Unione Europea

PON Ricerca e Innovazione 2014- 2020

Ministero dell'Istruzione, dell'Università e della Ricerca

Dottorato di Ricerca in Ingegneria dei Prodotti e dei Processi Industriali

Numerical simulations of a dosing jet:

impact of compressibility on an induced breakup

Carmelina Longo

PhD in *Industrial Product and Process Engineering* (XXX Cycle)

Department of Chemical, Material and Industrial Production Engineering

University of Naples Federico II

Scientific Committee:

Prof. Pier Luca Maffettone

Prof. Francesco Greco

Prof. Gaetano D'Avino

PhD Francesc Corominas

Contents

ABSTRACT

Filling operations, i.e., dosing a fixed amount of liquid in a bottle, are relevant in many industrial fields. A key aspect is a precise control of the breakup of the stream exiting a nozzle, avoiding events like dripping (falling down of drops) and stringing (formation of filament and threads). Breakup phenomena have been widely studied under constant flow rate conditions and different regimes of filament thinning have been identified. In this work, we analyze the effects of liquid properties and time-varying operating conditions on the breakup dynamics of a Newtonian liquid through Volume-of-Fluid numerical simulations and experiments. This thesis is divided in two main parts. In the first part, we study the dynamics of different classes of Newtonian liquids subjected to flow rates that linearly decrease in time. We find that the operating conditions only partially alter the thinning dynamics and, once a critical dimension of the filament has been reached, the dynamics is fairly described by scaling laws derived for steady-state operating conditions. In the second part, we address the filament breakup problem of a real dosing system. Experiments show the presence of air entrapped in the liquid phase during the process that significantly alters the breakup dynamics. The effect of entrapped air is accounted for in numerical simulations by defining and implementing a new model that adequately describes the compressibility effects induced by the coexistence of the two phases. The dissolved air delays the onset of the thinning phase and determines a slowdown of thinning dynamics. A good quantitative agreement between experiments and simulations in terms of time evolution of the filament radius at a fixed distance from the nozzle is found.

1. Introduction

The dynamics of a liquid exiting a nozzle and injected in an ambient gas is of high interest for many industrial applications, like ink-jet printing, sprays and atomization for combustion in engines, film coating, diffusion of fertilizers and pesticides, production of food or pharmaceutical powders, fiber and sheet drawing, and filling and dispensing operations. The aim of filling operations is to fill a number of cavities placed at a certain distance from the nozzle. It is a discontinuous operation and consists of repeated cycles of formation of a jet, followed by a sudden interruption aimed to break the jet. This technique is necessary when the cavities are particularly little and a small amount of liquid has to be injected, and using valves (that could physically obstruct the flow) is not possible. A fine control of the total flow rate and the instant of breakup is required during the filling phase, while phenomena like dripping (falling down of drops, Figure 1) and stringing (formation of filaments and threads, Figure 2) must be avoided in the no-flow phase (Danus, 2017).

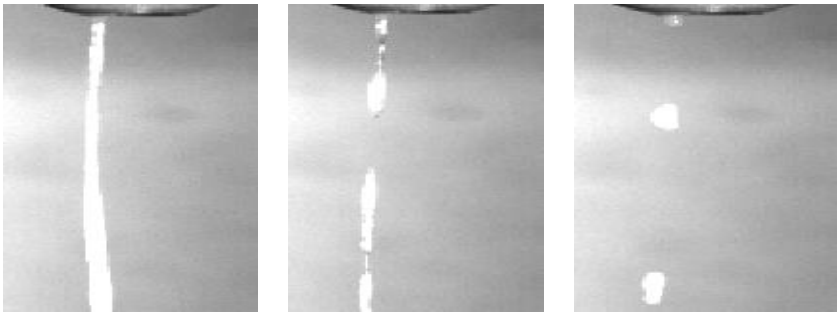

Figure 1: Sequence of dripping (Danus, 2017).

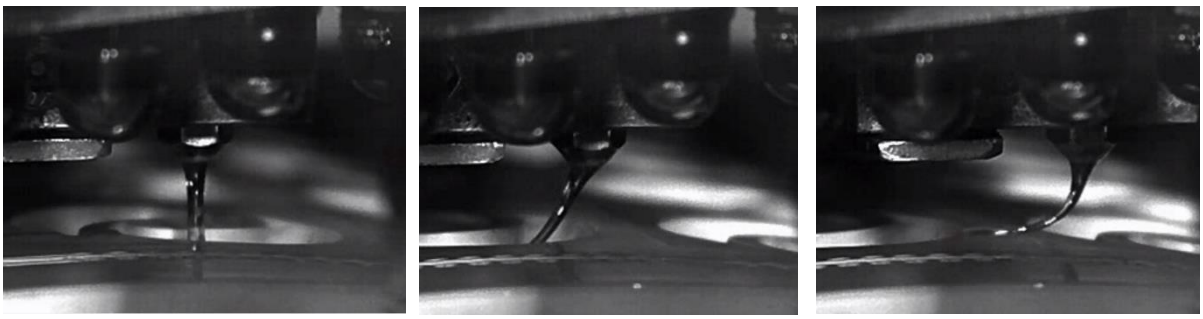

Figure 2: Sequence of stringing (Danus, 2017).

Filling operations are characterized by the passage of liquid through a nozzle, signing the transition from a *piping flow* to a *free-surface flow*. In the simplest case of no gas dispersed into the liquid, it means a transition from a single-phase to a multi-phase system, where the effect of surface tension has to be added to the other forces governing the motion of the fluid. The dynamics of a jet into the atmosphere is, in fact, governed by several forces: *inertial forces*, because the fluid has its own velocity, *gravitational force*, that causes its acceleration downwards, *viscous forces* that tend to prevent the breakup, and, in the case of non-Newtonian fluids, *elastic forces*, due to the intrinsic elasticity of the liquid.

The action of surface tension is to minimize the area between the liquid and the surrounding gas, and, to this end, it promotes the formation of drops, while inertia, viscoelasticity and gravity work in the opposite direction, like "preserving" the initial shape of the liquid jet. This action can be observed in apparently different phenomena: both for a dripping faucet and for a jet decaying into droplets. In the first case, surface tension and gravity effects play a major role: the first determines the shape of the drops, the second determines their falling down. In the case of a jet, droplets could be still observed at a certain distance from the nozzle: they are caused by small perturbations that, growing on the jet surface, reach a sufficiently large dimension to break the continuity of the flow. Perturbations of long wavelength reduce the surface area, so their growth is favored by surface tension (Eggers, 1997).

In both dripping faucet and jet breakup, we can observe a similar phenomenology: the formation of the drop is preceded by a deformation of the initial shape characterized by a thinning that leads to the setting-up of a filament (or *neck*, owing to its shape) linking a quasi-spherical volume of liquid to the remnant still attached to the nozzle. In Figure 3 and Figure 4 these two phenomena are shown. The local decreasing of jet diameter determines an increasing of velocity that pushes away the liquid: this is the reason why, in many cases, after the breakup and the detachment of the drop, a recoil of the neck is observed. In some cases, this primary separation is followed by a secondary one in the other

extremity of the neck: the resulting portion of liquid can rearrange its shape into a sphere to form one or more *satellite droplets* or conserve its extended aspect.

The dimension of primary or secondary drops, the presence of filaments, the time required for breakup, the stability of the jet as well as the direction in which drops are ejected and the shape of the jet are important aspects needed to properly design an industrial process equipment. It has been demonstrated that all these factors depend on the intrinsic properties of the liquid (surface tension, viscosity, elastic properties), on the flow and geometric conditions (flow rate, smoothness of the feeding tube, internal design of the nozzle), and on the action of the surrounding gas (aerodynamic forces).

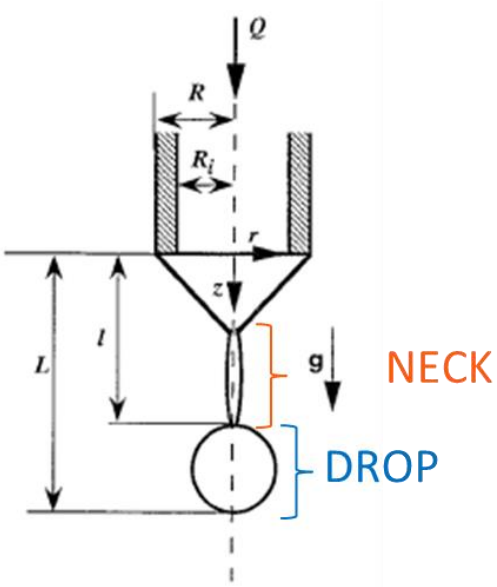

Figure 3: Sketch of a drop detaching from a nozzle. From the top to the bottom, it is represented the nozzle, the liquid attached, the neck and the forming drop.

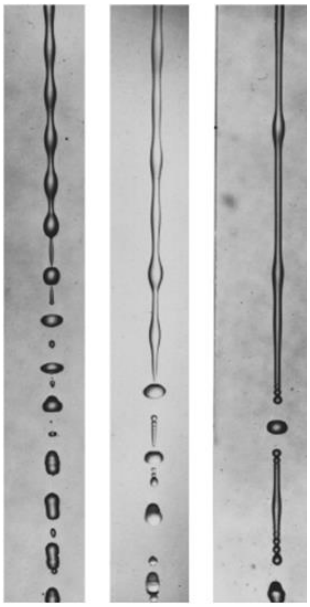

Figure 4: Photographs of a jet decaying into drops (Rutland & Jameson, 1971), excited by disturbances at three different frequencies (increasing wavelength from left to right).

In many industrial applications, a small amount of air is entrapped in the liquid phase, making the degree of complexity of the system even higher. Although it does not significantly alter the physical properties of the resulting mixture, it has large effects on the flow conditions. In filling operations, in fact, abrupt changes of velocity are typical, but the presence of the air dampens the transfer of information: a time delay from the point where the driving force acts and its effects at a given distance is observed and, when comparable to the typical temporal scales of the process, those effects are not negligible. As the flow-rate at nozzle is crucial to perform adequately the process, the understanding of the *piping flow* upstream of the nozzle is necessary, and so other parameters (pipe length and

diameter, pressure drops, amount of air, quality of flow) enter the picture. In addition, in order to efficiently breakup the jet exiting the nozzle, filling processes are generally operated under time-varying flow conditions, i.e., the flow rate is not constant in time but the flow is periodically stopped.

The aim of this work is to understand the dynamics of a fluid exiting a nozzle and injected in an ambient fluid in order to identify the characteristic parameters for the attainment of the desired flow condition, and to predict and control breakup. To this end, numerical simulations will be used, and will be compared with experimental results. In the next sections, we present an analysis of the available literature, the definition of the equations governing the problem, the description of the software chosen to carry out the simulations and preliminary results to validate the numerical code in the case of a stationary flow. Then, the effects of time-varying conditions have been analyzed with numerical simulations. In order to validate the code, numerical results have been compared with experiments, where a real dosing system has been used.

2. State of the Art

2.1 Historical excursus

The observation by a scientific point of view of the behavior of a jet and of the ways it breaks began with Leonardo da Vinci (1452-1519) who realized the existence of a cohesive force between particles of fluid: he noted that, when a drop detaches from a tap, the liquid at first stretches and, after breakup occurs, a small mass of liquid goes upwards "*with a movement contrary to the nature of heavy things*". In 1686 Mariotte, observing a stream of water decaying into drops, hypothesized that gravity or other external forces were responsible for the process. Savart (1833) understood for the first time that an intrinsic property of the fluid (later identified as *surface tension*) is responsible of breakup and observed tiny undulations growing along the liquid surfaces (shown in Figure 4). The link between them was discovered by Plateau (1849), who demonstrated how surface tension, whose aim is to minimize the surface area, determines an amplification of perturbations of long wavelength. Later, Lord Rayleigh (1878) understood that jet breakup is a consequence of a hydrodynamics instability. He recognized the role of inertia in breakup events and found the optimal wavelength assuring the fastest growing of the perturbations and setting the typical size of primary drops. The stability analysis provided by Rayleigh is able to predict the formation of the so called "primary drops", but the investigation of satellite droplets (fundamental in ink-jet printing field) needs to take in account non-linear terms, too. Based on Rayleigh's stability analysis, Tomotika (1935) took the surrounding fluid into account to quantify how the ratio between the viscosities of the jet liquid and of the ambient gas influences the growth rate of these disturbances. Chandrasekhar (1961) considered the contribution of liquid density as well as that of liquid viscosity on the jet dynamics.

After these pioneering works, a lot of publications appeared owing to the large number of applications in the field of breakup process. A fundamental theory has been proposed by Eggers (1997), who locally solved the Navier-Stokes equations for a Newtonian fluid (1993), assuming that around the point of breakup the motion becomes "universal" (concept of self-similarity), i.e., it does not depend on external parameters, but only on an internal length, which is a function of the fluid properties (viscosity, density and surface tension). Neglecting the outer fluid contribution, three regimes have been identified in the literature according to the dominating force acting against surface tension: *inertial* (Day, 2008, and Chen, 2002), *viscous* (Papageorgiou, 1995) and *inertial-viscous* (Eggers, 1993) (corresponding to infinite, zero and finite local Reynolds number, respectively), where scaling laws describe the dynamics of the local thinning. A fourth regime has been later on identified by Lister and Stone (1998) by considering the viscous resistance of the outer fluid, which occurs in the very last stages before breakup.

It is known that low and high viscosity fluids start to thin in an inertial and a viscous regime, respectively, and then exhibit a transition to inertial-viscous regime when approaching breakup conditions. Castrejón-Pita (2015) and Li and Sprittles (2016) have shown the existence of "intermediate" transient regimes that delay the onset of the inertial-viscous regime towards breakup.

2.2 Regimes of breakup

In this section, we provide a summary of the breakup regimes existing in the literature for Newtonian filaments and their similarity solutions, where lengths are made dimensionless with the nozzle radius R, time with $\eta R/\gamma$ where η is the viscosity of the fluid and γ its surface tension, and velocities with γ/η. Scaling laws available in the literature relate the minimum filament radius r_{min} and the local Reynolds number $Re_{loc} = \rho U_z L_z/\eta$ (with ρ the liquid density, U_z and L_z appropriate axial velocity and length scales near pinch point, respectively) to the time from breakup $\tau = t_b - t$, where t_b is the breakup time.

For a low viscosity liquid, pinching occurs in an inertial (I) regime, characterized by a balance between inertial and capillary forces. Scaling laws give (Day, 1998; Chen, 2002):

$$r_{min} \sim \tau^{2/3} \tag{2.1}$$

$$Re_{loc} \sim \left(\frac{\tau}{Oh^2}\right)^{1/3} \tag{2.2}$$

where Oh is the Ohnesorge number defined as $Oh = \eta/\sqrt{\rho R\gamma}$. Such a regime is found when $Oh \ll 1$. Notice that, as breakup is approached ($\tau \to 0$), $Re_{loc} \to 0$. The breakup has been found to be asymmetric, with a cone attached to a spherical cell with angles of 18.1° and 112.8° with the z-axis, as represented in Figure 5 (Day, 1998).

On the other hand, when viscous forces dominate ($Oh \gg 1$) (Papageorgiou, 1995):

$$r_{min} = 0.0709\tau \tag{2.3}$$

$$Re_{loc} \sim \tau^{-0.65}/Oh^2 \tag{2.4}$$

In the viscous regime (V), $Re_{loc} \to \infty$ when $\tau \to 0$ and the shape of the filament around the pinching point is symmetric: the radius locally decreases in the middle of a thin, quasi-cylindrical filament.

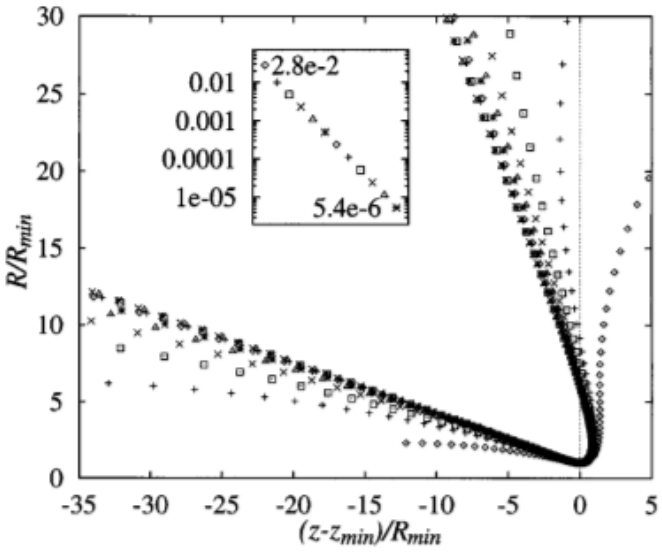

Figure 5: The pinchoff shapes collapsing onto two cones when rescaled with minimum radius $r_{min}(t)$ and centered on $z_{min}(t)$. Inset shows key of r_{min} over three decades (Day, 1998).

Regardless the initial stages of pinching, at the instant of breakup, inertial and viscous forces are in balance ($Re_{loc} \sim 1$) and together resist to capillary forces. The local solution of the Navier-Stokes equations gives (Eggers, 1993):

$$r_{min} = 0.0304\tau \tag{2.5}$$

$$Re_{loc} \sim 1 \tag{2.6}$$

with an asymmetric configuration of a drop joined to a thin thread.

Transitions from inertial (I) to inertial-viscous (IV) regime are predicted to occur when (Chen, 2002; Notz, 2001):

$$r_{min,crit} \sim Oh^2 \quad (2.7).$$

Transitions from viscous (V) to inertial-viscous (IV) regime are predicted to occur when (Basaran, 2002; Eggers, 2005):

$$r_{min,crit} \sim Oh^{-3.1} \quad (2.8).$$

2.3 Dripping and jetting regimes

Free-surface flows, as Rayleigh already demonstrated, are characterized by *instabilities*. When the feeding flow is stationary and the flow-rate is low, the system is *absolutely* unstable: the liquid is ejected drop-by-drop because the surface tension initially "holds" the liquid near the nozzle, collecting it into a hemispherical "bag" that slowly increases in dimension (and mass). As soon as a critical volume is reached, gravity overcomes pulling down the liquid: surface tension determines the formation of a neck, followed by the breakup with the ejection of a quasi-spherical volume of liquid. This condition is called *dripping regime*. When velocity increases, the instability is convected away from the nozzle: if velocity is high enough, the system enters in a *jetting regime*, in which a stable (quasi) cylindrical-shaped jet is obtained. The higher this velocity is, the further the jet disintegrates. The regimes are shown in Figure 6 in the case of water: (a) represents dripping regime and (c) represents jetting regime. Between them, a transition regime exists known as "*chaotic dripping*" (b).

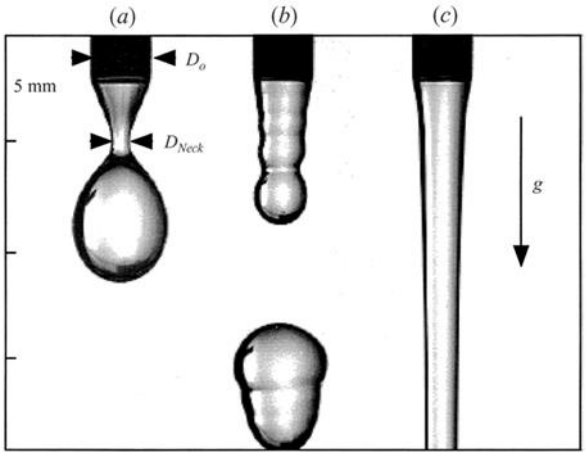

Figure 6: The transition from dripping (*a)* to jetting regime (*c*) for water. *(b)* represents a transition regime called "*chaotic dripping*".

Clasen *et al.* (2011) described the behavior of different classes of fluids according to the operating conditions they are processed in, giving a quite complete report. It is important to point out that gravitational forces are not taken in account.

As previously outlined, breakup is preceded by a decreasing of the radius linking the forming drop to the portion of fluid still attached to the nozzle. This *necking* (or *thinning*) phase is characterized by a radial velocity, that describes how r_{min} changes on time, called *thinning velocity*, that in a dimensional form is:

$$U_t = -\frac{dR_{min}}{dt} \quad .$$

According to the previous section, in a dimensional form:

$U_{t,\eta} = 0.0709\frac{\gamma}{\eta}$ Viscosity Controlled Thinning (high-viscosity, Newtonian fluid)

$U_{t,\rho} = 0.3413\sqrt{\frac{\gamma}{\rho R}}$ Inertia Controlled Thinning (low-viscosity, Newtonian fluid)

where the numerical prefactor comes from literature (i.e., Day, 1998; Rodd, 2005).

The critical *Oh* value discriminating between the two regime is $Oh_c = 0.2077$ (Clasen, 2011).

To determine if the flow is in a dripping or a jetting regime is possible to compare the thinning velocity U_t with the jet velocity U (axially directed): when the liquid moves downwards faster than the decreasing rate of its radius, a continuous jet is formed. On the contrary, when it moves slower, dripping regime is dominating the motion.

Other two dimensionless numbers can be used to determine the flowing regime. They are indicated in Table 1, where in fourth column, a critical value has been determined for the identification of the flow regime: values of the dimensionless numbers lower or higher than these reference values state a dripping or a jetting regime.

Capillary Number	$Ca = \frac{\eta_0 U}{\gamma}$	$U_{t,\eta}$ vs U	$Ca_c = 6.5$
Weber Number	$We = \frac{\rho U^2 R}{\gamma}$	$U_{t,\rho}$ vs U	$We_c = 0.1 \div 1$

Table 1: Dimensionless numbers of flow regime.

It is important to notice that the dimensionless numbers so far defined are not all independent. In fact, $Oh = \frac{Ca}{\sqrt{We}}$ and $Re = \frac{We}{Ca} = \frac{\rho U_j R}{\eta}$. Two of them can define an operating space (represented in Figure 7), where, by the knowledge of fluid properties and the operating conditions, it is possible to locate a point and to predict which kind of flowing regime will be reached and what are its characteristics.

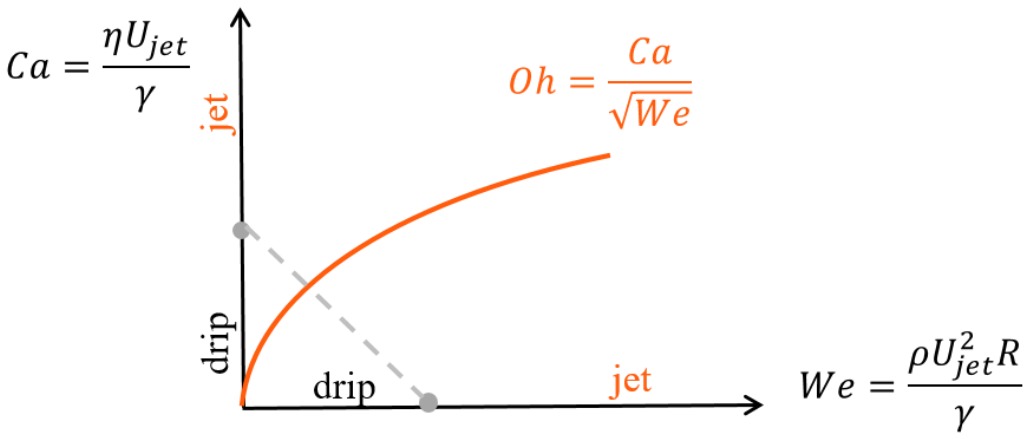

Figure 7: Operating space for dispensing. U_{jet} is the jet velocity U.

2.4 Stability of a Jet

A jet issuing in an ambient gas can experience different dynamics depending on the liquid properties and the operating conditions. Its behavior has been reviewed by Lin (1998) and Dumouchel (2008). Four main regimes have been observed, as shown in Figure 8:

a. Rayleigh regime (characterized by Rayleigh instability);
b. first-wind induced regime;
c. second-wind induced regime;
d. atomization regime.

They correspond to different combinations of liquid inertia, surface tension and aerodynamic forces acting on the jet and their macroscopic differences consist in the typical dimension of drops and in the *unbroken length* L_B, defined as the distance from the nozzle where the first droplet forms. The correlation between regimes and drop dimensions is represented in Figure 9 from a qualitative point of view: moving from the Rayleigh to the atomization regime, the drop diameter, initially having a size comparable to the jet, decreases of several orders of magnitude.

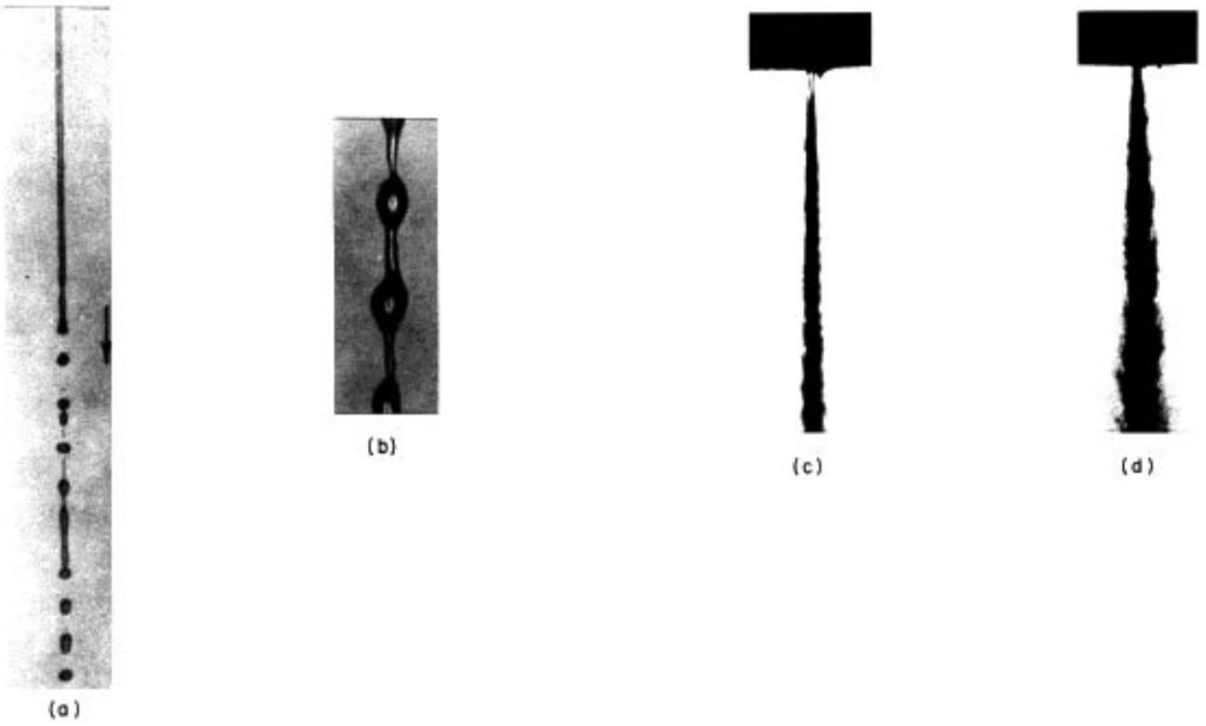

Figure 8: Four jet breakup regimes (Chiegier & Reitz, 1996).

In Figure 10, how the unbroken length varies with the velocity of the jet is qualitatively represented: in the Rayleigh regime (A), an increasing velocity leads to an increasing L_B up to a maximum that denotes the beginning of the first wind-induced regime (B). In this regime, at variance with the previous one, higher velocities imply a decreasing of the unbroken length. These two regimes are well understood and are well predicted (in terms of drop dimensions and fluid properties) by linear stability theories. The instability causing the breakup for A and B cases is attributed to long-wavelength, small amplitude disturbances growing on liquid surface. When a critical value of velocity is reached, the two last regimes (C) and (D) appear, where the jet dynamics mainly depends on aerodynamic forces. The second wind-induced regime (C) and the atomization regime (D) coexist for same values of velocity. However, in the first case, L_B increases with U, while, in the other case, L_B decreases for an increasing U. In this case, the instabilities are of short-wavelength nature.

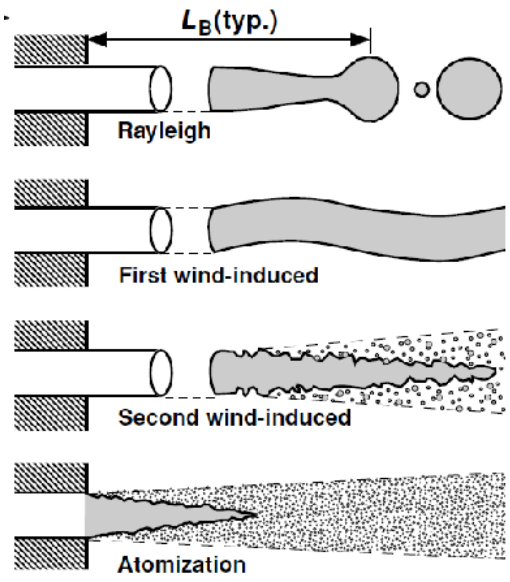

Figure 9: Sketch of breakup regimes.

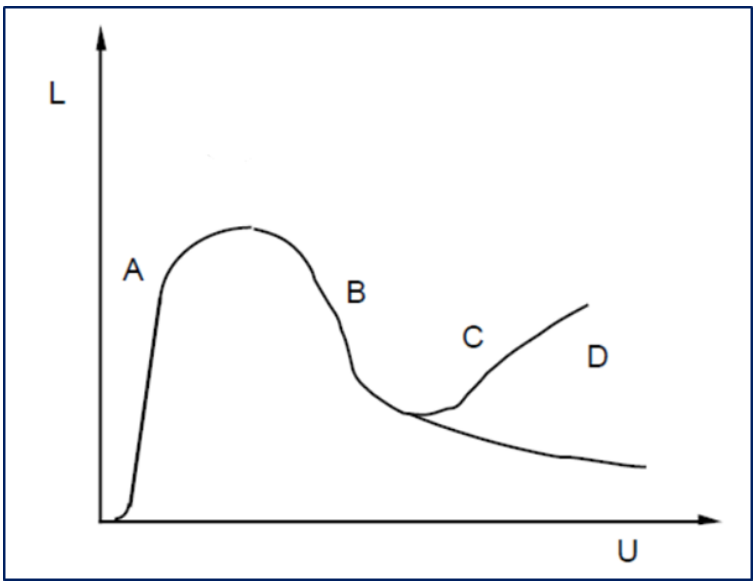

Figure 10: Schematic diagram of the jet breakup length curve.

Depending on the specific industrial purpose, one of the aforementioned regimes can be preferred: atomization is fundamental in the case of combustion in engines as well as of drying equipment, where the diffusion of small droplets is desired. In the case of filling, dispensing and dosing processes, it is important to obtain a stable, continuous jet in order to avoid fouling events (Rayleigh and first wind-induced regime).

Criteria for attainment of Rayleigh regime are:

$We > 4$ and $We_g < 0.2$ (Ranz, 1959)

or $We_g < 1.2 + 3.41\left(\frac{Oh}{\sqrt{2}}\right)^{0.9}$ with $We_g = \rho_g RU/\gamma$ (Sterling A.M., 1975)

Criteria for attainment of first wind-induced regime are:

$We > 4$ and $1.2 + 3.41\left(\frac{Oh}{\sqrt{2}}\right)^{0.9} < We_g < 6.5.$ (Ranz, 1959)

As seen, a jet always breaks, but it is possible to assure a continuity for a certain distance from the nozzle. In other words, if unbroken length is high enough, the jet is stable for planning purposes. A quantitative estimation of the unbroken length is then necessary, to be compared to the extension that the jet should have for a particular operation. Assuming that the aimed regime is the Rayleigh's one, we have to face with long-wavelength disturbances. Since no detailed information is available on these disturbances, this makes impossible to universally predict breakup length. In this regard, several

correlations between the unbroken length and the relevant dimensionless parameters have been proposed:

1) $\frac{L_B}{d} = 12\left\{(We)^{0.5} + \frac{3We}{Re}\right\}$; (Weber, 1931)

2) $\frac{L_B}{d} = \ln\frac{a}{\delta_0}\left\{(We)^{0.5} + \frac{3We}{Re}\right\}$

$\ln\frac{a}{\delta_0} = -2.66\ln(Oh) + 7.68$

3) $\frac{L_B}{d} = 19.5\left\{(We)^{0.5} + \frac{3We}{Re}\right\}^{0.85}$ (Grant & Middleman, 1966)

4) $\frac{L_B}{d} = 6.5\,We^{0.5}(1 + 3Oh)/Oh^{0.15}$ for $Oh < 0.017$

5) $\frac{L_B}{d} = 12\,We^{0.5}(1 + 3Oh)$ for $Oh > 0.017$ (Takahashi & Kitamura, 1972)

In these equations, d is the jet diameter, We and Oh are the dimensionless numbers already defined, Re is the Reynolds number ($Re = \rho DU/\mu$). Assuming a water jet with a velocity $U = 0.5\ m/s$ ($\rho = 1000\ kg/m^3$, $\sigma = 0.07 Kg/s^2$, $\mu = 10^{-3}\ Kg/m\,s$) the estimated unbroken lengths obtained with the previous correlations show large differences as indicated below:

1) $L_B = 38.2\ d$
2) $L_B = 73.1\ d$
3) $L_B = 52.2\ d$
4) $L_B = 49.1\ d$.

The problem of determination of the unbroken length and, indirectly, that of understanding the origin of disturbances growing on the jet surface has been faced by Umemura (2011) and Umemura *et al.* (2011). They proposed, as a solution for the periodic disintegrating liquid jet, a self-destabilizing loop, consisting in:

- a capillary wave created because of liquid jet contraction, propagating upstream until the nozzle is reached;
- a convective unstable wave reproduced at the nozzle exit and moving downstream, increasing its amplitude and causing the periodic breakup;
- a same amplitude for the capillary wave and the beginning of convective unstable wave.

The reflection of capillary wave depends on the dynamics at the nozzle exit. For example, for a long nozzle and a low Reynolds number, a fully developed laminar flow is obtained: when it exits a nozzle, the profile "relaxes" owing to the absence of solid walls. The relaxation is conceptually shown in Figure 11, where the radius of the jet r and the distance form the exit x are made dimensionless with the radius of the nozzle a.

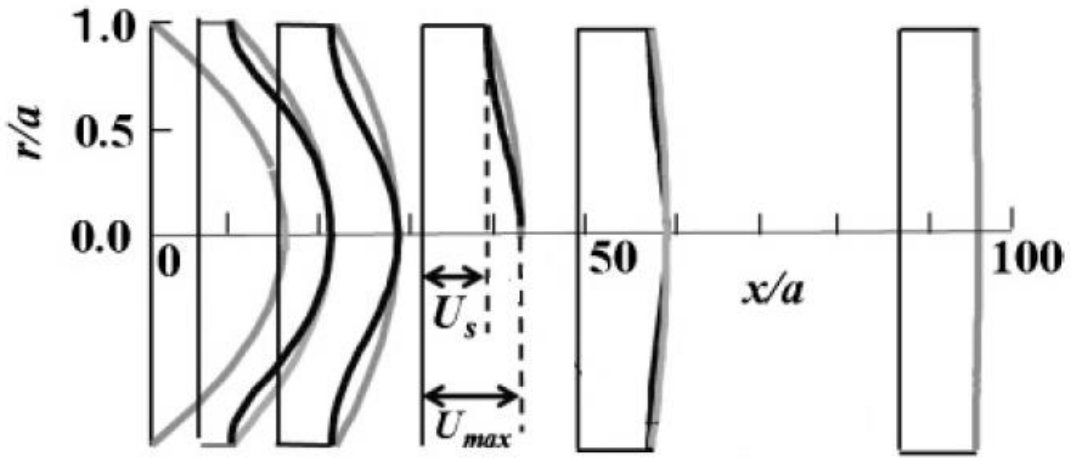

Figure 11: Modeling of velocity profile relaxation. Grey lines are extraction of Plateau-Rayleigh-type instability characteristics. Black lines represent the baseline jet flow. Numerical values calculated for: $\sqrt{We} = 2$ and $Oh = 0.006$.

Furthermore, the presence of two average breakup lengths, a long one and a short one, occurring for a same value of jet speed, was noted in the experiments performed in these works. They depend on different combinations of gravitational jet acceleration, velocity profile relaxation and vortex shedding from the nozzle entrance. The results are represented in Figure 12, where average long breakup distance (LBD) and average short breakup distance (SDB) are plotted versus $\sqrt{We}$ (for a given fluid and geometry, it depends only on jet velocity), for different values of the nozzle radius. Experiments have been repeated in different days, using water. At low steady jet speeds ($\sqrt{We} < 1$), a hysteresis phenomenon occurs (as indicated by the small arrows), that represents the transition between the dripping and jetting regime and vice versa. For higher $\sqrt{We}$, two groups of plots are noticeable: which breakup length occurs is random in experiments, but once LDB or SDB is occurred in a run, no transition to the other group is observed.

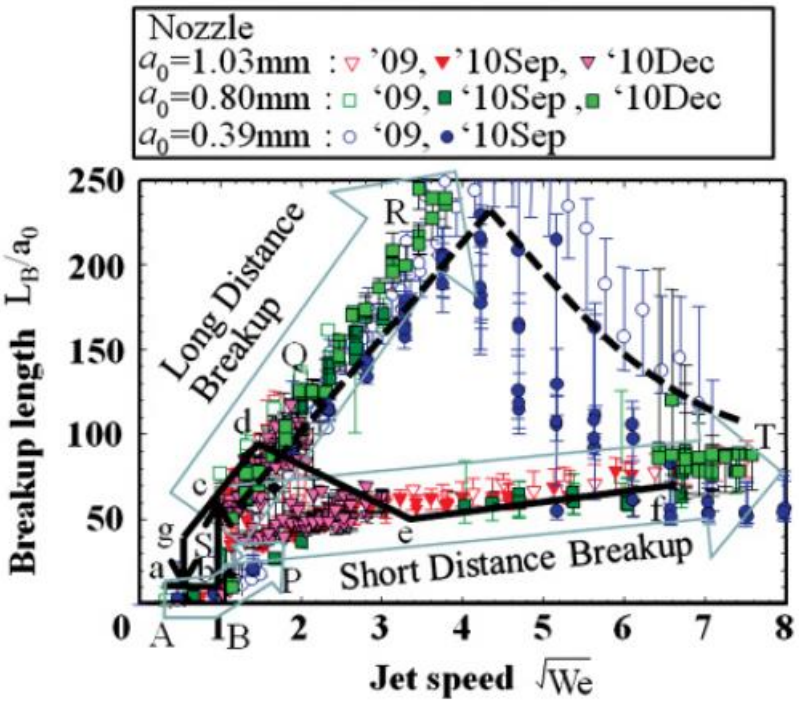

Figure 12: Dependence of average breakup length on jet issue speed. Symbols indicate experimental results for different values of nozzle radius (a_0), with different tranches of experiments.

2.5 Effect of gravity

Gravity force has been believed to be the real responsible of formation of drops in early works, since drops were observed for vertical downwards jets and not for upwards ones. Afterwards, the role of surface tension has been understood and instabilities have been demonstrated to propagate both upwards and downwards (Keller, Rubinow, & Tu, 1973).

To account for the gravity force, the two dimensionless numbers reported in Table 2 can be defined.

Froude number	$Fr = \frac{U^2}{g\,R} = \frac{Inertia}{Gravity}$
Bond number	$Bo = \frac{\rho R^2 g}{\gamma} = \frac{Gravity}{Surface\ tension}$

Table 2: Dimensionless numbers. (Part 3)

As the Bond number depends on the square of the radius, in the case of very small scales, gravity effect can be neglected in considering the dynamics near the nozzle. As we move far from the nozzle,

gravitational forces cause the acceleration of the flow, determining the increase of inertial forces over the viscous ones. Even for a highly viscous fluid, at a certain distance from the nozzle, the force controlling thinning velocity is the inertial one.

On the other hand, the effect of gravity on capillary instability has been studied by Amini *et al.* (2013). Their results show that for an increasing Bond number, critical Weber number decreases. As already discussed, critical Weber number defines the transition between dripping regime and jetting regime in an inertia controlled thinning. Now, since Weber number depends linearly on the radius, for a same fluid the velocity necessary to obtain a jetting regime is lower when radius increases.

2.6 Effect of viscosity

Jet destabilization is a phenomenon easy to observe in the case of low-viscosity Newtonian fluids. However, if we consider, for example, the dynamics of a filament of honey falling down from a spoon, we can note the development of a long thread, in spite of a high source of instability due to our inability to hold our hand motionless.

Breakup, in the case of viscous fluids, is indeed delayed owing to two effects:

1. The action of viscous forces against capillary forces during thinning phase;
2. Dampening of unstable waves on thread surface.

The effects of the delay and of the formation of a very long thread are clearly shown in Figure 13, where the profiles of three different fluids are represented near the point of breakup.

The passage for a viscous fluid from a symmetrical solution away from breakup (viscous thread) to a strong asymmetrical solution (like the low-viscosity fluids' one) has been demonstrated by Kowalewsky (1996) and coincides with the formation of a secondary thread (asymmetric) from the original neck (symmetric), that gets longer as viscosity increases.

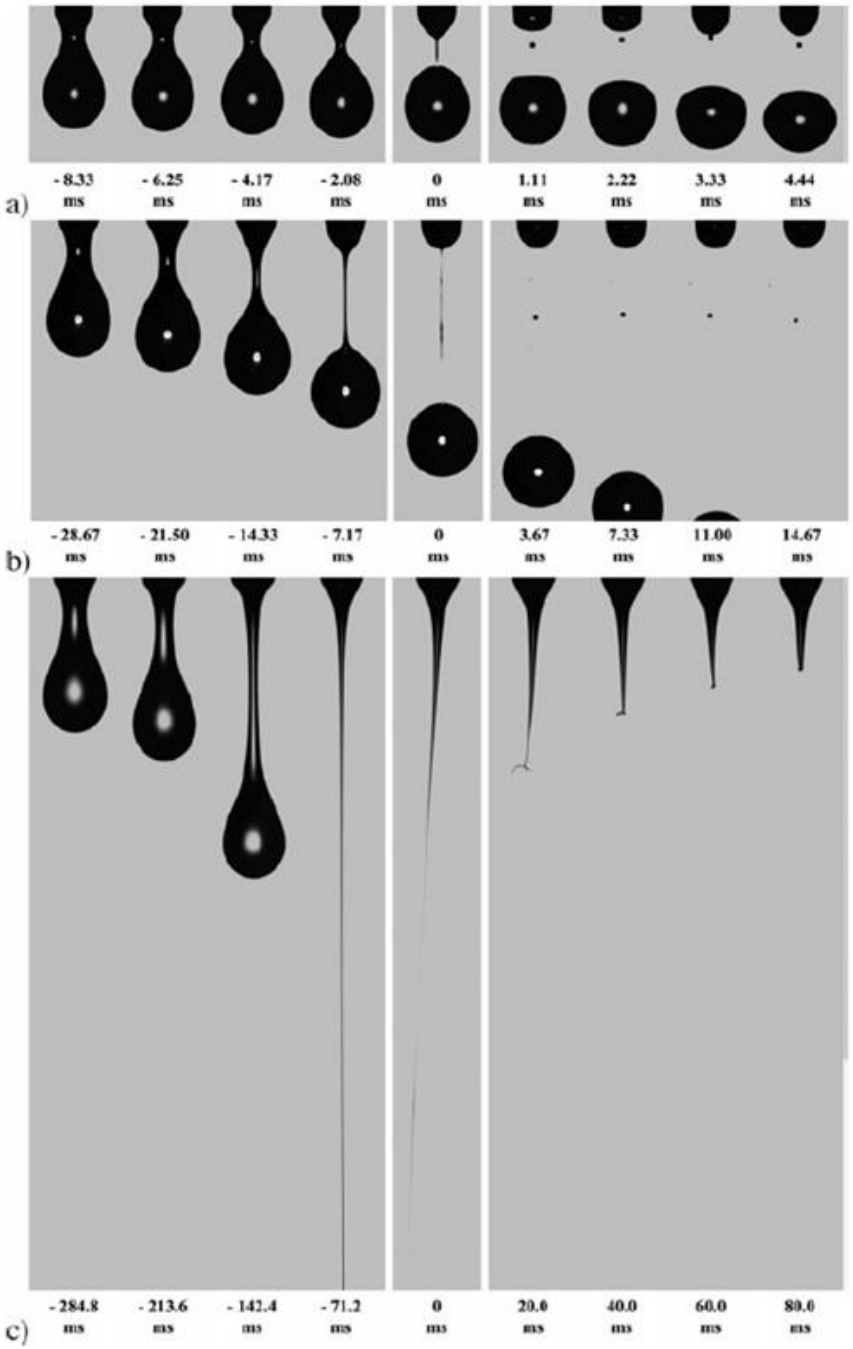

Figure 13: Breakup of Newtonian fluids for Newtonian fluids (Clasen, 2001): (a) inertia-controlled thinning: $Oh = 0.05$, $We = 0.0005$; (b) viscosity-controlled thinning: $Oh = 1.18$, $Ca = 0.02$ (c) viscosity-controlled thinning: $Oh = 63.3$, $Ca = 0.14$

Figure 14: Pictures of thread before breakup, $Re = 0.32$. (a) 2.8 ms before breakup and (b) is 1.5 ms before breakup. Solid lines are Stokes similarity solutions. (Kowalewski, 1996).

2.7 Unsteady flow-rate

In the most works available in the literature, breakup events have been studied in the case of a constant feeding flow, both in the case of low and high velocities. However, real industrial equipment may need a time-dependent flow rate. Filling operations and ink-jet printing are two examples of discontinuous operations.

The effect of an unsteady flow-rate on the breakup of a Newtonian fluid has been analyzed in the work of Xu and Basaran (2007): they, for the first time, consider a feeding flow that varies in time and has a phase of pushing, followed by a phase of suction. Figure 15 and Figure 16 show the geometry of the nozzle and the velocity profile of the feeding flow, respectively.

The aim of the work was to evaluate if a drop is ejected from the nozzle by means of a velocity inversion. The effect of different parameters has been taken into account in terms of dimensionless numbers: Oh, that represents flow characteristics (in particular, the influence of viscosity), and We, that represents the operating conditions (the amplitude of velocity curve). A dimensional parameter, Ω, represents the frequency of the velocity profile, that is assumed a sinusoidal function of time. Gravitational effect has been assumed to be negligible.

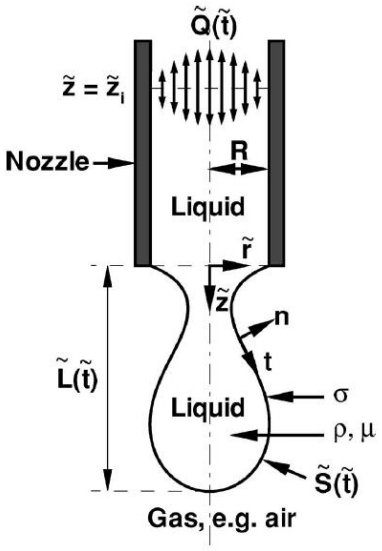

Figure 15: Sketch of the geometry. z_i is where velocity profile is imposed, the nozzle exit is the origin of z axis.

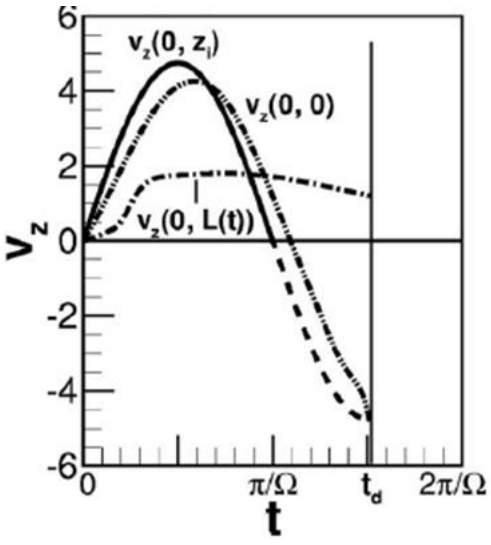

Figure 16: Profile of axial velocity for different positions, along the axis.

The results are shown to be dependent mainly on We number and Ω. Figure 17 represents a phase diagram in the (We, Ω)-space formed of three distinct regions. In region A no drop is formed, in regions B and C a drop is formed with a different velocity field: in region B the velocity at the tip of the drop is upwards, while in region C is downwards. Figure 18 and Figure 19 represent liquid behavior, respectively, in region A and region C.

The frequency Ω of feeding flow also affects the drop formation: two different shapes are represented in Figure 20 for fixed We and Oh numbers at two different values of Ω.

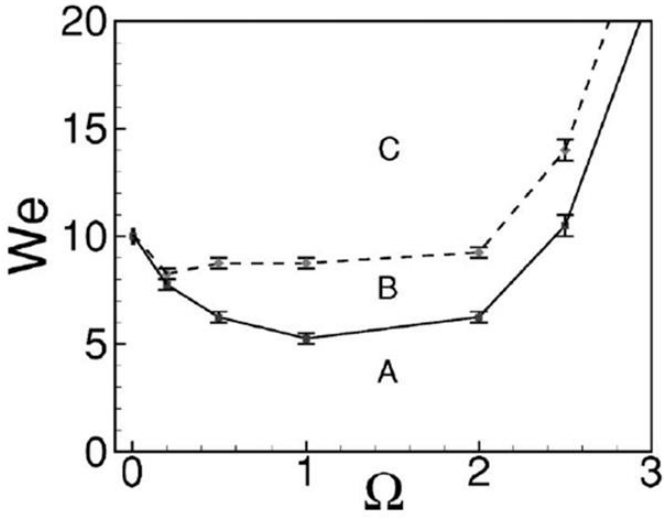

Figure 17: Phase diagram of behavior of Newtonian fluid with $Oh = 0.1$. A: no drop formation; B: a drop with an upwards velocity at the tip is formed; C: a drop with a downwards velocity at the tip is formed.

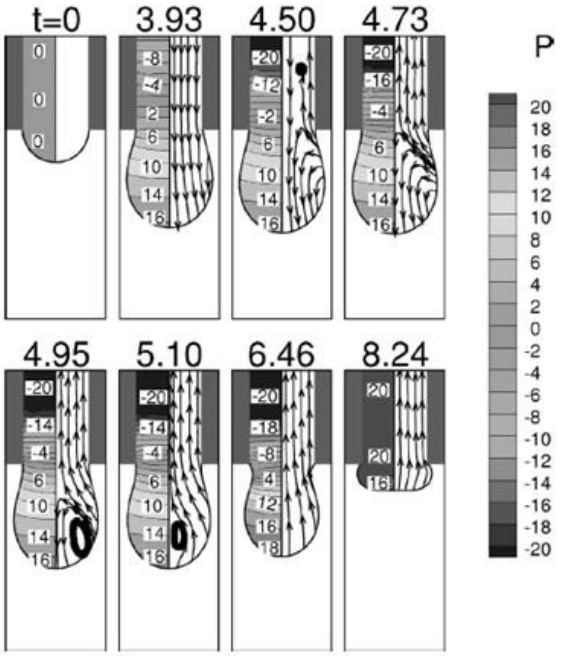

Figure 18: Shape and pressure field of liquid in region A.

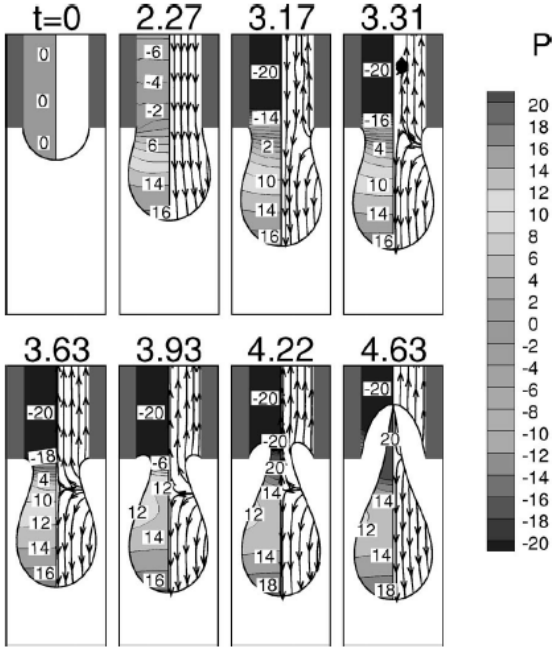

Figure 19: Shape and pressure field of liquid in region C.

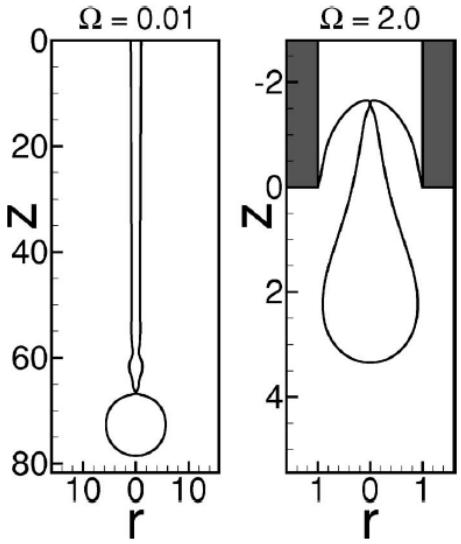

Figure 20: Two different shapes for an ejecting drop. $Oh = 0.1, We = 10$.

2.8 The role of the air

The behavior of a liquid exiting a nozzle is the most important, final stage of the more complex process of filling operation. Since the ability to provide a sudden interruption of the flow is crucial, a fine control of the flow rate and an immediate response of the liquid flow to abrupt changes in velocity

are necessary. The pump is usually placed at a certain distance from the nozzle: the imposed flow rate needs a finite time to develop throughout the pipeline, and the signal transmission has to be as fast as possible. In this regard, a significant role is played by the liquid composition: if some air enters the liquid phase, it can strongly alter the response of the material to pressure and velocity variations that move at the speed of sound.

A number of configurations, or *flow patterns*, can be observed in a gas-liquid flow, and they are usually recognized by a visual inspection (Brennen, 2005). Figure 21 and Figure 22 represent, respectively, the sketches of flow regimes that an air/water system can experience in a horizontal pipe, and a phase diagram showing the occurrence of those regimes according to the fluxes of the phases.Figure 23 and Figure 24 show the same schemes, but related to vertical flows.

Despite the classifications, two main "categories" of flow patterns can be identified: *disperse*, where one component is dispersed as drops or bubbles in the other continuous phase, and *separated*, composed by two (or more) separate streams. A disperse flow pattern where the disperse phase is composed by very small (much smaller than the pipe dimensions) distributed particles is a *homogeneous* multiphase flow: in that case, the relative motion between the phases can be neglected, with a notable simplification in the description of motion.

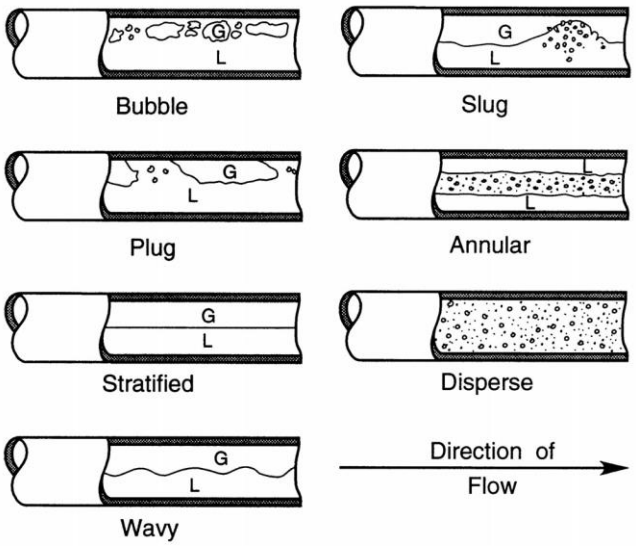

Figure 21: Sketches of flow regimes for flow of air/water mixtures in a horizontal, 5.1cm diameter pipe. Adapted from Weisman (1983).

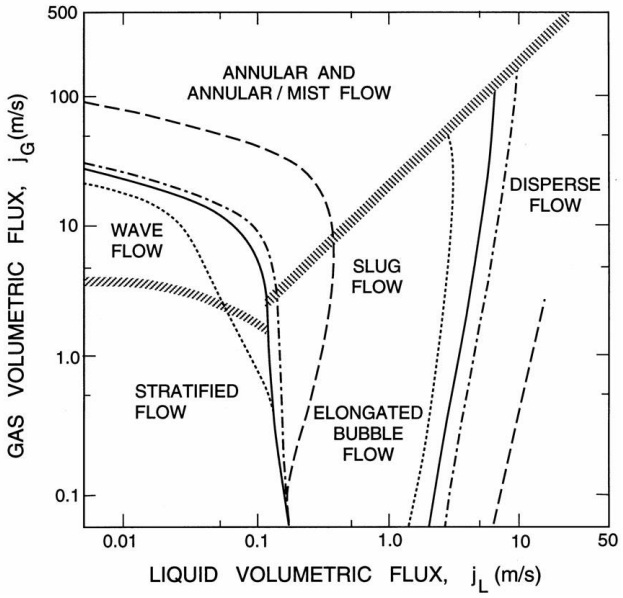

Figure 22: Flow regime boundaries for various pipe diameters: 1.25cm (dotted lines), 2.5cm (solid lines), 5cm (dash-dot lines) and 30cm (dashed lines). From Mandhane et al. (1974).

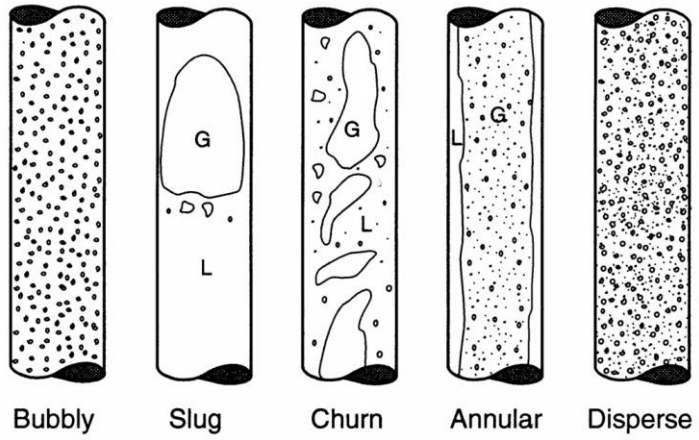

Figure 23: Sketches of flow regimes for two-phase flow in a vertical pipe. Adapted from Weisman (1983).

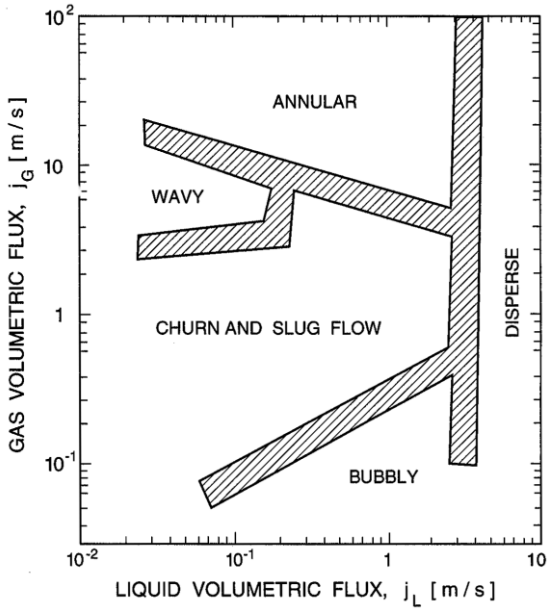

Figure 24: A flow regime map for the flow of an air/water mixture in a vertical, 2.5cm diameter pipe showing the experimentally observed transition regions hatched. Adapted from Weisman (1983).

A pressure wave travels in a given medium at sound velocity: a change in the flow rate occurring near the pump can be observed at the end of the pipeline after a time calculated by dividing the pipe length by the speed of sound. It has been demonstrated (Brennen, 2005), for a homogeneous multiphase flow in absence of any exchange of mass between the components and neglecting surface tension, the acoustic impedance of the mixture, $\frac{1}{\rho c^2}$, is simply given by the average of the acoustic impedance of the components weighted according to their volume fractions:

$$\frac{1}{c^2} = (\rho_A \alpha_A + \rho_B \alpha_B)\left(\frac{\alpha_A}{\rho_A c_A^2} + \frac{\alpha_B}{\rho_B c_B^2}\right) \qquad (2.9).$$

Figure 25 shows the sonic velocity for a water/air system at atmospheric pressure. It is clear that, in the absence of air, the lines should intercept the vertical axis at a value of 1484 m/s (i.e., the sound speed in pure water), while, at the other extreme (only air in the system) the intercept should be 343 m/s (i.e., the sound speed of pure air). When air and water coexist, the sonic velocity is much lower than the sonic velocities of the pure components, even when a very small amount of air is entrapped in the liquid, with a consequent increasing of the time needed for the information to travel along the pipe.

In conclusion, the amount of air dissolved in the liquid has a crucial role in filling operations and must be taken into account to properly model and design the system.

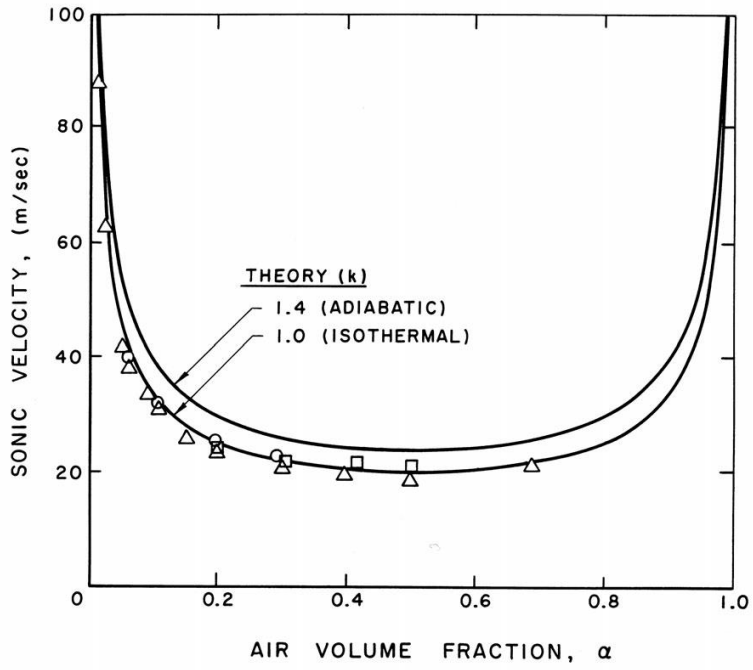

Figure 25: The sonic velocity in a bubbly air/water mixture at atmospheric pressure for both adiabatic and isothermal transformation. Experimental data presented is from Karplus (1958) and Gouse and Brown (1964) for frequencies of 1 *kHz* (⊙), 0. 5 *kHz* (□), and extrapolated to zero frequency(△). Adapted from Brennen (2005).

3. Aim of the work

The aim of this work is to study the free-surface flow of a fluid exiting a nozzle and injected in atmosphere by means of numerical simulations, validated with experimental results. In particular, we focus our attention on the dynamics exhibited by different classes of fluids undergoing time-varying inlet conditions, where a breakup of the liquid stream is induced by alternating pushing and sucking back phases.

As starting point, the behavior of an incompressible Newtonian liquid exiting a nozzle at a constant flow rate, high enough to have a continuous jet, is investigated. Indeed, it represents the simplest case of free-surface flows dynamics, and, as such, both analytical and numerical solutions are available in the literature that will be used to validate our simulation results. In the next sections, we show the governing equations, the software adopted in the numerical simulations, the geometry and the mesh used. We also report the results for some test cases under steady-state flow conditions.

The steady solution so obtained is then used as initial condition of the problem with time-varying inlet conditions. In particular, we impose a velocity profile that linearly decreases in time: the direction of the motion is inverted as the mean velocity crosses the zero value. We study the effects of the sucking back velocity on the breakup and we compare the results with the scaling laws derived from steady-state conditions.

In the last part of this thesis, we extend the study to a real dosing system, in order to test and validate the code. We found that the liquid undergoing dosing cycles is affected by the presence of a disperse gaseous phase in a continue liquid phase. Due to the relevance of the dispersed air on the flow

dynamics mentioned in the previous section, the incompressible fluid hypothesis is removed. To this aim, an equation of state able to adequately describe the liquid phase needs to be defined and implemented in the numerical code. Moreover, since the flow rate experienced by the liquid stream at the nozzle is strongly affected by the compressibility, and, as such, it is unknown, the whole dosing system (from the pump to the nozzle) needs to be simulated. The experimental apparatus, the numerical and experimental results on the real system are presented and discussed.

4. Mathematical model and numerical method

4.1 Governing equations

Let us consider a Newtonian fluid flowing in a pipe and exiting a nozzle in the ambient air. Assuming isothermal conditions, the governing equations are the Navier-Stokes equations for both phases (liquid and air):

$$\frac{\partial \rho_1}{\partial t} + \boldsymbol{\nabla} \cdot \rho_1 \boldsymbol{v_1} = 0 \tag{4.1}$$

$$\frac{\partial \rho_1 \boldsymbol{v_1}}{\partial t} + \boldsymbol{\nabla} \cdot (\rho_1 \boldsymbol{v_1} \boldsymbol{v_1}) = -\boldsymbol{\nabla} p_1 + \eta_1 \boldsymbol{\nabla}^2 \boldsymbol{v_1} + \rho_1 \boldsymbol{g} \tag{4.2}$$

$$\frac{\partial \rho_2}{\partial t} + \boldsymbol{\nabla} \cdot \rho_2 \boldsymbol{v_2} = 0 \tag{4.3}$$

$$\frac{\partial \rho_2 \boldsymbol{v_2}}{\partial t} + \boldsymbol{\nabla} \cdot (\rho_2 \boldsymbol{v_2} \boldsymbol{v_2}) = -\boldsymbol{\nabla} p_2 + \eta_2 \boldsymbol{\nabla}^2 \boldsymbol{v_2} + \rho_2 \boldsymbol{g} \tag{4.4}$$

where $\boldsymbol{v}$ is the velocity field, p the pressure, t the time, $\boldsymbol{g}$ the gravitational field. The density of the fluids is indicated by ρ and viscosity by η, where subscripts 1 and 2 refer to liquid and gas phase, respectively.

On the free surface (i.e., the contact boundary between the two phases), pressure and viscous forces are balanced by capillary forces:

$$\boldsymbol{n} \cdot [\boldsymbol{\sigma_1} - \boldsymbol{\sigma_2}] = \gamma \boldsymbol{n}(\boldsymbol{\nabla} \cdot \boldsymbol{n}) \tag{4.5}$$

where $\boldsymbol{\sigma}$ is the stress tensor, $\boldsymbol{n}$ the normal vector pointing out of the fluid domain, and γ the surface tension. Of course, these equations need to be completed by boundary conditions on the external boundaries that will be discussed below.

The terms of the equations can be adimensionalized with an appropriate choice of characteristic parameters. Of course, different possibilities exist: typically, the approach used to model the pinchoff is to refer to local quantities (i.e., velocities $U_{t,\eta}$ and $U_{t,\rho}$ defined in section 2.3). Our choice is to refer to global quantities because our problem ranges between i) different conditions of flow (from stable jet to pinchoff) and ii) different flow regimes (from inertial to viscous).

Then, dimensionless quantities are: $\boldsymbol{v}^* = \boldsymbol{v}/U_c$, $t^* = t\,L_c/U_c$, $\boldsymbol{\sigma}^* = \boldsymbol{\sigma}\,\gamma/L_c$ and $\rho^* = \rho/\rho_c$, where U_c, L_c, and ρ_c are characteristic velocity, length, and density. In what follows, we selected U_c as the mean flow velocity $\bar{U}$, L_c as the nozzle radius R, and ρ_c the density at atmospheric pressure ρ_0.

The dimensionless form of Eqs. (4.1)-(4.4) is reported below (without subscripts denoting the two phases):

$$\frac{\partial \rho^*}{\partial t^*} \boldsymbol{\nabla}^* \cdot \rho \boldsymbol{v}^* = 0 \tag{4.6}$$

$$\frac{\partial \rho^* \boldsymbol{v}^*}{\partial t^*} + \boldsymbol{\nabla}^* \cdot (\rho^* \boldsymbol{v}^* \boldsymbol{v}^*) = -\frac{1}{We} \boldsymbol{\nabla}^* p^* + \frac{1}{Re} \boldsymbol{\nabla}^{*2} \boldsymbol{v}^* + \rho^* \frac{1}{Fr} \boldsymbol{g}^* \tag{4.7}$$

with the boundary condition defined as:

$$\boldsymbol{n} \cdot [\boldsymbol{\sigma_2^*} - \boldsymbol{\sigma_1^*}] = \boldsymbol{n}(\boldsymbol{\nabla}^* \cdot \boldsymbol{n}). \tag{4.8}.$$

The dimensionless numbers in Eq. (4.7) are $We = \rho \bar{U}^2 R/\gamma$, $Re = \rho \bar{U} R/\gamma$ and $Fr = U^2/gR$.

All the results presented in the following are given in terms of dimensionless quantities. For the sake of simplicity, the superscript * is omitted.

4.2 Software

The software used in this work is OpenFOAM (Weller, 1998), a free-to-use open-source software with extensive CFD and multiphysics capabilities. OpenFOAM uses a Volume-of-Fluid (VoF) method (Hirt, 1981) to model multiphase systems, which consists in considering the two immiscible

fluids as a unique fluid on the whole domain, but characterized by "changing" physical properties defined as follows:

$$\eta = \alpha\eta_1 + (1-\alpha)\eta_2 \tag{4.9}$$

$$\rho = \alpha\rho_1 + (1-\alpha)\rho_2 \tag{4.10}$$

where α is a volume fraction whose range of variability is between 0 and 1. The region of the domain occupied by the gas phase has $\alpha = 0$, whereas the region occupied by liquid phase has $\alpha = 1$. The interface is a thin volume where α value varies in the range [0-1] and the properties are averaged. The gas-liquid interface corresponds to $\alpha = 0.5$.

This approach is implemented in a group of solvers included in the OpenFOAM package. For incompressible phases, the solver is "interFOAM" that will be used to carried out the numerical simulations presented in this work. Its performances have been evaluated in the work by Deshpande *et al.* (2012) over a wide range of application. They concluded that interFOAM has:

- excellent mass conservation and acceptable advection errors;
- excellent performances in inertia-dominated flows ($We \gg 1$);
- discrete balance between pressure gradient and surface tension in surface tension-dominated flows;
- curvature computation presents a slight error with respect to analytical results, but in good agreement with experiments;
- high ability to capture the physics of capillary wave, Rayleigh breakup of a laminar jet and capillary retraction of a liquid jet.

4.3 Model equations

According to VoF method, the mass balance and the momentum equations presented above are re-written in dimensional form as:

$$\frac{\partial\rho}{\partial t} + \boldsymbol{\nabla}\cdot\rho\boldsymbol{v} = 0 \tag{4.11}$$

$$\frac{\partial\rho\boldsymbol{v}}{\partial t} + \boldsymbol{\nabla}\cdot(\rho\boldsymbol{v}\boldsymbol{v}) - \boldsymbol{\nabla}\cdot[\eta((\boldsymbol{\nabla}\boldsymbol{v}) + (\boldsymbol{\nabla}\boldsymbol{v})^T)] = -\boldsymbol{\nabla}p_d - (\boldsymbol{\nabla}\rho)\boldsymbol{g}\cdot\boldsymbol{z} + \gamma\kappa\boldsymbol{\nabla}\alpha \tag{4.12}$$

where $p_d = p - \rho\boldsymbol{g}\cdot\boldsymbol{z}$ is the piezometric pressure (where $\boldsymbol{g}$ and $\boldsymbol{z}$ are the gravity and position vectors, respectively), ρ and η are the density and the viscosity defined by Eqn. 4.9 and 4.10, γ is the surface tension and κ the mean curvature of the free surface, defined as:

$$\kappa = \boldsymbol{\nabla} \cdot \left(\frac{\boldsymbol{\nabla}\alpha}{|\boldsymbol{\nabla}\alpha|} \right) \tag{4.13}$$

Notice that the extra field needs to be specified through a proper evolution equation. In this regard, it is simply assumed that the local volume fraction is convected with the flow:

$$\frac{\partial \alpha}{\partial t} + \boldsymbol{v} \cdot \boldsymbol{\nabla}\alpha = 0 \tag{4.14}$$

This set of equations closes the problem under the hypotheses of incompressible fluids, and will be used both for the test cases and in Chapter 5. For later references, we will call this situation as an "incompressible (overall) liquid": the density of the overall liquid is supposed to vary significantly only "around" the interface between the two components.

If compressibility is taken into account, i.e., the densities spatially vary in the bulk of the two phases, two additional equations of state must be added to Eqs. (4.3)-(4.6). We will refer to this case as a "compressible (overall) liquid", i.e., where the overall density can vary throughout all space. We choose to relate the overall density to the pressure only and assume that only isoentropic transformations can occur. Hence, an energy balance is not needed and the two additional equations are (i) the "ideal fluid" equation of state of isoentropic transformations:

$$\frac{p}{\rho^{\gamma}} = constant \tag{4.15}$$

and (ii) the isoentropic formula giving the sound velocity c in the overall liquid in terms of density variations:

$$\left(\frac{\partial \rho}{\partial p} \right)\Big|_{s} = \frac{1}{c^2} \tag{4.16}$$

Notice that the latter equation has to be meant as a *local* equation, because the velocity of sound will depend on the local composition of the overall liquid. This complete set of equations, Eqn. (4.3)-(4.8), will be used in Chapter 6, where the dependence of sound velocity c on the local conditions of the overall liquid will also be specified.

4.4 Geometry and boundary conditions

The geometry of the problem is a cylindrical object (the nozzle) surrounded by air. The problem has been faced by exploiting axial symmetry: our control volume is a slice of a cylinder and is represented in Figure 26 (a), where the red region represents the liquid inside the nozzle and the blue region represents the air, that is also an example of initial condition. A cylindrical reference frame with x

and z the radial and axial directions, centered at the lower-left corner of the domain, is adopted. Of course, due to the axial symmetry, the coordinate θ is irrelevant. The nozzle is delimited by a solid wall (yellow in Figure 23 - b), the left boundary (dashed-dottted line) that is the axis of symmetry. The air domain is enclosed by open boundaries (blue lines). The liquid enters through the inlet boundary (green line).

The boundary conditions are:

- Inlet: imposed, laminar, fully developed velocity profile:

$$\boldsymbol{v} = (v_r, v_z) = \left(0, 2U(t)(1 - x^2)\right) \tag{4.17}$$

  where $U(t)$ is the mean velocity (in space) and will be defined in the next sections and x is the radial coordinate;
- Wall: no slip condition:

$$\boldsymbol{v} = \mathbf{0} \tag{4.18}$$

- Axis: axial symmetry condition
- Open boundaries:
  - outflow for both phases (Neumann conditions);
  - inflow for air (fixed value).

Dimensions are specified in Figure 26 (c). The domain length along the axial direction has been chosen arbitrarily, in order to observe the typical phenomena of jet formation. The radial length is the result of a convergence study as discussed below.

4.4.1 Choice of the control volume

The choice of the control volume has been optimized on the (dimensionless) radial length L, that is the width of the slice. Preliminary simulations have been carried out exploring the range between $L = 3$ and $L = 10$. Velocity and pressure profiles have been analyzed at different positions in the volume, obtaining an overlapping of the results. The results for axial velocity profiles for the cases $L = 10$ (the maximum dimension) and $L = 3$, at two different positions: $z = 17$ (after the nozzle) and $z = 43$ (in the pipe) are shown in Figure 27 and Figure 28. As visible from these figures, the curves perfectly overlap. We selected for the next simulations $L = 3$.

Regarding the axial length H, a similar check on the positions of upper and lower boundaries has been performed, but the final choice has been made preferring a wider domain, in order to catch significative variations of the stream radius when a time-varying inlet condition is applied.

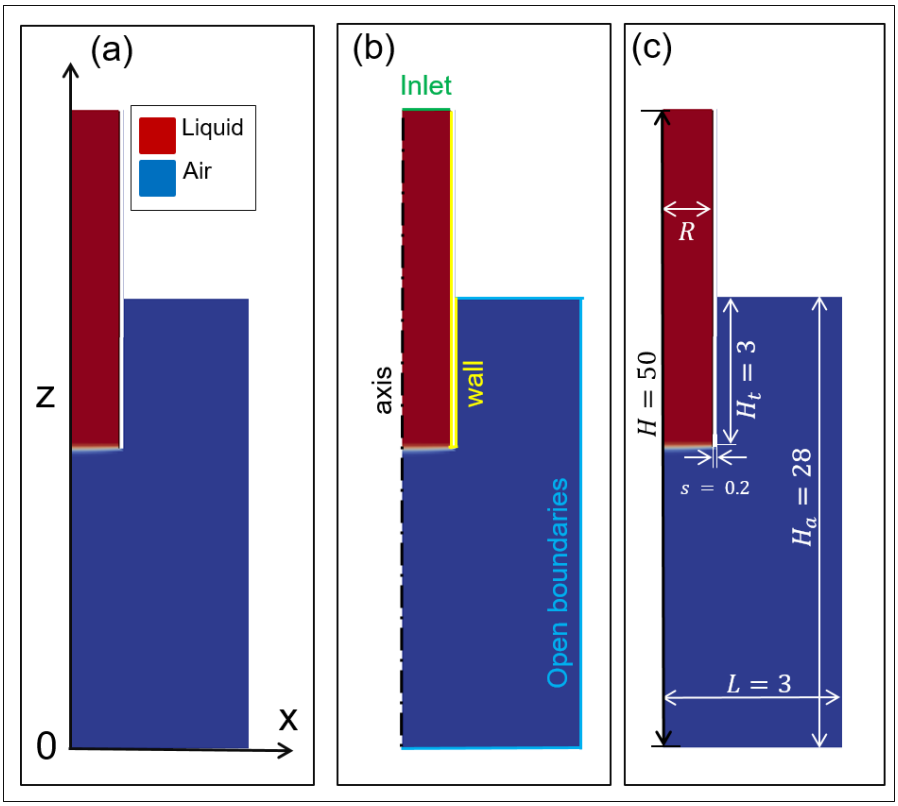

Figure 26: Geometry used in numerical simulations: a) Reference frame; b) Boundaries; c) Dimensions of the control volume.

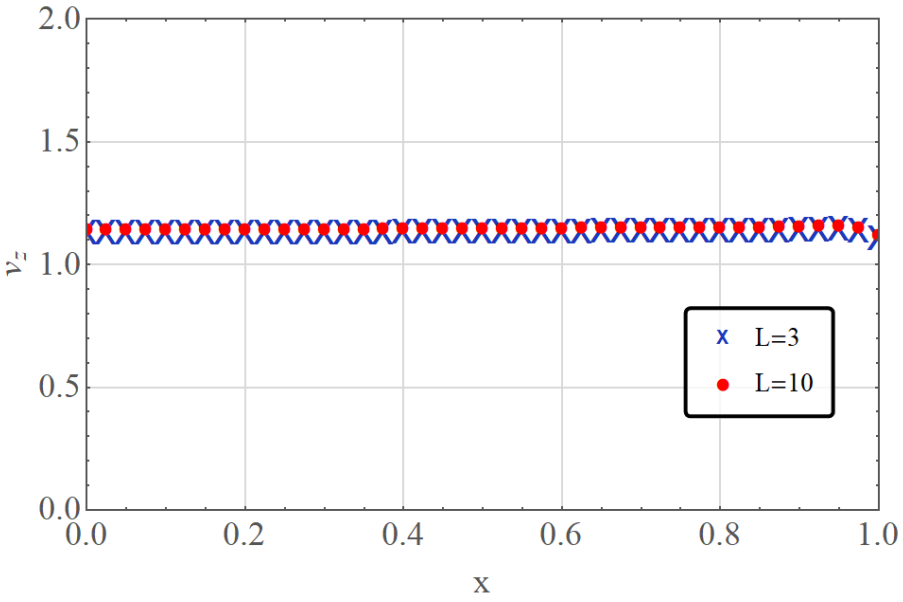

Figure 27: axial velocity profile, $z = 17$. ($Re = 10$, $Ca = 1.42$, $Oh = 0.378$)

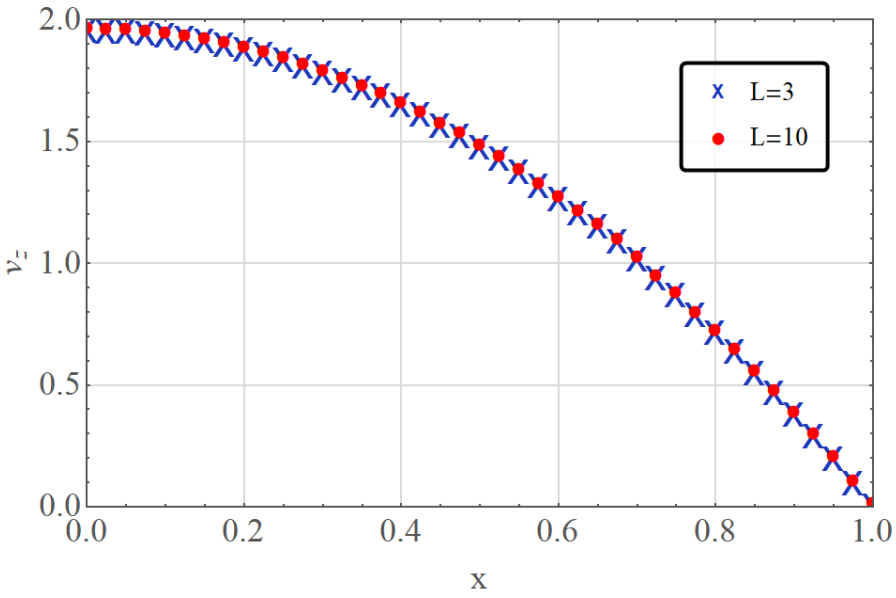

Figure 28: axial velocity profile, $z = 43$ ($Re = 10$, $Ca = 1.42$, $Oh = 0.378$).

4.5 Mesh and time convergence

Model equations are a set of partial differential equations. These equations are discretized using a Finite Volume Method, in order to determine the velocity field, $\boldsymbol{v}$, the pressure field, p, and the volume fraction field, α. To this end, the control volume needs to be discretized. It has been chosen a hexahedral mesh. A typical mesh is shown in Figure 29, where the dimensions of the elements are smaller in the part of the volume where liquid flow is expected (from the axis up to a radial position slightly higher than the nozzle radius) and larger moving far from it.

Mesh convergence has been checked for all the simulations presented in this work. In Figure 30, a typical mesh convergence plot is shown. Specifically, the axial velocity profile along the axis of symmetry is reported for different kinds of meshes. In the legend, the number of elements for each mesh is indicated. The profiles are very similar by a qualitative and a quantitative point of view. In order to quantify the differences, the relative error has been calculated for three different axial positions ($z = 5$, near the bottom exit; $z = 24$, just outside the nozzle; $z = 40$, inside the nozzle). The results are reported in Table 3. Figure 31 represents the values of the alpha field in the radial direction at $z = 24$, which goes from $\alpha = 1$ in the liquid to $\alpha = 0$ in the gas, for different meshes. Notice that the width of the transition region is reduced by using a finer mesh.

When time-varying inlet conditions are applied, a temporal convergence has been verified by decreasing progressively the delta t, found to be the limiting parameter in terms of computational

time. An example of time convergence is given in Figure 32, where the trend of the minimum radius r_{min} on time is represented for different Δt used in numerical simulations.

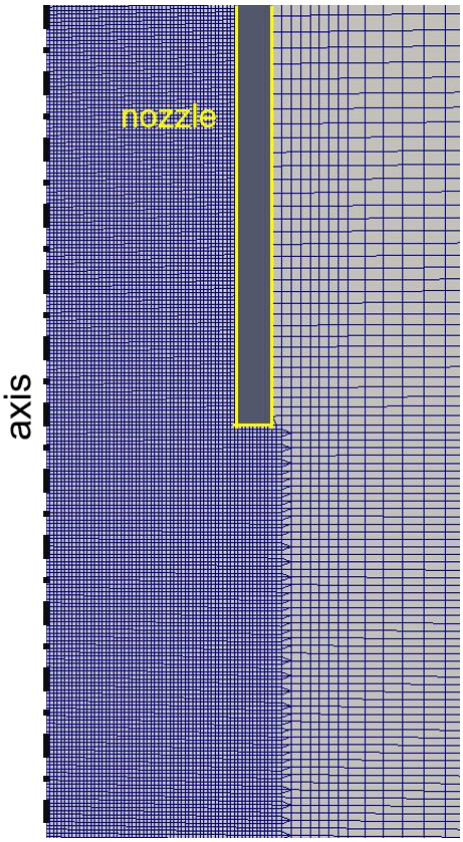

Figure 29: Spatial discretization using hexahedral elements (M1), zoom on the nozzle area.

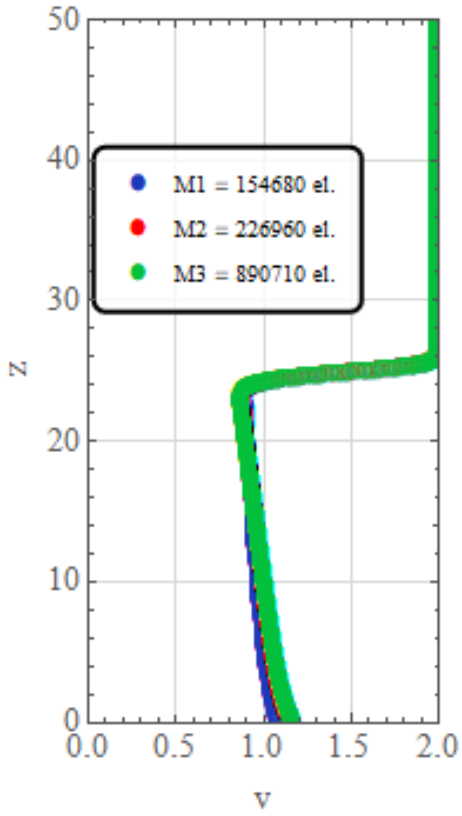

Figure 30: Axial velocity along the axis, for different meshes ($Re = 1$, $Ca = 14.2$, $Oh = 3.78$).

M1: 154680 elements		$z = 5$	$z = 24$	$z = 40$
M2: 226960 elements	**M1 vs M2**	3.9%	0.8%	0.6%
M3: 890710 elements	**M2 vs M3**	0.96%	0.4%	0.1%

Table 3: Relative errors for different discretizations.

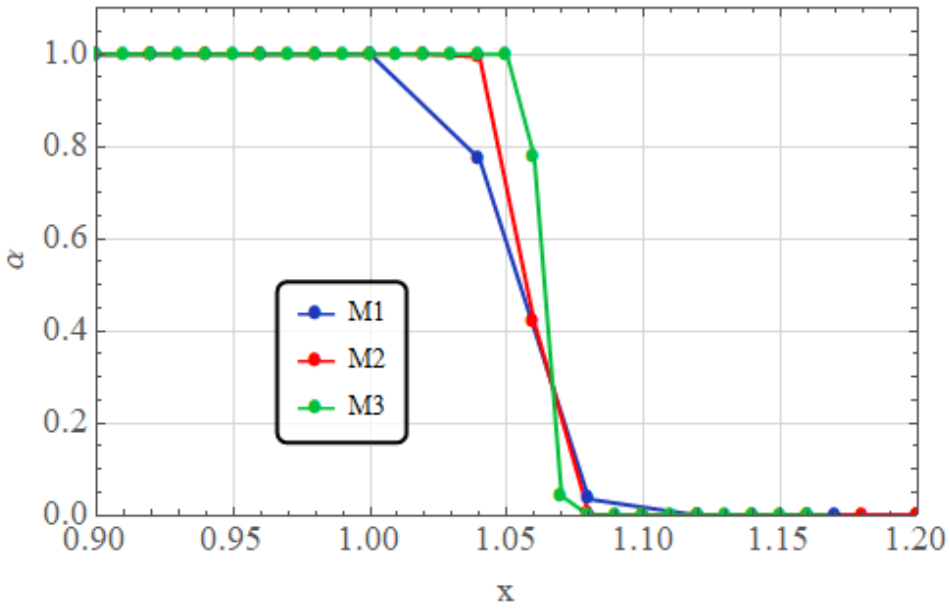

Figure 31: Interface sharpness. α values versus radial position x, $z = 24$ ($Re = 1, Ca = 14.2, Oh = 3.78$).

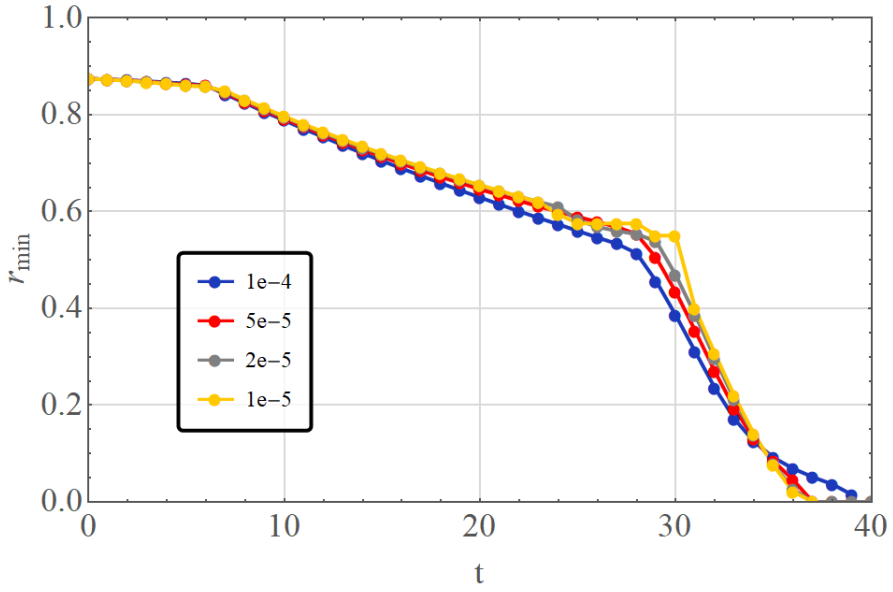

Figure 32: Temporal convergence, r_{min} versus time, for different Δt. ($Re = 10$, $Ca = 1.42$, $Oh = 0.378$).

4.6 Validation of the code

To test the capabilities of the solver, a Newtonian liquid under a steady-state feeding flow condition has been studied, starting from an initial condition where the fluid is at rest and fills the nozzle. At time zero, a constant velocity is imposed at the inlet, determining the formation of the jet. In this

stage, both the liquid density and the external air density have been supposed to be constant. Four test cases have been run with dimensionless parameters reported in Table 4.

A	$Re = 100$	$Ca = 0.142$	$Oh = 0.0378$	$We = 14.2$	$Bo = 0.14$
B	$Re = 10$	$Ca = 1.42$	$Oh = 0.378$	$We = 14.2$	$Bo = 0.14$
C	$Re = 1$	$Ca = 14.2$	$Oh = 3.78$	$We = 14.2$	$Bo = 0.14$
D	$Re = 0.1$	$Ca = 142$	$Oh = 37.8$	$We = 14.2$	$Bo = 0.14$

Table 4: Dimensionless parameters considered for the code validation test cases.

Notice that all the dimensionless numbers have been indicated, but only three of them are independent, i.e., Bo number together with two among Re, Ca, We and Oh. Each of them, as outlined previously, highlights a peculiar behavior of the flow.

All the presented cases are characterized by a laminar flow. The case A exhibits an inertia-dominated thinning regime; cases B, C and D exhibit a viscosity-dominated thinning regime. For these combinations of the dimensionless parameters, a continuous jet is expected at long times with a jet radius smaller or larger (die swell) than the nozzle radius for cases A-B and C-D, respectively (Middleman, 1961; Omodei, 1979; Clasen, 2011). The steady-state solutions obtained by our simulations are shown in Figure 33. Agreement is found both in terms of jet formation as well as for its shape. Indeed, in cases C and D, the die-swell effect is correctly predicted.

A quantitative comparison has been performed with the universal solution of the slenderness momentum equation calculated by Clarke (1968), on which validity has been recently discussed by Montanero *et al.* (2011). The solution is reported in terms a dimensionless velocity w' versus a dimensionless position z' defined as:

$$z' = z/L_0 \qquad \text{with} \qquad L_0 = 3^{2/3}(\eta^2/\rho\mathcal{F})^{1/3} \tag{4.19}$$

$$w' = w/w_0 \qquad \text{with} \qquad w_0 = (L_0\mathcal{F}/\rho)^{\frac{1}{2}} \tag{4.20}$$

where $\mathcal{F}$ represents the driving force that is assumed to be the gravitational force $\mathcal{F} = \rho g$.

The dimensionless momentum equation, in the case of neglecting surface tension effects, has the form (4.21) and satisfies boundary conditions (4.22) and (4.23):

$$w'\frac{dw'}{dz'} - w'\frac{d}{dz'}\left(\frac{1}{w'}\frac{dw'}{dz'}\right) = 1 \tag{4.21}$$

$$w'(0) = 0 \tag{4.22}$$

$$w'(\infty) \to \infty \quad \text{for} \quad z'(\infty) \to \infty \tag{4.23}$$

The solution has the form:

$$w' = \frac{2^{-1/3}Ai^2(\xi)}{Ai'^2(\xi) - rAi^2(\xi)} \qquad \text{with} \qquad \xi = 2^{-1/3}(z' - k),\ k = 2.94583 \tag{4.24}$$

where Ai and Ai' are the Airy function and its derivative.

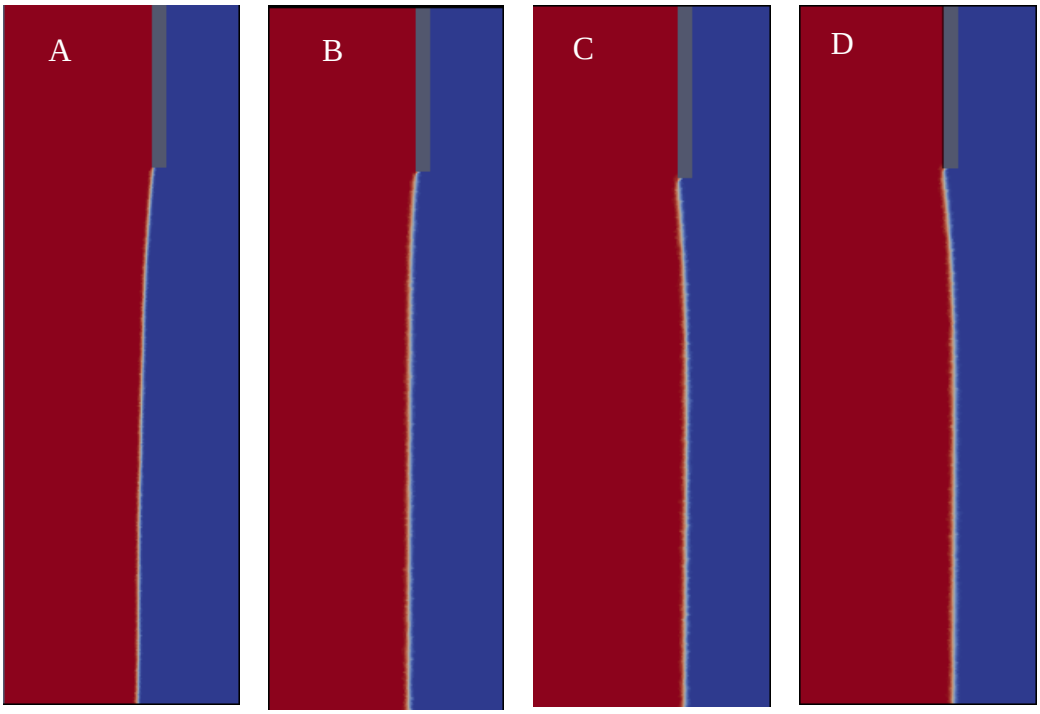

Figure 33: α field for cases A, B, C and D of Table IV. Red color represents liquid phase, blue color represents gas phase. Grey region is the nozzle, white line is the interface.

Montanero *et al.* (2011) compare this analytical solution with numerical results carried out by three-dimensional axisymmetric simulations of steady and incompressible Navier-Stokes equations in the ranges of *Re* [0.01-100] and *Fr* [0.02-10], obtaining a very good agreement (higher for an increasing *Re* number and a decreasing *Fr* number). We would like to point out that the numerical method used by Montanero *et al.* solves the equations in the liquid phase only and, hence, it is a different approach as compared to the one used in this work (volume of fluid).

In Figure 34, the universal solution (solid line) is compared with our numerical results (symbols) for the four aforementioned test cases. A very good quantitative agreement is observed even for a small Re number (liquid D).

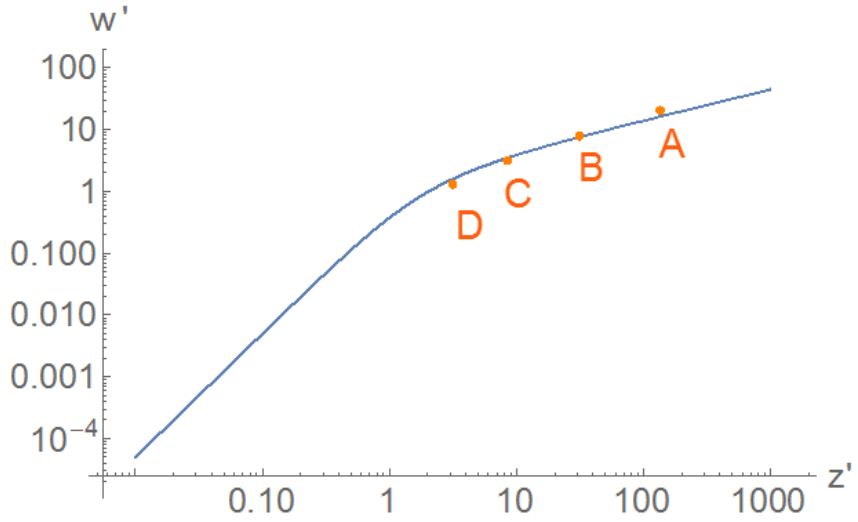

Figure 34: Comparison between universal solution (blue line) (Clarke, 1968) and numerical results for the four test cases summarized in Table IV (orange dots). In the graph, w' and z' are a dimensionless velocity and distance from the nozzle (see main text). The numerical results evaluated at $z = 24$.

5. Results - Effect of a time-varying feeding condition

In this chapter, we analyze the behavior of an isothermal Newtonian liquid exiting a nozzle subjected to a time-varying feeding condition. In all these simulations, the fluid is assumed to be incompressible.

5.1 Problem statement

The behavior of different fluid A and B, presented in the previous chapter, has been analyzed. Their properties and dimensionless numbers are specified in Table 5.

Fluid	$\eta\ [Pa\ s]$	$\rho\ [Kg/m^3]$	$\gamma\ [Kg/s^2]$	Ca	Re	We	Oh
A	10^{-2}	1000	0.07	0.14	100	14.3	0.038
B	0.1	1000	0.07	1.4	10	14.3	0.38
Air	$1.48E-5$	1					

Table 5: Physical properties and dimensionless numbers.

The geometry used in numerical simulations has been presented in Section 4.2. For each operating condition, we run a preliminary simulation with a constant flow rate in order to achieve a stable, continuous jet. After the jet has reached a steady-state condition, the velocity profile in inlet is progressively inverted. Specifically, the profile is kept parabolic with mean velocity that varies linearly between U_0 (liquid flows downwards) and $-U_0$ (fluid rises the nozzle). U_0 is the characteristic velocity and has been used for the dimensionless numbers in Table 7. Several slopes have been investigated as reported in Table 6 (dimensionless) and represented in Figure 35.

Initial mean velocity, U_0	1
Slope 1	$5\,e-3$
Slope 2	$10\,e-3$
Slope 3	$20\,e-3$
Slope 4	$40\,e-3$
Slope 5	$80\,e-3$

Table 6: Characteristic of the feeding flow-rate.

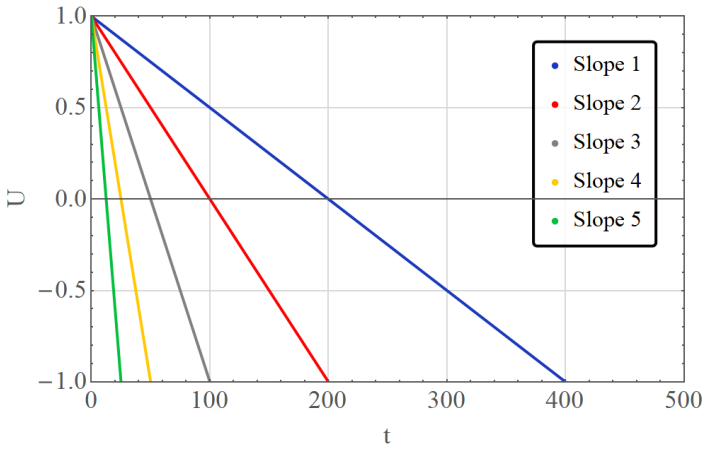

Figure 35: Feeding flow-rate versus time.

5.2 Results

In this section, we show the effect of the time-varying inlet boundary condition on the jet dynamics and its break-up. The behavior of two different Newtonian fluids (A and B, physical properties

specified in Table 5) at different slopes of the velocity inversion (seen Table 6) is investigated. Results are shown and discussed in terms of minimum dimensionless radius r_{min} and dimensionless time to breakup $\tau_b = t - t_b$, t_b is the breakup time. τ_b is 0 when breakup occurs and $\tau_b > 0$ before breakup.

5.2.1 Fluid A ($Oh \ll 1$)

The evolution of interfaces on time is represented in Figure 36 in terms of dimensionless radius versus dimensionless quota for a slow (left panel), medium (middle panel), and fast (right panel) sucking-back rate. Different colors represent different values of τ_b. The graphs show that the sucking-back velocity strongly influences the position of the pinch point that "rises" towards the nozzle as slopes increase. The interfaces near the pinchoff is also found to exhibit a two cones configuration, where the upper angles with respect to the axis are 103° (slope 3) and 107° (slope 5), and lower angles 10° (both slope 3 and slope 5), differing from 112.8° and 18.1°, as found by Day (1998).

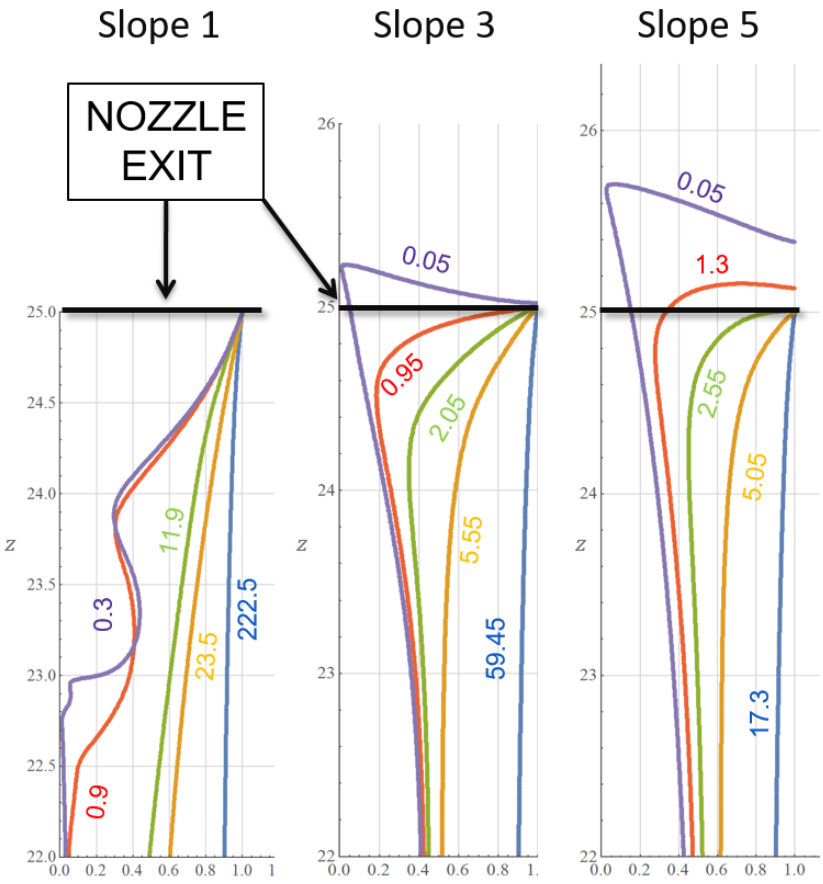

Figure 36: Temporal evolution of interfaces, represented for different slopes at $Oh = 0.038$. x-axis represents the dimensionless radius, y-axis the dimensionless vertical quota. Nozzle exit is placed at $z = 25$. Each color represents a different value of τ_b (labelled).

The trends of the minimum radius r_{min} experienced by the liquid stream versus the dimensionless time τ_b for a low-viscosity liquid are shown in Figure 37. Notice that breakup is approached moving on right to left with τ_b axes. Different colors represent different slopes. Regardless of the imposed velocity variation, the well-known inertial regime, where $r_{min}{\sim}\tau^{2/3}$, is reached (represented as the black line in the graph), meaning that the dynamics bringing the system to breakup is still local. The instant such that the system enters the breakup regime as well as the constant relating r_{min} to τ depend on the sucking-back velocity: as the slopes increase, such inertial regime is reached earlier. Notice that the transition from inertial to viscous-inertial regime for a fluid when $Oh \ll 1$ is expected to occur when $r_{min}{\sim}0.001$. However, the finest mesh resolution used in our simulations is $\Delta x{\sim}0.005$, setting a cut-off of the dynamics leading to breakup. Nevertheless, the estimated time to breakup in the viscous-inertial regime is $\tau_b{\sim}0.005$, which is negligible as compared to the duration of the inertial regime ($\tau_b{\sim}1$).

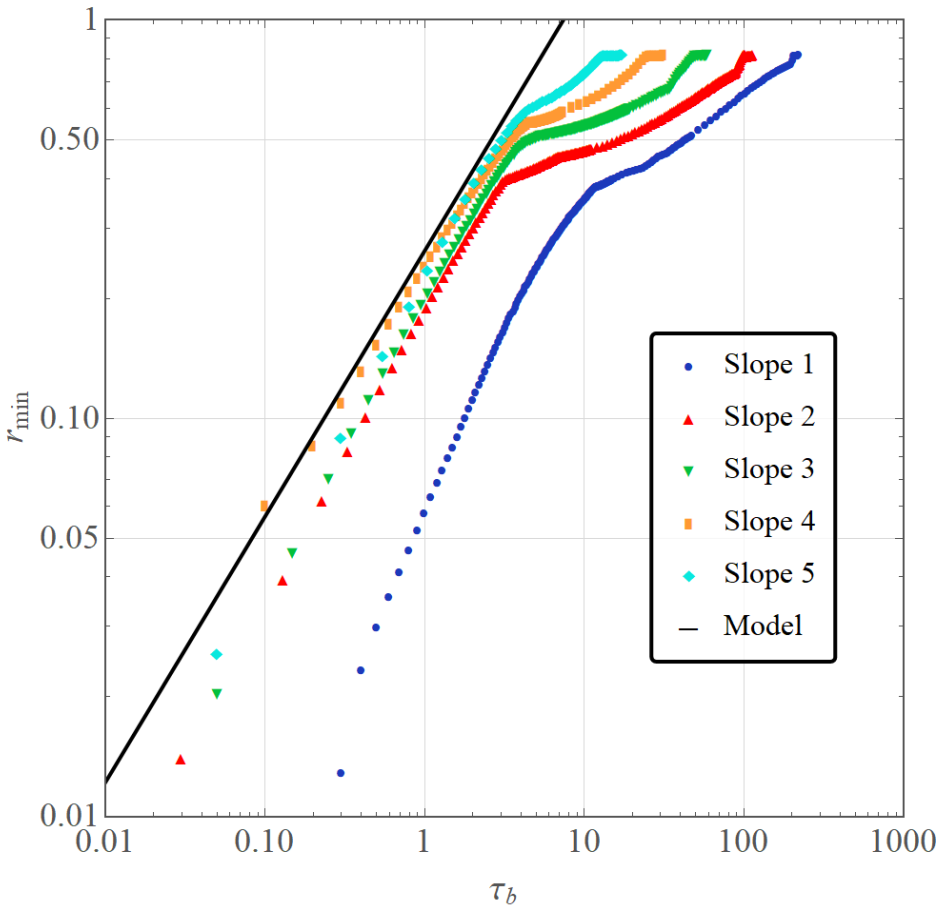

Figure 37: Values of dimensionless r_{min} versus dimensionless time τ_b, for different slopes at $Oh = 0.038$. Symbols represent numerical results, the black line is the theoretical prediction for inertial regime $r_{min}{\sim}\tau_b^{2/3}$ (Day, 1998).

5.2.2 Fluid B ($0.1 < Oh < 1$)

In Figure 38 we represent the interfaces at different times (dimensionless radius versus dimensionless quota) for three different sucking back velocities. Again, as slopes increases the pinch point position gets higher, even more as compared with the low-Oh case.

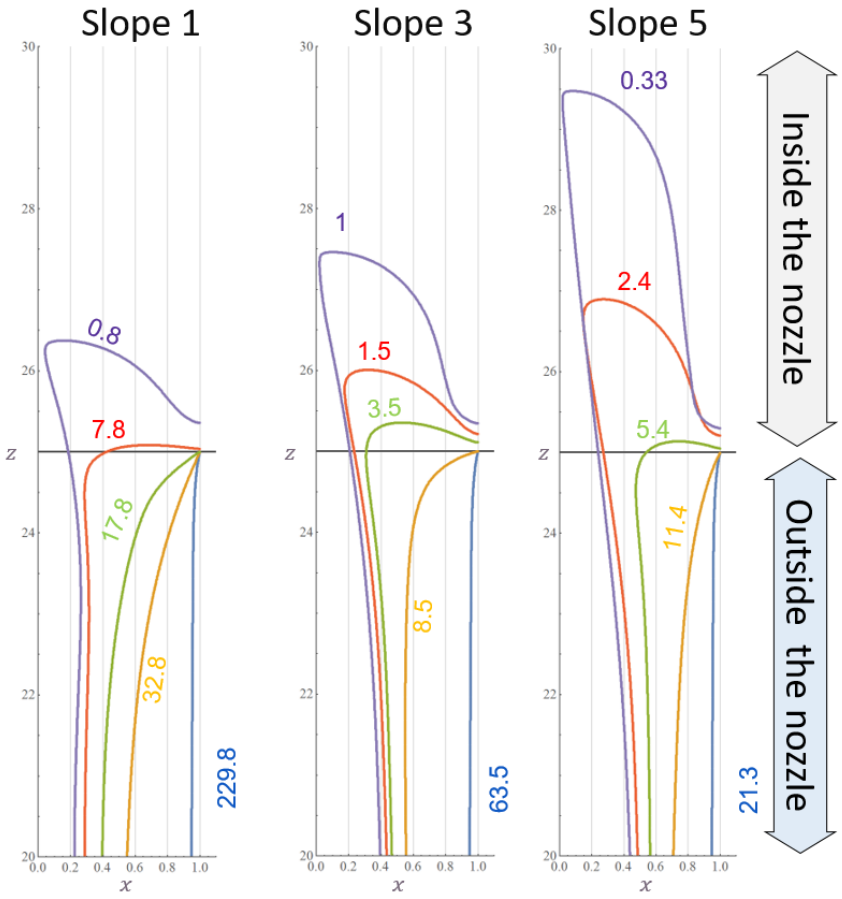

Figure 38: Temporal evolution of interfaces, represented for different slopes at $Oh = 0.38$. x-axis represents the dimensionless radius, y-axis the dimensionless vertical quota. Nozzle exit is placed at $z = 25$. Each colour represents a different value of τ_b (labelled).

The trends of minimum radius r_{min} versus dimensionless time τ_b for a liquid characterized by a medium viscosity are reported in Figure 39. The data at long times (i.e., short τ_b) clearly show a linear dependence of r_{min} on τ_b, characteristic of dominant viscous effects, found for liquids with $Oh > 0.2077$, as reported by Middleman (1966, 1995). Concerning the dynamics before the viscous regime, a faster decreasing of the filament radius as sucking back velocity increases as well as a delay of the onset of the regime are observed. The latter agrees with the results of Castrejón-Pita (2015) (appearance of the viscous regime when r_{min}~0.1) but they are discrepant from Li & Sprittles (2016)

(expected transition at r_{min}~0.01). As before, the breakup is "artificially induced" by the resolution of the mesh used and it is not possible to observe the transition to viscous-inertial regime.

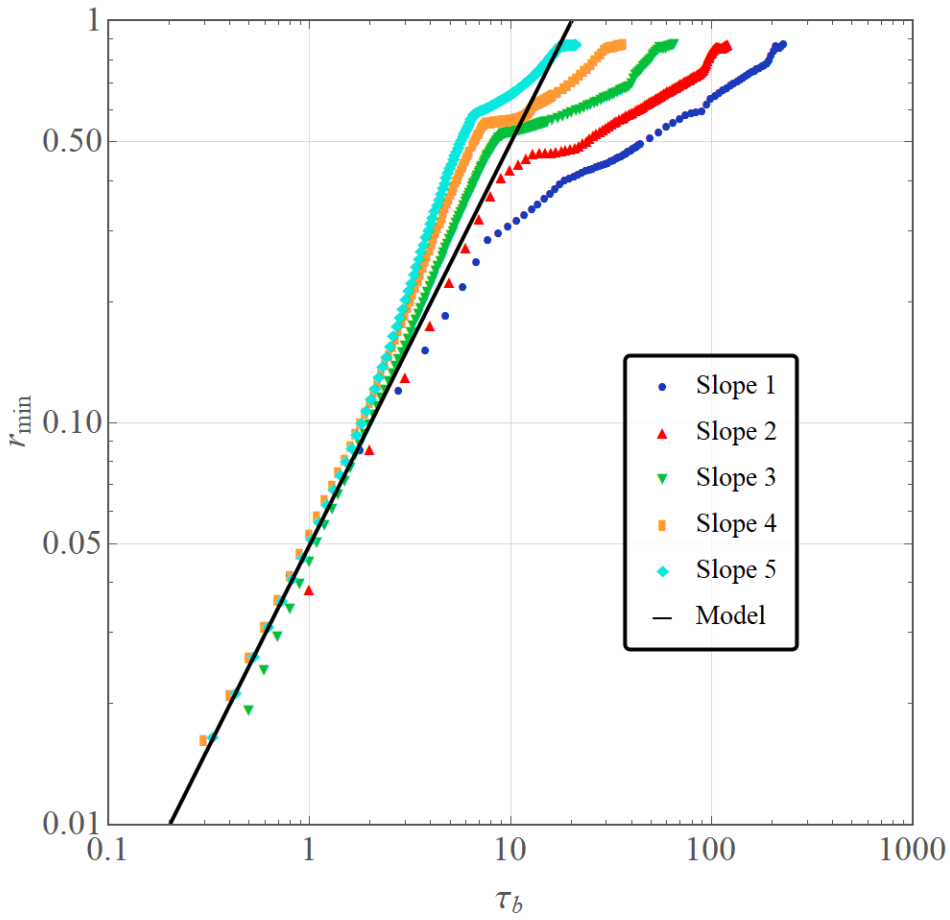

Figure 39: Values of dimensionless r_{min} versus dimensionless time τ, for different slopes at Oh=0.38. Symbols represent numerical results, the black line is the theoretical prediction for viscous regime $r_{min} = 0.0709\,\tau_b/Ca$ (Papageorgiou, 1995).

5.2.3 Concluding remarks

In this chapter, numerical simulations with a Volume of Fluid method have been used to study the dynamics of an incompressible Newtonian liquid exiting a nozzle, undergoing a time-varying inlet condition. A linear variation of the velocity on time has been taken into account. The behavior of two fluids, characterized by a different balance between inertial and viscous forces ($Oh = 0.038$ and $Oh = 0.38$), with different slopes of the inlet mean velocity variation has been considered. The filament thinning dynamics has been analyzed and compared to the scaling laws available in the literature for stationary flow conditions.

Our simulation results show that the dynamics leading to breakup is local and well-described by asymptotic regimes derived for steady-state conditions. On the other hand, the flow rate inversion seems to strongly influence the pre-thinning dynamics as well as the thickness of the filament such that the system enters into the breakup regime and the position of pinch point.

6. Results – Effect of compressibility and comparison with experiments

In real filling operations, air can be trapped during the process. As remarked in the previous sections, even a slight amount of air may have significant effects on the flow behavior of the liquid exiting a nozzle. In this section, we address the effect of the time-dependent flow rate on the breakup of a continuous liquid jet with different conditions of aeration of the liquid. The simulation results are compared with experiments where a real dosing system is considered. We first provide a description of the experimental materials and methods, including the description of the apparatus and the procedure adopted to measure the aeration. Then, we describe the implementation of the compressibility in the simulations. Finally, the comparison between experimental and numerical results is shown and discussed.

6.1 Experiments

6.1.1 Materials and methods

Experiments have been carried out at Brussels Innovation Center, the European Research Development Center for the Fabric and Home Care Global Business unit for P&G. The experimental apparatus (named “dosing stand” and shown in Figure 40) is intentionally built as a small pilot plant: pipe lengths are longer than needed, but just one nozzle is fed by the liquid. It is composed of:

- a Human Machine Interface (HMI), where input parameters (inlet velocity profiles, number and frequency of cycles) are entered and transmitted to the pump;
- a vessel, where the liquid is stored at a fixed pressure, controlled by a manometer. Its bottom is connected to a gear pump by means of a flexible pipe;
- a gear pump, that imposes the time-varying flow rate to the fluid. Pressure is controlled both before and after the pump by pressure sensors, and a second flexible pipe (length 1.7 m, internal diameter 6 mm, thickness 1 mm) connects the pump to a rigid duct with a 90° round elbow (internal diameter 4 mm), where the nozzle is attached vertically. At the end of the pipe both temperature and pressure are measured;
- a transparent nozzle (length 5 cm, internal diameter 2.8 mm);
- a 350 fps camera that records the liquid stream exiting the nozzle focusing on the nozzle exit and orthogonally aligned with the rigid nozzle block;
- a computer station, connected to the sensors, whose recordings are managed by *Labview*, a commercial software designed for data acquisition and analysis;
- the Red Bird computer, connected both to the pump and the high-speed camera, whose generated data allow the match between stream behavior and input velocity profile. Moreover, these data can be synchronized to *Labview* data thanks to the overlapping of common outputs (time-varying flow rate), so the correspondence of pressure profiles with stream behavior on time can be obtained;
- a 240 fps camera, that records the nozzle block and the liquid stream and has a larger view with respect to 350 fps camera. Since it’s not synchronized to any other devices, it allows to study the behavior of the stream by a qualitative point of view.

The behavior of different Newtonian fluids, pumped with a time-dependent feeding flow, in different conditions of aeration, has been studied. Four liquids have been considered, based on a mixture of glycerol, water and propylene glycol (P-diol), and they are reported in Table 7 with their

corresponding properties and dimensionless numbers. We would like to remark that the dimensionless numbers contain the jet velocity that, in our cases, depends both on time and on the section of the pipe. In this stage, the velocity experimented by the flow at the nozzle during the jet phase has been considered. The characteristic dimension used in dimensionless numbers is the nozzle radius. As just discussed, the experimental outputs are recordings of the stream exiting the nozzle: in order to enhance the contrast of frames, few drops of pure dark dye have been added to the mixtures, with not negligible effects on viscosities, whose values slightly deviate from those available in the literature. Therefore, each fluid has been rheologically characterized with an Ares-G2 Rheometer (TA INSTRUMENTS, 2017).

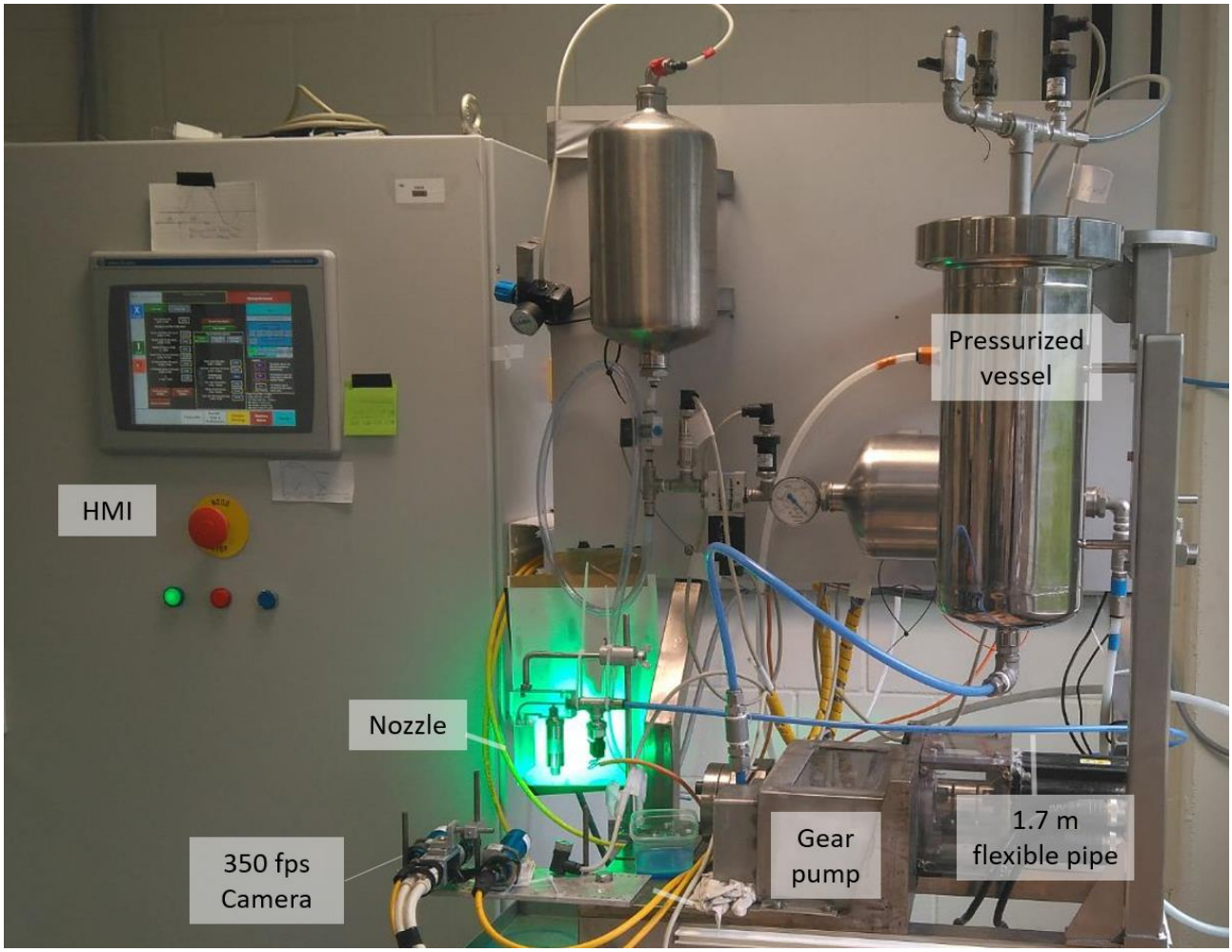

Figure 40: Dosing experimental apparatus.

The liquids have been processed with two different feeding flow time-varying profiles (here in after, cam profile 1 and 2, respectively), shown in Figure 41 and Figure 42, dimensionless. They are

characterized by a first rapid increasing of the flow rate up to reach a constant value. The velocity corresponding to such a value ($v = 4.4\ m/s$) is used in the calculation of dimensionless numbers. This short "stationary phase" is followed by a rapid decreasing of the flow rate. When the profile reaches the *x*-axis, the flow inverts its direction, i.e., the fluid is sucked back by the pump. Finally, the pump is stopped and the flow rate gets back to the zero-value, determining the end of the cycle. The two different cam profiles are characterized by the same total amount of liquid exiting the nozzle (i.e., same area between the profiles and the *x*-axis), but different velocities in sucking-back phase (faster for cam profile 1 and slower for cam profile 2).

Mixture	**Composition**	$\eta\ [Pa\ s]$	$\rho_0\ [Kg/m^3]$	$\gamma\ [Kg/s^2]$	Ca	Re	We	Oh
1	**60 % Glycerol 40 % Water**	0.0157	1153.5	0.068	1.03	460	951	0.047
2	**85 % Glycerol 15% Water**	0.122	1222	0.065	8.39	62.5	1054	0.366
3	**80 % Glycerol 20% P-diol**	0.61	1212	0.059	46.3	12.5	1151	1.92
4	**99 % Glycerol 1% Water**	0.79	1259	0.063	56.1	10	1120	2.37

Table 7: liquids used in experiments and their properties

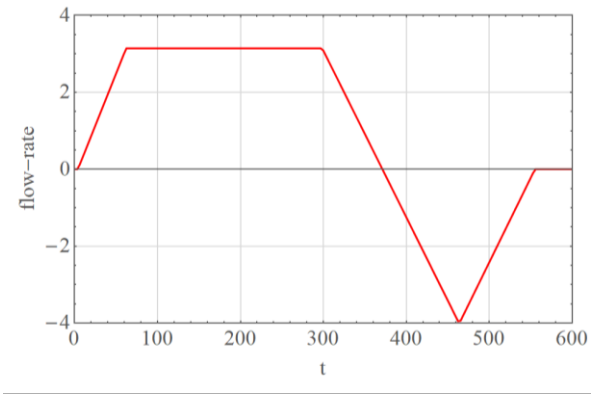

Figure 41: Cam Profile 1.

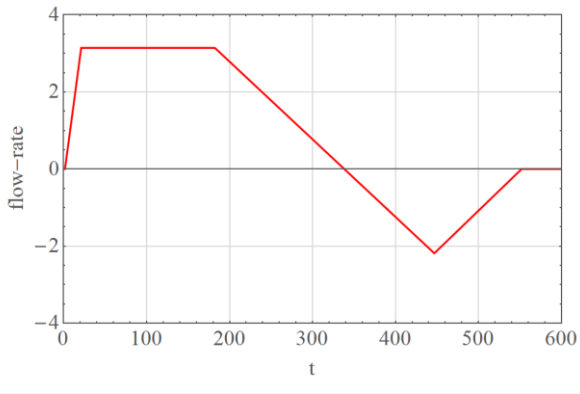

Figure 42: Cam Profile 2.

6.1.2 The aeration measurements

A relevant aspect we considered is the effect of the aeration on the jet break-up dynamics. To this aim, different conditions of aeration have been considered as follows:

- Not aerated sample: the liquid has been loaded into the vessel and left at rest in order to permit to bubbles eventually entrapped during pouring to get out. The vessel has been then closed and pressurized at 1.5 atm, to ensure the proper functioning of the pump and to avoid the coalescence of air bubbles at the same time. Then, the liquid has been flushed at constant flow rate (10 mL/sec) in order to fill uniformly the pipeline and to get it free from air bags. Finally, experiments with time varying inlet conditions have been run in two tranches: we impose the cam profile 1, we stop the system, and then we impose the cam profile 2. No further aeration between the two tranches of experiments has been performed.
- Aerated sample: the liquid previously aerated has been loaded into the vessel, closed, pressurized at 1.5 atm, and flushed at constant flow rate (10 mL/sec). Then, experiments have been run, with the same procedure as for not aerated sample.

The amount of air of the samples has been indirectly measured as a result of density variations. Densities have been measured with the density cup method, weighting 100 mL of liquid filling a calibrated stainless cup, both during experiments in different conditions of aerations (ρ_{aer}) and after a centrifuge (ρ_{dear}) of the same sample. The effect of temperature on density variations has also been considered and densities of centrifuged samples have been measured at different temperatures, in order to obtain $\rho_{deaer}\ (T)$. The resulting amount of air has then been calculated as:

$$\%\ air = \frac{\rho_{aer}(T_{exp}) - \rho_{dear}(T_{exp})}{\rho_{dear}(T_{exp})} \tag{6.1}$$

This method is clearly unappropriated when the air is present in the form of bubbles that would ideally exit the liquid phase according to the well-known Stokes solution (Stokes, 1880):

$$u_{\infty} = \frac{1}{18}\frac{g\ d_e^2(\rho_l - \rho_g)}{\mu_l} \tag{6.2}$$

where d_e is the equivalent bubble diameter (diameter of a sphere of the same volume as the bubble), μ_l the dynamic viscosity of the liquid, ρ_l the density of liquid and ρ_g the density of gas.

Therefore, densities measured during experiments are affected by a dynamic component, due to the inability to "freeze" the system, justifying the differences between the values obtained right after the aeration (red dots, Figure 51) and those obtained after the experiments (yellow dot, Figure 51), taken

with a time lapse of the order of minutes. Moreover, experiments have been run imposing cam profile 1 and cam profile 2 (in this order), and that's why the deviation between aerated and not aerated samples is lower for cam profile 2. The quantitative information given by density cup method will be then correlated with a qualitative analysis of the frames recorded by high-speed cameras in next sections.

As just discussed, we consider both liquids without added air and liquids where air has been intentionally added. To limit as much as possible the air initially present in the pipeline, we flush the liquid at a constant, continuous flow rate before running experiments. Unfortunately, a pure liquid is never observed, as we would expect in the case of not aerated sample. Indeed, from an accurate analysis of the frames recorded during our experiments, we found small, isolated bubbles in the liquid phase of not aerated samples, as shown in Figure 43 in the case of Mixture 2 and Mixture 4 (bubbles are surrounded by white circles). Then, the incompressible fluid hypothesis needs to be removed even when a "pure" liquid is considered. A compressible model must then be considered in the numerical modeling, as described in the next section.

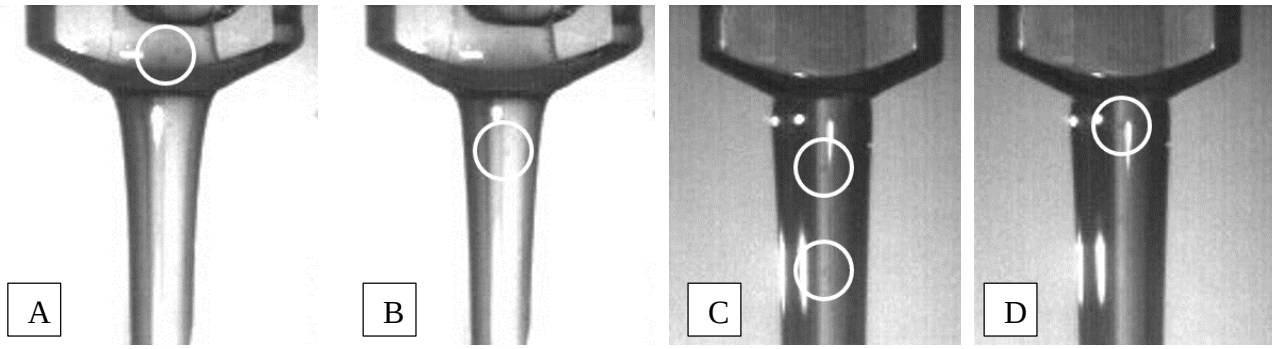

Figure 43: Isolated bubbles in not aerated samples, highlighted by white circles. A and B refer to Mixture 2, C and D refer to Mixture 4.

6.2 Simulations

The software used in numerical simulations has been presented in Chapter 4. In this part of the work, we want to simulate the dynamics of a Newtonian liquid with entrapped air. In this section, we show the model used for the compressible phase and the geometry used in simulations.

6.2.1 A new model for the air-liquid system

The issues related to the coexistence of two different phases in pipelines with hydraulic transients have been presented and discussed in section 2.8, where the correlation between sound velocity and

composition (Eq. 2.9) has been shown. From Eq. 4.16, that expresses the sound velocity in terms of density variations, we obtain for the liquid phase, in dimensional form:

$$\frac{d\rho_1}{dp} = \left(\rho_{air}(p)\phi_{air}(p) + \rho_{liq}(1-\phi_{air}(p))\right)\left(\frac{\phi_{air}(p)}{\rho_{air}(p)c_{air}^2(p)} + \frac{(1-\phi_{air}(p))}{\rho_{liq}c_{liq}^2}\right) \tag{6.3}$$

where ρ_1 is the density of the resulting biphasic system (modelled as an homogeneous liquid), ρ_{air} is the air density, ρ_{liq} the pure liquid density, ϕ_{air} the air volume fraction, c_{air} the air sound velocity and c_{liq} the pure liquid sound velocity, and their dependence on pressure is here made explicit:

$$\rho_{air} = \rho_{0,air}\left(\frac{p}{p_0}\right)^{1/\gamma} \tag{6.4}$$

$$\phi_{air} = \left(\frac{p_0}{p}\right)a_0 \tag{6.5}$$

$$c_{air} = \sqrt{\gamma\frac{p}{\rho_{air}}} \tag{6.6}$$

where p_0 a reference pressure, a_0 the air volume fraction at the reference pressure, γ is the isoentropic constant.

The differential Eq. 6.3 can be analytically solved with the boundary condition:

$$\rho_1(p_0) = \left(\rho_{air}(p_0)\phi_{air}(p_0) + \rho_{liq}(1-\phi_{air}(p_0))\right) \tag{6.7}$$

In Figure 44 the solution $\rho_1(p)$ is shown with a red solid line for a system where $a_0 = 0.5\%$, $c_{liq} = 1800\ m/s^2$, $\rho_{liq} = 1222\ kg/m^3$, $\gamma = 1.4$, $\rho_0 = 1\ Kg/m^3$, $p_0 = 1\ atm$. The analytical expression of such solution is quite complex and not suitable to be implemented in a numerical code. However, many high-order terms can be neglected, at least in the range of our interest. We end up to the following the approximate solution $\rho_{1,app}(p)$:

$$\rho_{1,app}(p) = \rho_{1,c} + a\ p + \frac{b}{p} \tag{6.8}.$$

reported as dashed black line in Figure 41. In Eq. (6.8), $\rho_{1,c}$, a, and b are constants obtained from the solution of Eq. (6.3). Unfortunately, OpenFOAM standard solvers for compressible flows only deal with constant values of sound velocities, i.e., with a density linearly dependent on the pressure, which is not the case of Eq. (6.8). Hence, the standard version of the adopted solver has been modified and recompiled. The customized solver is reported in Appendix A.

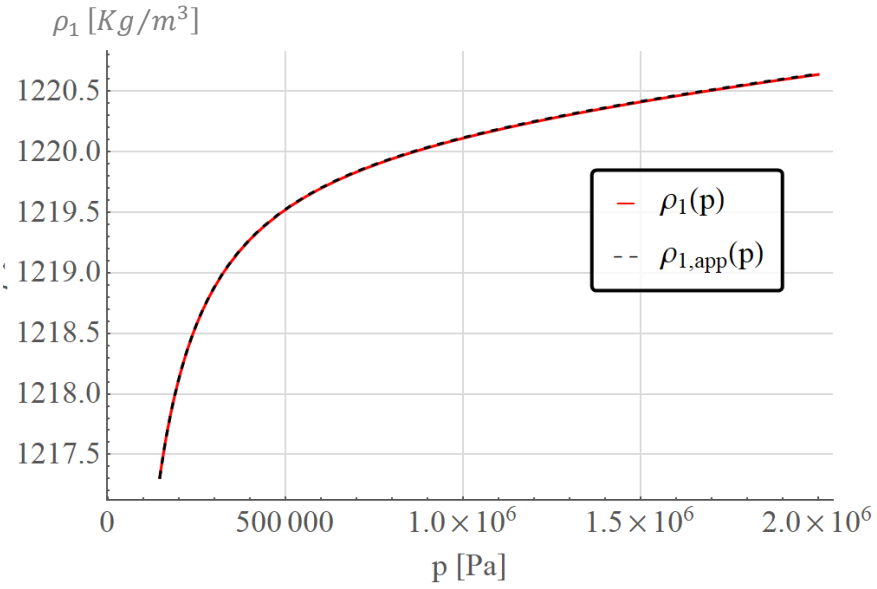

Figure 44: Solution of Eq. 6.3 of boundary conditions 6.7, for a system where $a_0 = 0.5\ w/w$, $c_{liq} = 1800\ m/s^2$, $\rho_{liq} = 1222\ kg/m^3$, $\gamma = 1.4$, $\rho_0 = 1\ Kg/m^3$, $p_0 = 1\ atm$ (solid red line) compared with its approximated solution $\rho_{1,app}(p) = \rho_0 + a\,p + \frac{b}{p}$.

6.2.2 Geometry

The simulations presented in the previous Chapter refereed to an incompressible liquid. This assumption assures that the flow rate imposed at the pump is instantaneously transmitted to the whole fluid volume in the pipeline. Hence, only the pipe portion near the nozzle needs to be simulated. If compressibility is relevant, the scenario changes as the entrapped air drastically reduces the mixture speed of sound (see section 2.8) and the liquid near the nozzle needs a certain time to "react" to any flow rate variation imposed at the pump. Although such a time delay is very small, it is comparable to the characteristic filling time and, as such, it must be carefully accounted for. As consequence, the whole filling system from the pump to the nozzle, consisting of a flexible pipe and the nozzle block (schematically represented in black in Figure 45), must be simulated. Notice that the geometry is composed of two cylindrical parts connected by a 90° round elbow. Only the last part of the pipe is parallel to the gravity (green arrow in Figure 42). In principle, a 3D geometry of a flexible pipe is needed. To reduce the computational effort, we assume that: (i) gravity only acts on the vertical final portion of the pipe, i.e., the liquid in the horizontal pipe is not affected by gravity, (ii) the pipe is rigid. The first assumption allows to use two axisymmetric domains, one for the horizontal (no gravity) and one for the vertical (with gravity) pipe regions, leading to a huge saving in terms of computational

effort. Hence, no 90° round elbow is simulated and the domain is an axisymmetric pipe with gravity affecting only the last part.

Figure 45: Conceptual scheme of the geometry used in simulation. The graph on the left represents the imposed time-dependent flow rate.

These assumptions do not alter significantly the motion inside the pipeline, where no large differences in height are observed, allowing, on the other hand, to consider the contribution of the gravity force inside the nozzle, on the free-surface flow, and on the breakup dynamics where gravity is relevant. The resulting control volume is conceptually close to the one presented in section 4.2, with the differences staying in lengths and sections concerning the closed channel. The dimensions used are congruent with the real ones and the simulated geometry with correspondent lengths is represented in Figure 46 A and B, adimensionalized with the nozzle radius, $R = 1.4\,mm$. The non-uniform gravity field is not a standard feature in OpenFOAM and its implementation has required a second modification and recompilation of the solver. Further details are reported in Appendix A.

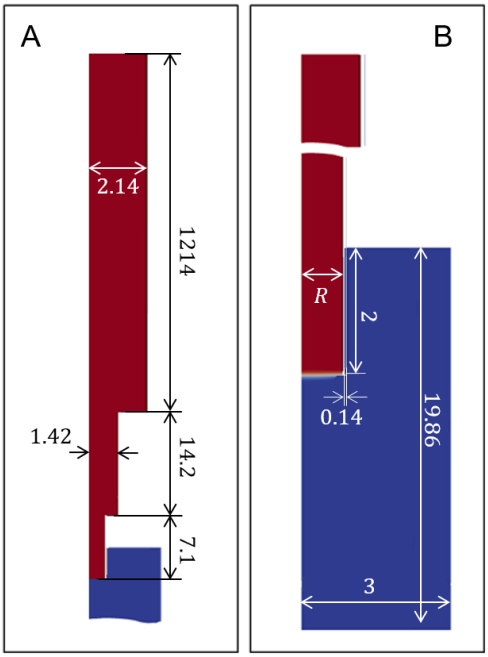

Figure 46: Geometry used in numerical simulations with dimensionless lengths.

6.2.3 Initial condition

The initial condition consists in a tube partially filled by the liquid phase as schematically shown in Figure 47, where the gray area represents the liquid and the white area represents the "empty" part. As discussed above, the geometry used in numerical simulations consists of a *straight* pipe, with two abrupt contractions.

At zero time, the pump starts to push the liquid towards the nozzle and then into the pouch. The filled part (gray in Figure 44) has been calculated by a mass balance: the amount of liquid *pushed* by the pump is represented in Figure 48 by the *total* green area (with and without stripes). At time $t = t_i$ the flow rate is inverted and the pump works to suck the liquid back by an amount equal to the red area in Figure 48. This area corresponds to the striped green area whereas the amount of liquid exiting the nozzle is represented by the unstriped green area.

Then, the empty part of the pipe (white area in Figure 47) is simply given by:

$$\int_{t_i}^{t_f} Q(t)\, dt.$$

Figure 47: Sketch of initial condition used in simulations.

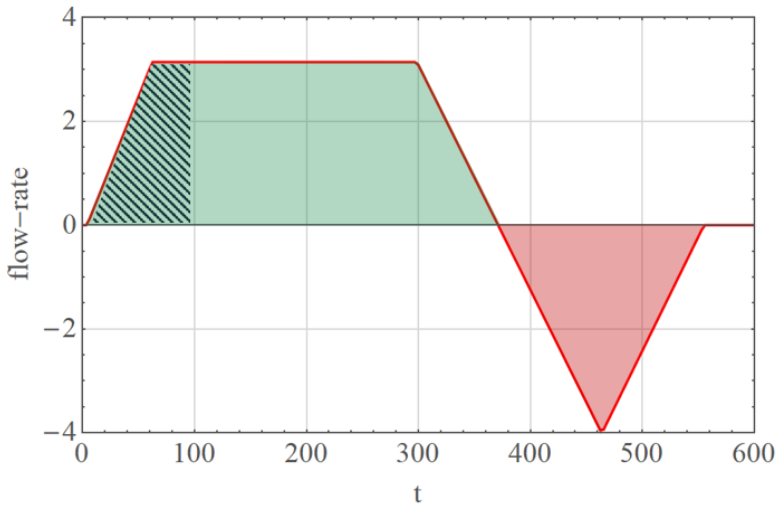

Figure 48: Flow rate imposed by the pump (cam profile 1). Striped green area and red area are equal and represent the empty part of the pipe. Unstriped green area represents the amount of liquid that exits the nozzle.

6.3 Results and discussion

In this section, we present the experimental and numerical results of the breakup of a jet undergoing an industrially used varying feeding flow cycle for the four mixtures described above. We first describe the experimental observations of the liquid dynamics exiting the nozzle. Then, we compare experiments and simulations in terms of time evolution of radius of the stream measured at a fixed distance from the nozzle.

6.3.1 Experiments

6.3.1.1 Mixture 1 (Oh=0.047)

Figure 49 shows a sequence of frames representing the first stages when a non-aerated mixture issues into ambient air. Although this initial phase leads to the formation of a stable jet, the stream is characterized by a liquid core surrounded by small droplets that is undesired in dosing industrial applications. Figure 50 reports a sequence of snapshots during the breakup phase. In Figure 48A, millimetric air bubbles into the transparent nozzle block are visible. Assuming that the bubble diameter is 1 mm (the nozzle block dimension is 4 mm) and the validity of the Stokes law, they need less than 1 second to get out once the liquid has filled the density cup.

Figure 49: Formation of the jet (mixture 1, cam profile 1, not aerated sample, 240 fps).

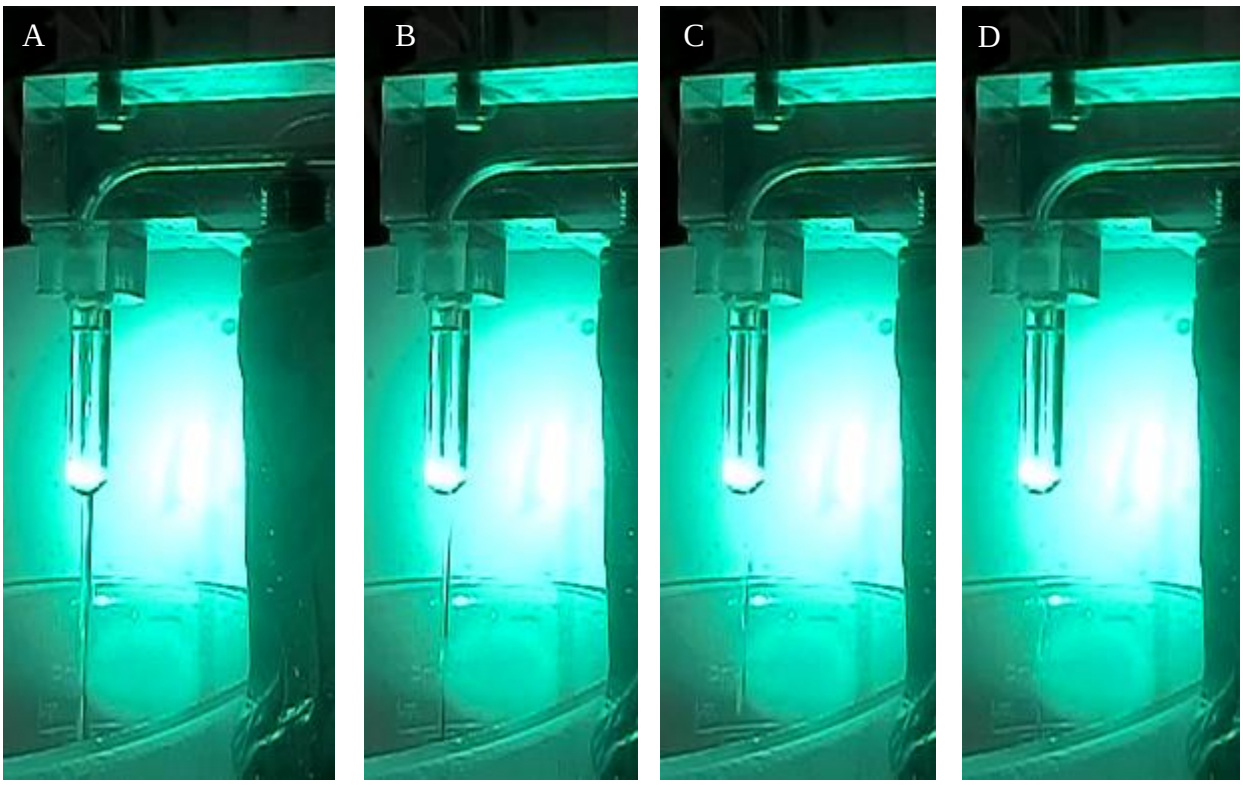

Figure 50: Breakup phase (mixture 1, cam profile 1, not aerated sample, 240 fps). A: Bubbles in the nozzle block; B, C and D: Breakup of liquid stream localized in two different positions with consequent formation of undesired satellite droplets (dripping).

Hence, air bubbles present in the system quickly escape the liquid phase and the only traces we have are the frames from high speed cameras. Figure 50B, C and D also show the presence of a Taylor bubble rising the transparent nozzle block. As it will be shown later, although the approximation of "dispersed air" falls, simulations predict very well the evolution of the stream radius on time as long as the "right" amount of air is hypothesized, mostly dependent on number and size of air bubbles. Notice that the air bubbles shown in Figure 50A will exit the pipe in the following pushing phase (whose phase will be similar to the sequence represented in Figure 51) and other bubbles will arrive with the following cycle. The frames represented in Figure 50B, C and D show a breakup phenomenon localized at two different points of the liquid stream, with the consequent formation of undesired satellite droplets. Literature reports a satellite-free dispensing when $Oh \gg 1$ (Clasen, 2011).

Finally, Figure 51 reports the mixture density measured for the not aerated sample (blue dot) and the aerated sample, both right after the aeration (red dots) and after the experiments (yellow dot). Grey dots represent the densities of the centrifuged sample at different temperatures, fitted by the dashed line. The correspondent measured amount of air is between 1% and 1.5% right after the aeration.

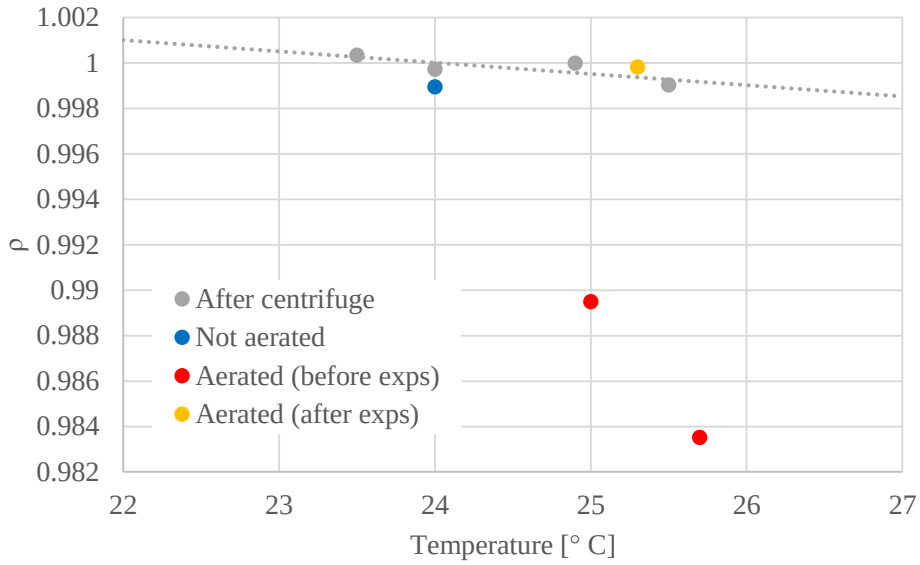

Figure 51: Density measurements for mixture 1: grey dots represent densities of centrifuged sample, blue dot is the density for not aerated sample, red dots are the densities for aerated sample (measured right after the aeration) and yellow dot is the density after the experiments.

6.3.1.2 Mixture 2 (Oh=0.366)

Figure 59 shows an image sequence corresponding to the instants just after the pump starts to push the mixture 2 liquid. As soon as the nozzle block is filled, small isolated droplets (highlighted in Figure 59 with an orange circles) start to exit the nozzle, which is undesired in dosing operations. The liquid jet exiting the nozzle is smoother for this mixture, and the liquid jet is immediately stable.

In Figure 53 the sequence of frames of breakup phase is reported. The pinching occurs right after the nozzle and the liquid continues to fall vertically as a unique string of liquid, where no satellite droplets are formed.

Finally, density cup results are represented in Figure 54, with an amount of air of 1.45% for the aerated sample (red dots).

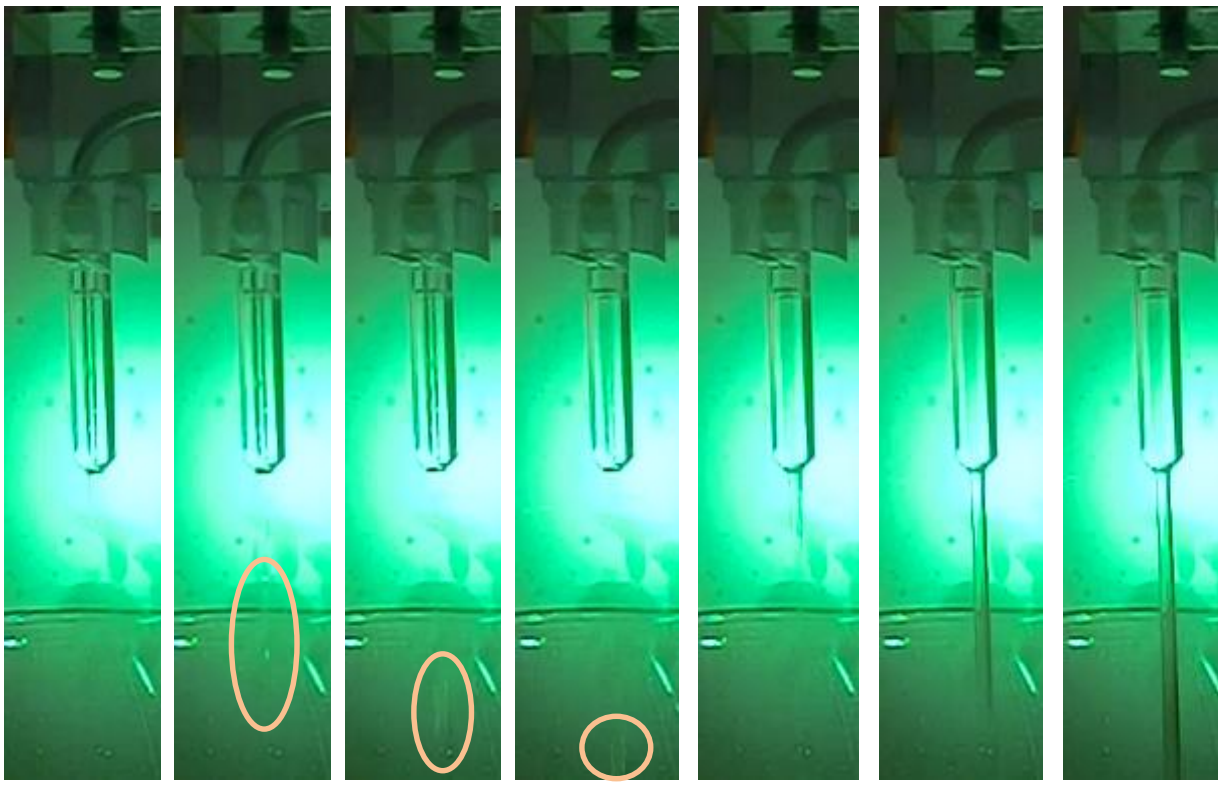

Figure 52: First stages of dosing cycle (mixture 2, cam profile 1, not aerated sample, 240 fps). Orange circles highlights the formation of small droplets exiting the nozzle before a stable jet is formed.

Figure 53: Breakup phase (mixture 2, cam profile 1, not aerated sample, 240 fps).

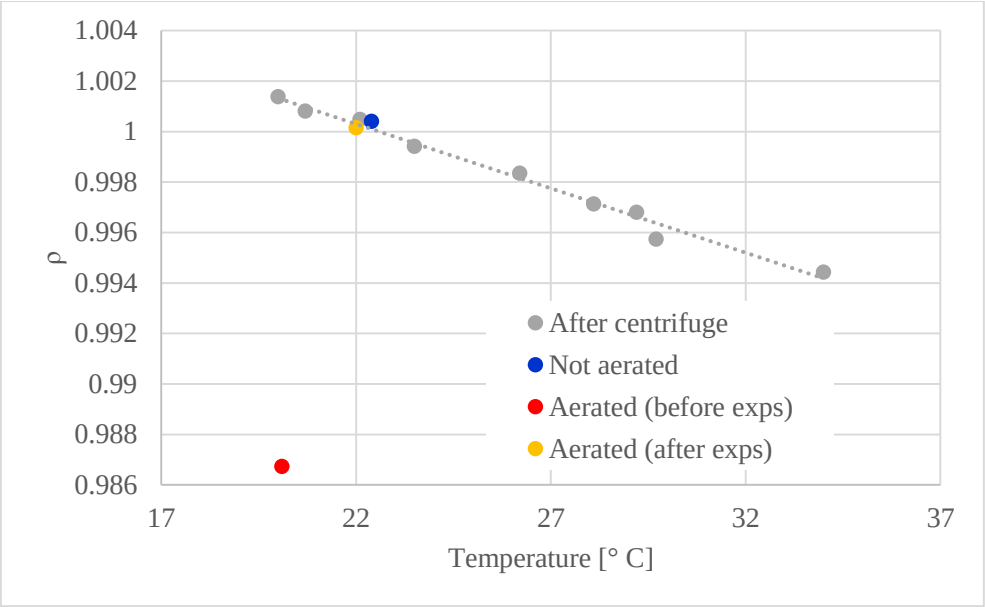

Figure 54: Density measurements for mixture 2: grey dots represent densities of centrifuged sample, blue dot is the density for not aerated sample, red dots are the densities for aerated sample (measured right after the aeration) and yellow dot is the density after the experiments.

6.3.1.3 Mixture 3 (Oh=1.92)

The liquid stream exiting the nozzle in the case of a highly viscous liquid (high Oh number) is not affected by the issues previously shown (formation of small droplets at the beginning of the cycle). Indeed, as shown in the sequence of frames in Figure 36 referring to mixture 3, the front moves forward towards the exit and a smooth "cylinder" is formed at once. Density measurements shown in Figure 56 report an amount of air for the aerated sample between 0.8% and 0.5% (before experiments, red dots in Figure 56). Regarding the value obtained after the experiments, even if the deviation from centrifuged sample is almost of the same order of experimental error, we found a lower density, suggesting the presence of traces of air (on average less than 0.1%). Results from 350 fps camera, focused on the nozzle exit, also give an evidence of the air in form of small bubbles in the aerated sample (shown in Figure 58), which is absent in the not-aerated sample (shown in Figure 57).

The breakup phase is represented in Figure 59, where a sequence of images shows the persistence of a thin filament, while the liquid front is rising the nozzle thanks to sucking back phase. With respect to previous cases, the frequency of frames is reduced by one half, then the dynamics exhibited has been found to be much slower, as can be inferred by the lower slopes in Figure 68 and Figure 69. As a result, this liquid capillary (whose dimensions can be appreciated in Figure 60) is found to be unstable in a quiescent gaseous ambient as demonstrated by oscillations in last frames of Figure 59. The breakup occurring in the external air close to the nozzle causes the formation of a minuscule

droplet (surrounded by a red circle in Figure 60-D), with no dramatic effects on the success of the industrial process.

Figure 55: Formation of the jet (mixture 3, cam profile 1, not aerated sample, 240 fps).

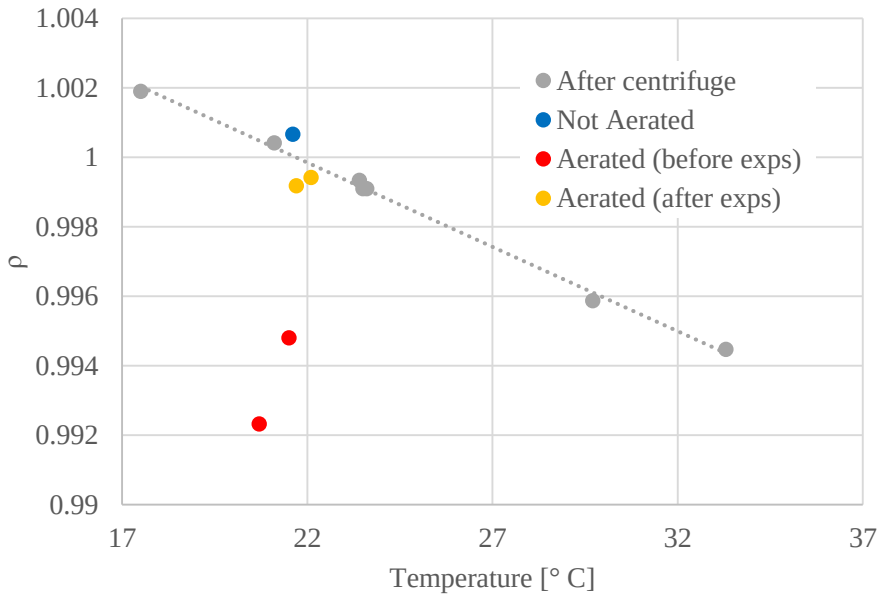

Figure 56: Density measurements for mixture 3: grey dots represent densities of centrifuged sample, blue dot is the density for not aerated sample, red dots are the densities for aerated sample (measured right after the aeration) and yellow dot is the density after the experiments.

Figure 57: liquid exiting the nozzle (thinning phase), not aerated sample.

Figure 58: liquid exiting the nozzle (thinning phase), aerated sample.

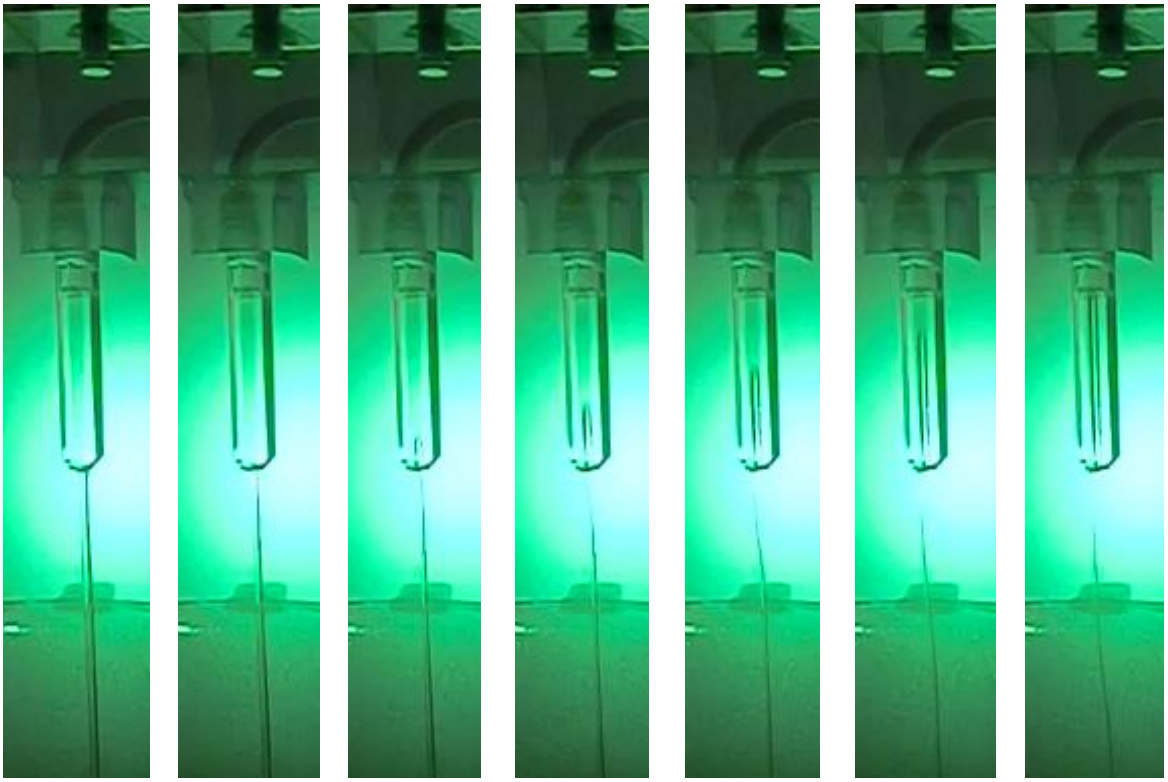

Figure 59: Breakup phase (mixture 3, cam profile 1, not aerated sample, 120 fps).

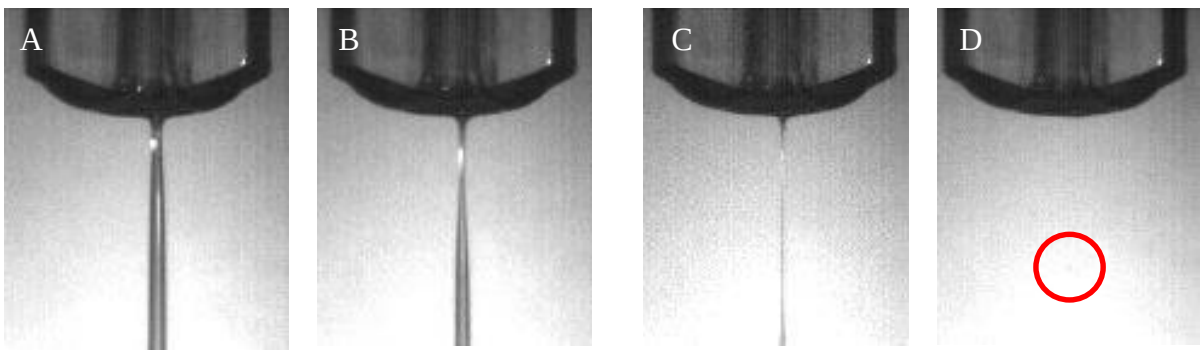

Figure 60: Breakup phase, zoom on nozzle exit (mixture 3, cam profile 1, not aerated sample, 87.5 fps).

6.3.1.4 Mixture 4 (Oh=2.37)

Mixture 4 behaves like mixture 3 by a qualitative point of view, and has the following features:

- formation of a stable, smooth jet;
- entrapment of air bubbles in the aerated sample (see Figure 61 and Figure 62);
- longer breakup dynamics due to onset of viscous regime.

By a quantitative point of view, the amount of air measured in the aerated sample is between 0.5% and 1% (densities reported in Figure 63), whereas the *dosing time*, defined as the time needed to perform a complete cycle, from the beginning of the pushing phase till the breakup, increases by approximately 15%.

Figure 61: liquid exiting the nozzle (thinning phase), not aerated sample.

Figure 62: liquid exiting the nozzle (thinning phase), aerated sample.

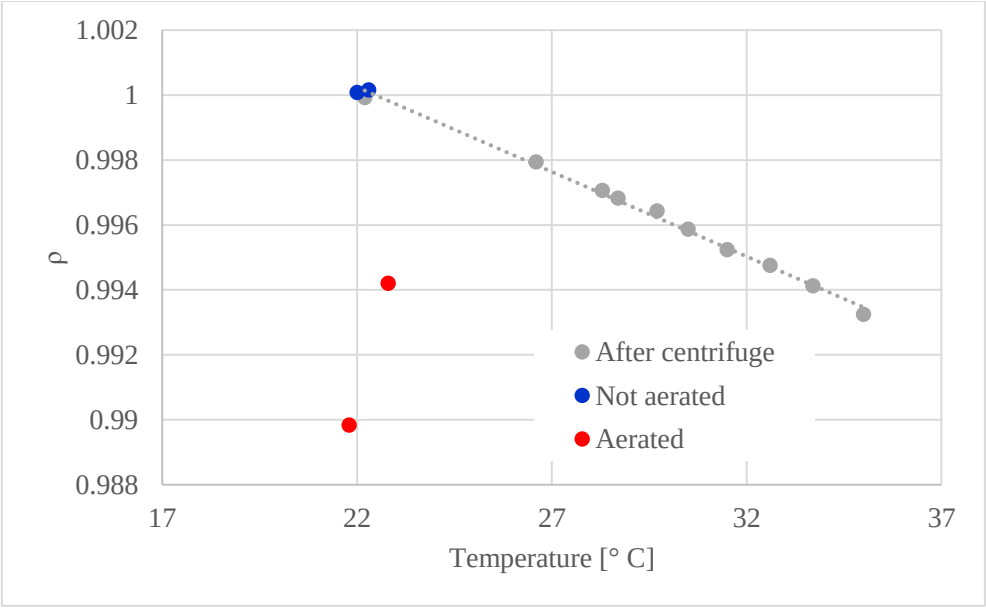

Figure 63: Density measurements for mixture 4: grey dots represent densities of centrifuged sample, blue dot is the density for not aerated sample, red dots are the densities for aerated sample (measured right after the aeration).

6.3.2 Comparison between experiments and simulations

In this section, we compare the experimental and simulation results in terms of time evolution of the dimensionless radius of the stream measured at a distance R from the nozzle. To understand the effect of the compressibility due to the entrapped air, we consider the case of incompressible liquid (interFoam solver) and the case of compressible homogeneous phase (customized solver) with different amounts of dissolved air.

The results are shown from Figure 64 to Figure 71 for the four mixtures and the two cam profiles. The experimentally measured stream radius is represented by blue open circles for unaerated sample and red open circles for the aerated sample. The numerical predictions are shown as closed circles where different colors correspond to different volume fractions of dissolved air (the gray symbols refer to an incompressible liquid). On the same graphs, the grey solid line represents the cam profile applied by the pump and must be read on right *y*-axis. Figures 49-53 refer to mixtures 3 and 4 characterized by $Oh \gg 0.2$ for which a viscous filament is expected (Clasen et al., 2011). Hence, in these plots, the dashed black lines are the prediction of the evolution of the stream radius according to Papageorgiou (1995).

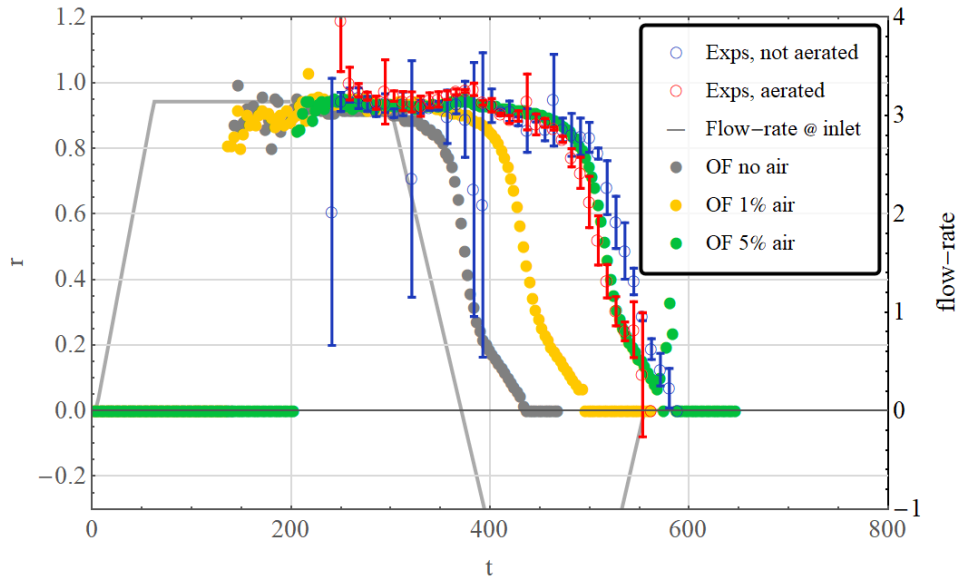

Figure 64: Results for mixture 1, Cam Profile 1. Solid, gray line represents the Cam Profile (referring to the flow-rate scale on the right); the dots represent the stream radius at a distance R from the nozzle: yellow dots for 1% disperse air in liquid, green for 5%, gray dots for pure liquid mixture, blue empty dots with error bars represent the experimental results of a not aerated mixture and red empty dots the experimental results of an aerated mixture.

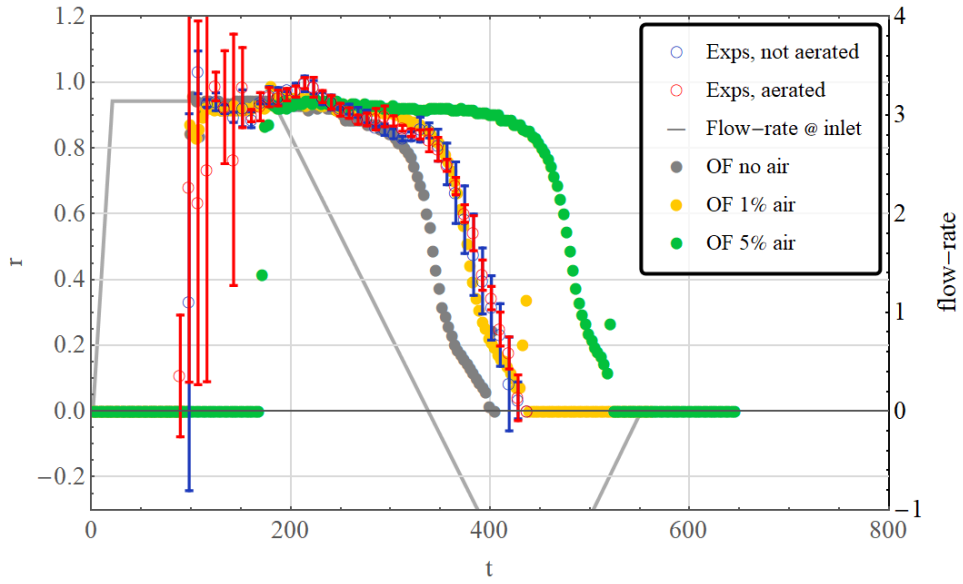

Figure 65: Results for mixture 1, Cam Profile 2. Solid, gray line represents the Cam Profile (referring to the flow-rate scale on the right); the dots represent the stream radius at a distance R from the nozzle: yellow dots for 1% disperse air in liquid, green for 5%, gray dots for pure liquid mixture, blue empty dots with error bars represent the experimental results of a not aerated mixture and red empty dots the experimental results of an aerated mixture.

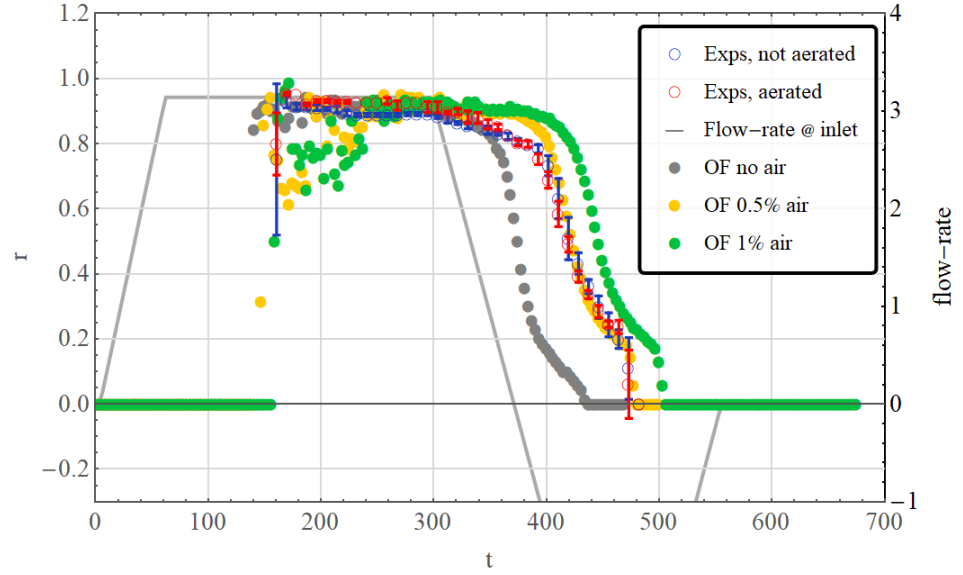

Figure 66: Results for mixture 2, Cam Profile 1. Solid, gray line represents the Cam Profile (referring to the flow-rate scale on the right); the dots represent the stream radius at a distance R from the nozzle: yellow dots for 0.5% disperse air in liquid, green for 1%, gray dots for pure liquid mixture, blue empty dots with error bars represent the experimental results of a not aerated mixture and red empty dots the experimental results of an aerated mixture.

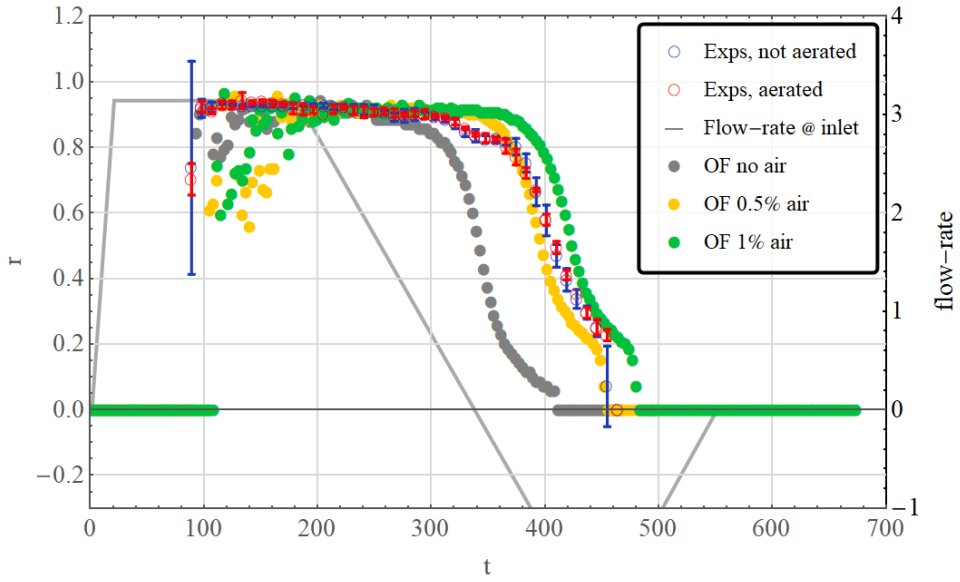

Figure 67: Results for mixture 2, Cam Profile 2. Solid, gray line represents the Cam Profile (referring to the flow-rate scale on the right); the dots represent the stream radius at a distance R from the nozzle: yellow dots for 0.5% disperse air in liquid, green for 1%, gray dots for pure liquid mixture, blue empty dots with error bars represent the experimental results of a not aerated mixture and red empty dots the experimental results of an aerated mixture.

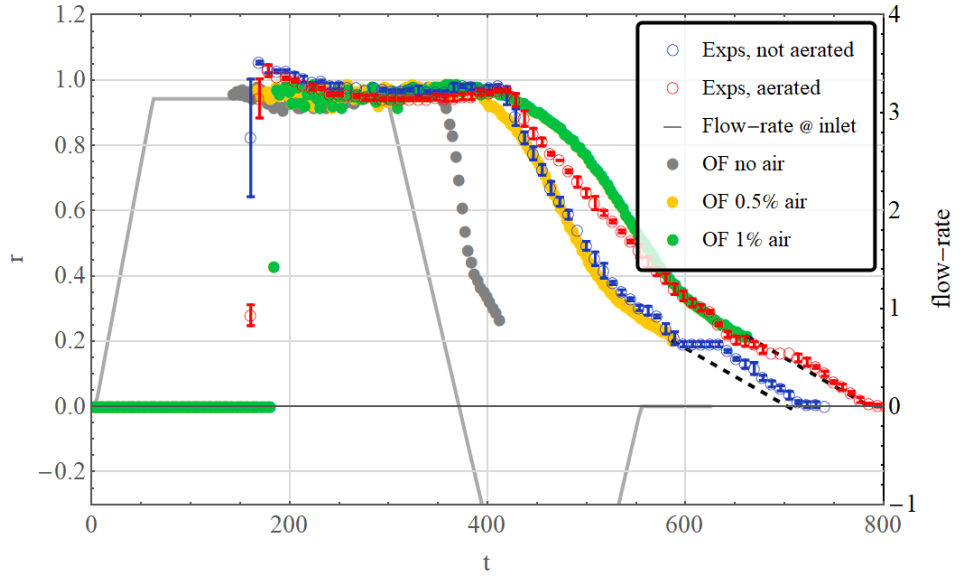

Figure 68: Results for mixture 3, Cam Profile 1. Solid, gray line represents the Cam Profile (referring to the flow-rate scale on the right); the dots represent the stream radius at a distance R from the nozzle: yellow dots for 0.5% disperse air in liquid, green for 1%, gray dots for pure liquid mixture, blue empty dots with error bars represent the experimental results of a not aerated mixture and red empty dots the experimental results of an aerated mixture. Black, dashed line represents the extrapolation according to Papageorgiou (1995).

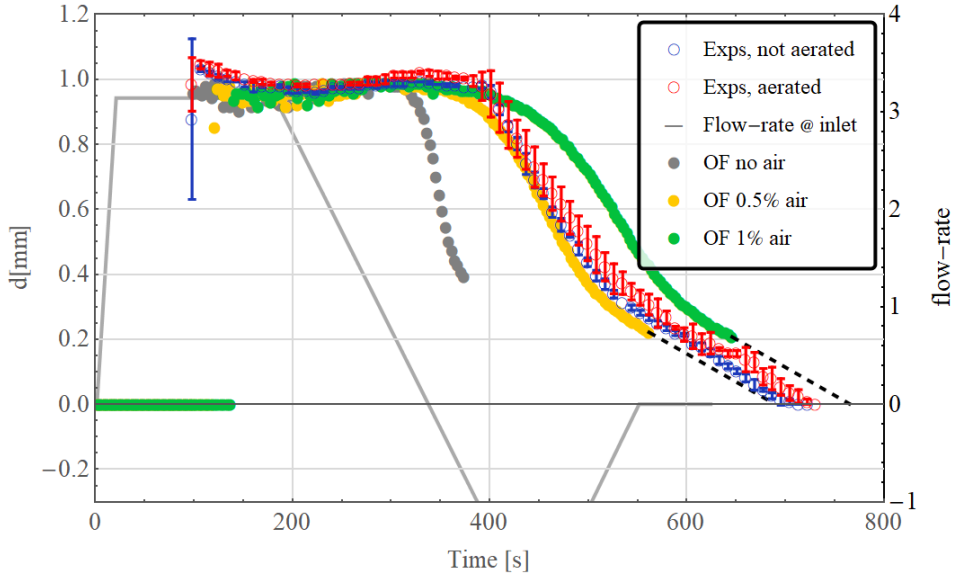

Figure 69: Results for mixture 3, Cam Profile 2. Solid, gray line represents the Cam Profile (referring to the flow-rate scale on the right); the dots represent the stream radius at a distance R from the nozzle: yellow dots for 0.5% disperse air in liquid, green for 1%, gray dots for pure liquid mixture, blue empty dots with error bars represent the experimental results of a not aerated mixture and red empty dots the experimental results of an aerated mixture. Black, dashed line represents the extrapolation according to Papageorgiou (1995).

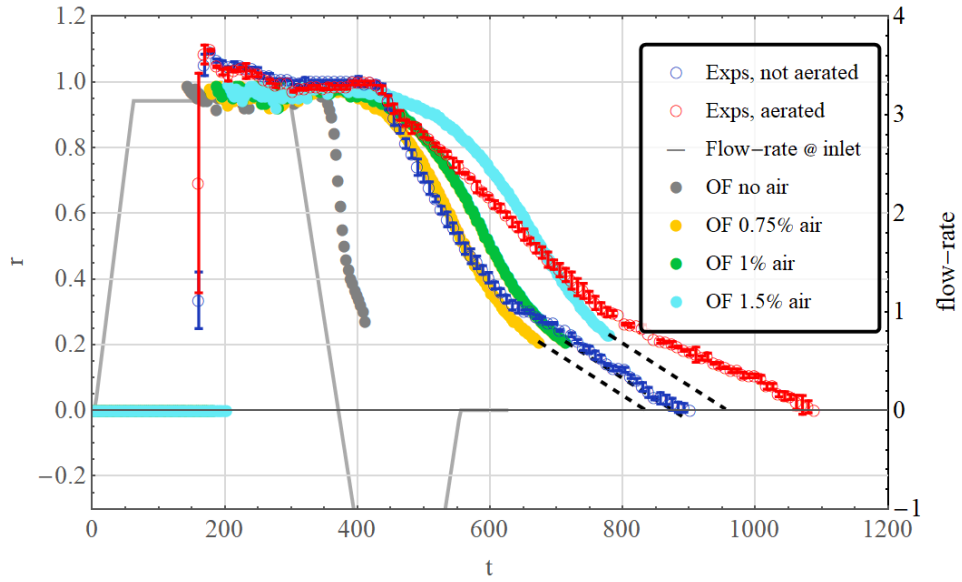

Figure 70: Results for mixture 4, Cam Profile 1. Solid, gray line represents the Cam Profile (referring to the flow-rate scale on the right); the dots represent the stream radius at a distance R from the nozzle: yellow dots for 0.75% disperse air in liquid, green for 1%, gray dots for pure liquid mixture, light blue dots for 1. 5% disperse air in liquid, blue dots with error bars represent the experimental results of a not aerated mixture and red dots the experimental results of an aerated mixture. Black, dashed line represents the extrapolation according to Papageorgiou (1995).

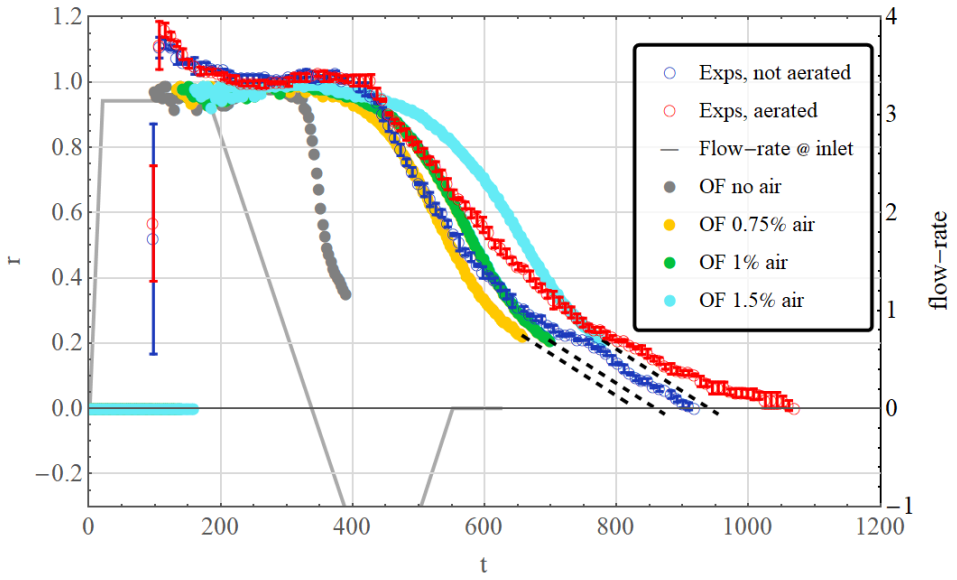

Figure 71: Results for mixture 4, Cam Profile 2. Solid, gray line represents the Cam Profile (referring to the flow-rate scale on the right); the dots represent the stream radius at a distance R from the nozzle: yellow dots for 0.5% disperse air in liquid, green for 1%, gray dots for pure liquid mixture, light blue dots for 1. 5% disperse air in liquid, blue dots with error bars represent the experimental results of a not aerated mixture and red dots the experimental results of an aerated mixture. Black, dashed line represents the extrapolation according to Papageorgiou (1995).

All the data shown in these figures highlight the five main phases characterizing the behavior of the liquid stream in a dosing operation:

1. piping flow: as discussed in section 6.3.1, at the beginning of a dosing cycle the liquid does not fill the pipeline entirely, and the first stage of the pushing phase is necessary for the liquid front to reach the nozzle exit (i.e., from $t = 0$ to $t = 100$ in Figure 71, where no liquid stream is observed after the nozzle);
2. formation of a jet: the liquid issuing into the ambient gas is unstable, and the stream radius can experience significant variations in the very first stages (i.e., from $t = 100$ to $t = 250$ in Figure 71, referring to experimental data);
3. stationary phase: once the liquid jet is formed and the flow rate has reached a constant value, the stream radius oscillates around a mean value (i.e., from $t = 250$ to $t = 450$ in Figure 71, referring to experimental data);
4. thinning phase: as the flow rate starts to decrease and attains a sufficiently low enough, the stream quickly thins (i.e., from $t = 450$ to $t = 700$ in Figure 71, referring to experimental data of not aerated sample);

5. pre-breakup phase: just before the breakup, the stream radius continues to decrease with a different slope as compared to the previous phase (i.e., from $t = 700$ to $t = 900$ in Figure 71, referring to experimental data of not aerated sample).

The instant when the liquid flow exits the nozzle (i.e., when a stream radius can be measured) depends on two factors: (i) the empty quota of the tube and (ii) the delay induced by the air entrapped in the liquid. The delay time induced by the former depends on cam profile and it can be easily estimated by means of a global mass balance as discussed in the previous section.

In general, the presence of air slows down the dosing dynamics, as clearly seen in both experiments and simulations. This is not the case, however, for mixture 1 (Figure 64 and Figure 65) where the experimental data show that different conditions of aeration do not significantly influence the dynamics. Density measurements (whose results are shown in Figure 51) show an absence of air for the not aerated sample (blue dot in Figure 51) and a value between 1% and 1.55% for the aerated sample measured right after the aeration (red dots in Figure 51) and a zero value if measured after the experiments (yellow dot in Figure 51). As for mixture 1, different conditions of aerations lead to the same behavior of the stream (as shown in Figure 66 and Figure 67). In the case of mixture 3, the higher viscosity is able to entrap the air added by aeration, whose effect is a delay of breakup dynamics, as visible from the evolution of stream radius shown Figure 68 and Figure 69. In particular, the two samples have the same behavior in the first part of the cycle (forming jet and stationary phase), but a different slope of the thinning phase. A similar scenario is also observed for mixture 4.

Experimental data are quantitatively predicted by simulations assuming an initial amount of air and the best correspondence in each case is confirmed both in the formation of the jet and in dynamics of thinning phase. For mixture 1, 5% and 1% air volume fraction give the best predictions for cam profile 1 and 2, respectively. For mixture 2, 0.5% volume fraction is the best value for both cam profiles. For mixture 3, numerical simulations predict very well the behavior of the not aerated sample under the hypotheses of 0.5% of disperse air (yellow curves in Figure 68 and Figure 69), with an excellent agreement during the thinning phase, whereas curve at 1% (green in Figure 68 and Figure 69) fits well the aerated stream radius for cam profile 1 and overestimate the dynamics for cam profile 2, as expected. The slight disagreement between numerical and experimental results for the aerated sample is supposed to be due to the heterogeneity of "real" liquid phase against the homogeneity assumption of the model. Simulations do not catch the results when $r < 0.2$, because of issues due to mesh resolution. In Figure 72, the last stage obtained with numerical simulations is shown, where the dark red area represents the liquid phase and the blue area the external air. Before breakup, a long thin filament is forming (viscous thread) that gets longer towards the nozzle because of sucking-back

phase. The smallest radius experienced by the filament is elsewhere with respect to fixed position where stream radius is detected (orange line in Figure 72), whose value is used in the corresponding graphs. However, when it reaches the same order of magnitude of mesh resolution (see Figure 73), the simulations diverge. The use of a finer mesh is not practicable because of increasing computational time due to a larger number of elements and to the smaller time step size required for temporal convergence. However, the evolution of the radius of a viscous filament has been derived by Papageorgiou (1995) and in dimensionless form is given by:

$$r = r_0 - 0.0709 * \frac{t}{Ca} \tag{6.9}$$

where $Ca = \eta U_c / \gamma$.

This linear law is reported by dashed black lines in Figure 68 and Figure 69 and perfectly fits the experimental data. Thus, it can be used to extrapolate the "missing" phase of numerical simulations on first approximation by assuming that the filament is a cylindrical shape and thins uniformly. The correctness of this approach will be discussed in the next section.

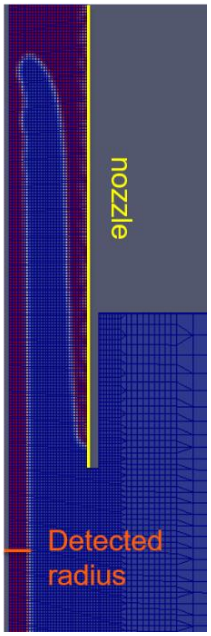

Figure 72: last frame obtained by numerical simulation: the yellow line represents the nozzle wall, the orange line the position where we measure the stream radius, the dark red area represents the liquid and the blue area the external gas phase. Dark blue lines represent the mesh.

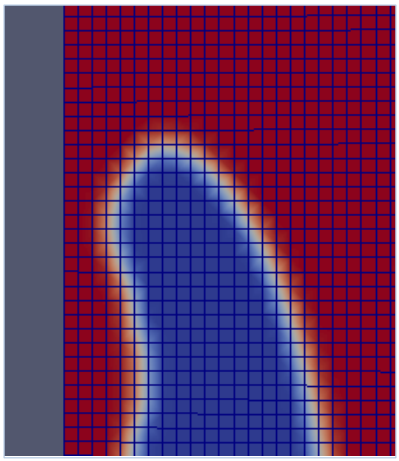

Figure 73: zoom of Figure 72 at the thinnest part of the filament: dark red area represents the liquid and the blue area the external gas phase; white line is the interface and dark blue lines represent the mesh.

6.4 Pre-breakup phase

When $Oh > 1$, simulations are not able to predict the pre-breakup dynamics, characterized by the formation of a long, thin filament, due to the extremely high resolution of the mesh required. Then, we extrapolate the evolution of the stream radius by resorting on the asymptotic law derived by Papageorgiou (1995) under the hypothesis of negligible inertial forces. This theoretical law describes how the pinching is approached under the action of capillary forces, whose evolution is represented in Figure 13. Since breakup is a local phenomenon, it must be pointed out that Eq. 6.9 is referred to the radius of the neck, corresponding to the minimum radius experienced by the filament, which, in this regime, is placed midway from the liquid still attached to the nozzle and the liquid drained to the forming drop.

In the case of sucking-back velocity, the typical symmetric geometry shown in section 2.5 fails: Figure 74 shows the time evolution of interfaces for the Mixture 4 (air 0.75%, cam profile 1), opportunely labelled with dimensionless times, obtained by numerical simulations. The grey horizontal line represents the nozzle exit and the dark red horizontal line represents the fixed position where we measure the radius to be compared with the experimental one. On the axis, the axial position (y-axis) and the radius (x-axis) are represented. The flow is directed downwards during the pushing phase and upwards during the sucking back phase. The phenomenology shown in Figure 74 is conceptually different from the behavior we know from literature, which occurs in the case of a low, stationary feeding-flow, where a minimum radius can be clearly identified.

In our case, thinning starts from a condition of continuous jet, whose radius decreases getting far from the nozzle because of gravitational acceleration. Since the liquid phase has been modelled as compressible, in order to analyze the behavior of the stream radius, we need to refer to the flow rate experienced in a region close to the nozzle. The light blue line in Figure 75 represents the flow rate before the nozzle block ($z = 0.16$ in the geometry represented in Figure 46), to be read on the right *y*-axis, that progressively deviates from the flow-rate imposed by the pump (grey line in Figure 75) as the sucking back phase is approached. In the same graph, we represent with yellow dots the stream radius of the liquid jet at a fixed position and with green dots the minimum radius obtained by numerical simulations with 0.75% of disperse air. The minimum radius of stationary phase is found to be at the bottom of our geometry, and starts to decreases as soon as the flow rate decreases as well. At the same time, the radius near the nozzle does not significantly change. At the beginning, thinning is a phenomenon occurring far from the nozzle and the minimum radius position slowly rises the liquid stream. When the flow-rate is almost zero, thinning starts to affect the entire liquid stream, and

stream radius starts to decreases in time although we need to wait the onset of the sucking-back phase to observe a local thinning and to identify a minimum radius that is independent of the geometry we are considering. At $t = 600$, the minimum radius "crosses" the fixed position and moves in the same direction of the flow (black circles in Figure 74). In these stages, the minimum radius experiences a *faster* dynamics with respect to the one reported in the literature, suggesting that the breakup is going to occur *inside the nozzle*, against the behavior observed in experiments, shown with the sequence of frames in Figure 76.

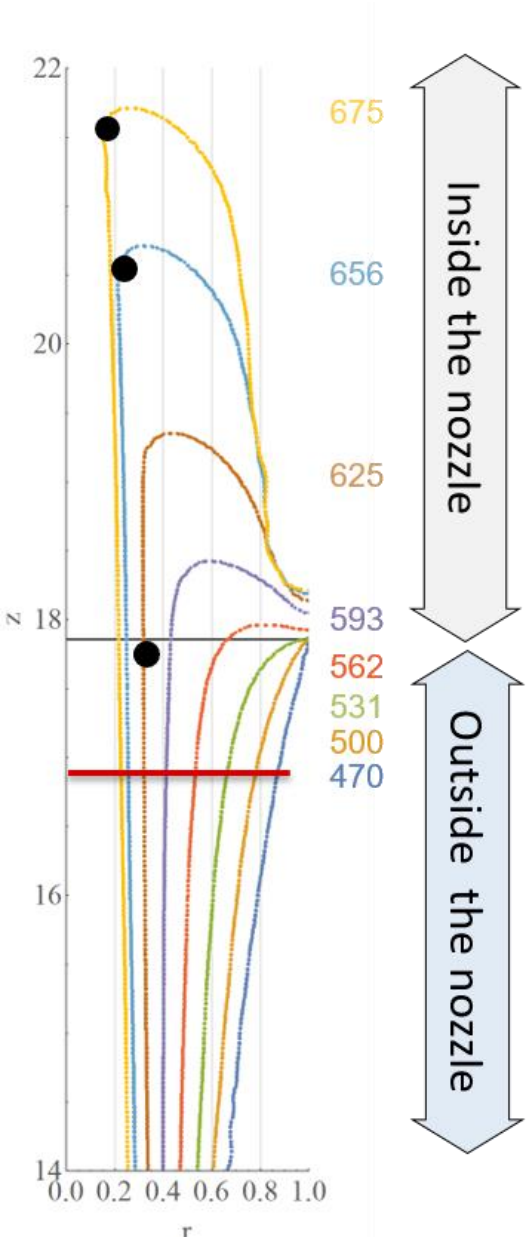

Figure 74: Temporal evolution of interfaces, represented for different slopes for mixture 4. x-axis represents the, y-axis the vertical quota. Nozzle exit is placed at $z = 17.86$ and is represented by a horizontal grey line. The horizontal red line represents the position where we measure the radius in simulations and experiments. Each color represents a different value of dimensionless time (labelled).

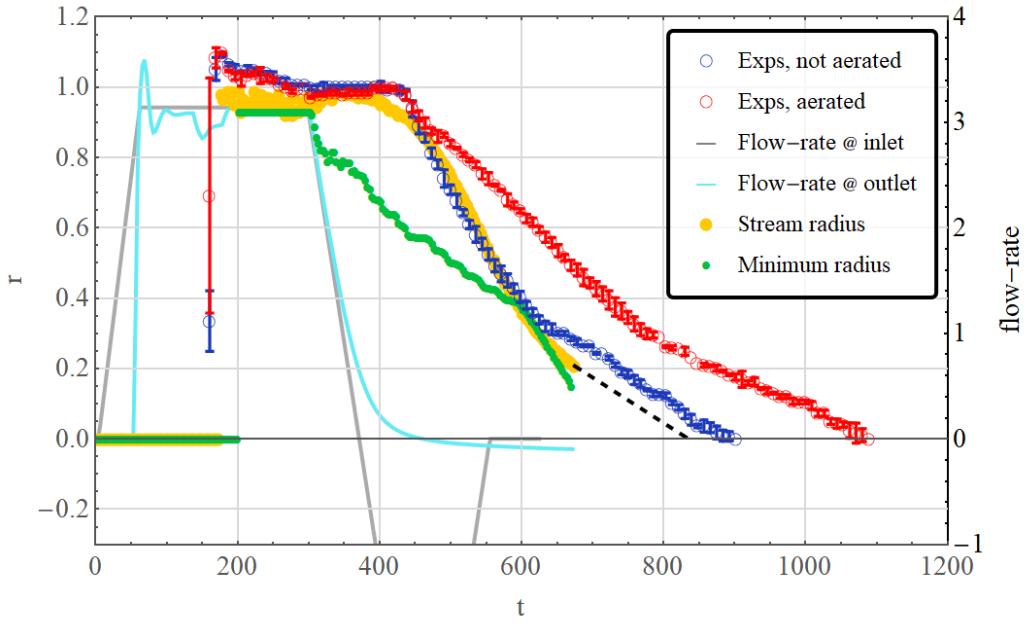

Figure 75: Results for mixture 4, Cam Profile 1. Blue dots with error bars represent the experimental results of a not aerated mixture; red dots the experimental results of an aerated mixture, measured at a distance R under the nozzle exit. Solid lines refer to right axis: gray line represents the Cam Profile imposed at inlet, light blue line the flow-rate experienced at $z = 0.16$. Yellow and green dots represent the radius at a distance R under the nozzle exit and the minimum radius, respectively, calculated by numerical simulations with 0.75% of air dispersed in liquid phase. Black, dashed line represents the extrapolation according to Papageorgiou (1995).

Actually, simulations are based on the assumption of axial symmetry, while Figure 76 shows that, when the string is thin enough, the situation is no longer axisymmetric and liquid impacts on a wall of the nozzle, trickling down. Although the transparency, we cannot know if a breakup phenomenon has occurred inside the nozzle. Moreover, the liquid at the wall does not experience the imposed sucking-back, since its velocity is around zero, and that agrees with the inertialess assumptions of the theoretical derivation. Notice that the impact on the wall occurs when the thinning phase changes its slope ($t = 640$ in Figure 75).

In conclusion, the behavior found experimentally belongs to two different problems: in the first stage, the liquid undergoes a sucking-back velocity and is recalled inside the nozzle moving upwards; in the second stage it impacts on the wall and thins as a viscous thread. Of course, simulations under axial symmetric hypotheses can only predict the first stage.

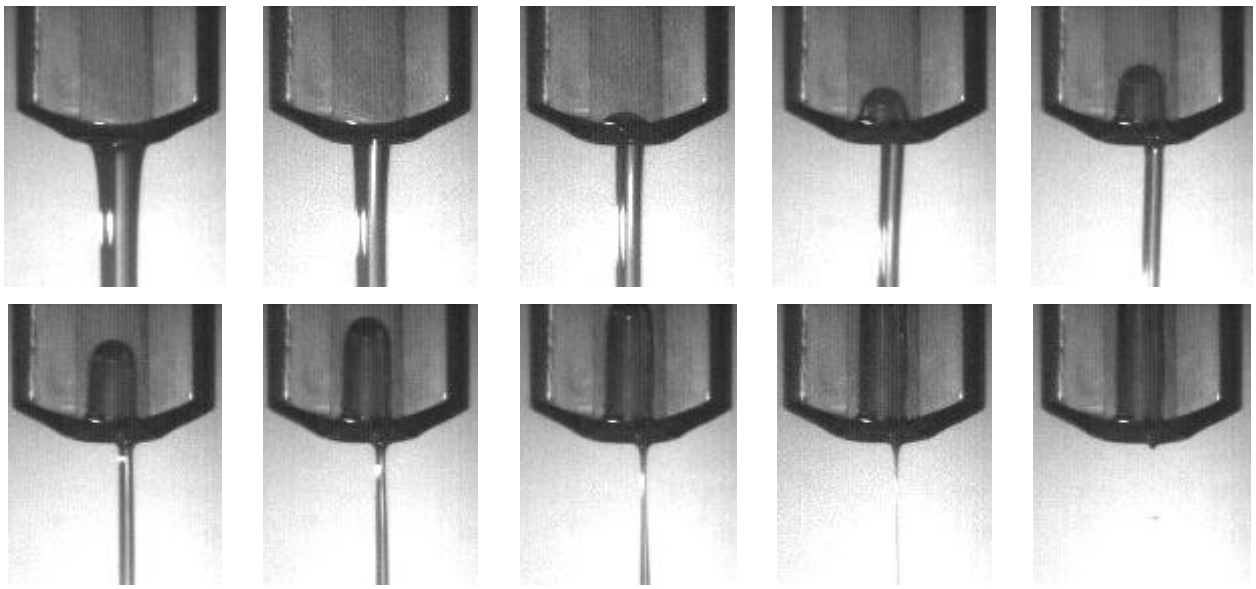

Figure 76: Sequence of frames of breakup phase, zoom on nozzle exit (mixture 4, cam profile 1, not aerated sample, 70 fps). Time moves forward from left to right, and from first row to second raw.

6.5 Dosing time

The primary objective of an industrial dosing process is to minimize the time needed to perform a complete cycle, once an effective breakup is achieved. To this end, different liquids and inlet conditions must be explored and for each different combination we can refer to a global quantity, the *dosing time*, that is the time from the beginning of the pushing phase to the observed breakup.

On the other side, the aim of numerical simulations is to accurately predict the dynamics of a system under given conditions. Figure 77 represents a comparison between experimental and numerical results in terms of dosing time, obtained for the four different mixtures and the two different cam profiles, in the case where air has been not intentionally added. Since numerical results strongly depend on the volume fraction of dispersed air in the liquid phase, we choose for this comparison the best predictions of experimental data. Except for Mixture 1, for which we have observed a peculiar phenomenology, the same amount of air gives the best prediction for both the cam profiles considered, suggesting that this value might be a characteristic of the system. Under this assumption, the excellent agreement shown in Figure 77 conveys that the model used in numerical simulations can be effectively used for the investigated problem.

The graph also shows a noticeable relation between dosing time and Oh and a quasi-independency on sucking-back slope, with a slight preference of cam profile 2.

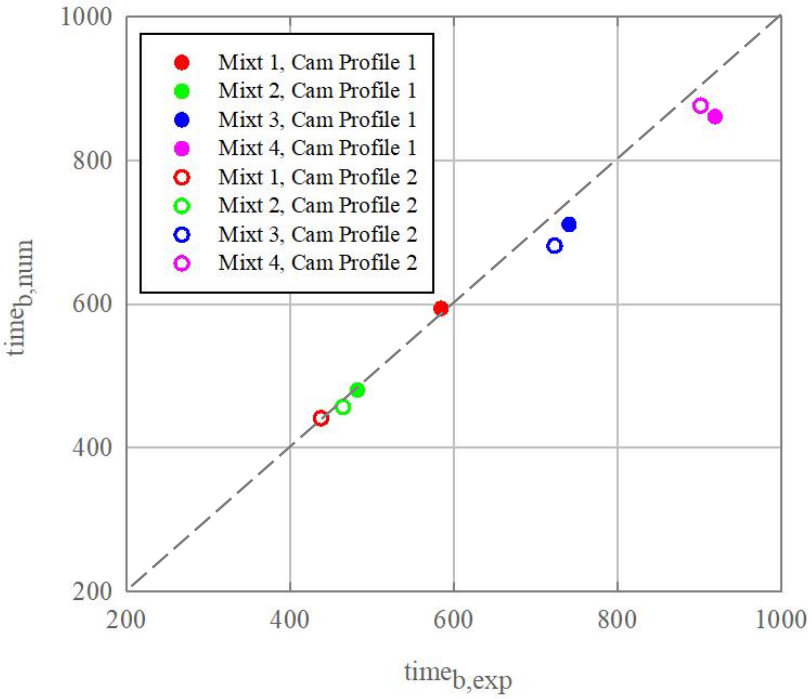

Figure 77: Numerical dosing time versus experimental dosing time for the 8 analyzed cases. Different colors represent different mixtures: red dots for mixture 1, green dots for mixture 2, blue dots for mixture 3 and pink dots for mixture 4; full circles are referred to Cam Profile 1, empty circles are referred to Cam Profile 2.

6.6 Effect of air bags and pipe flexibility

In this section, we want to show the effect of air bags in a liquid system used for dosing purposes as well as the importance of pipe flexibility.

The formation of air bags occurs when the apparatus has not been flushed properly (i.e., with a low flow rate), and the smallest bubbles present the system coalesce, forming larger bags as shown in Figure 78 that persist in the system. In these experiments, we use Mixture 1 as liquid, while in numerical simulations the assumption of homogenous compressible liquid is still used, although not representing the real case.

Experimental results (blue empty dots with error bars represented in Figure 79) show an increasing of 15% of the dosing time required with respect to the results shown in Figure 64. The numerical simulations are shown in Figure 79 as closed circles and refer to the left *y*-axis, while the grey solid line represents the flow-rate applied by the pump and refers to right *y*-axis. Different colors of closed circles correspond to different volume fractions of dissolved air, and the dynamics is well predicted hypothesizing an equivalent amount of disperse air of 12%.

Figure 78: air bags in feeding flexible pipe.

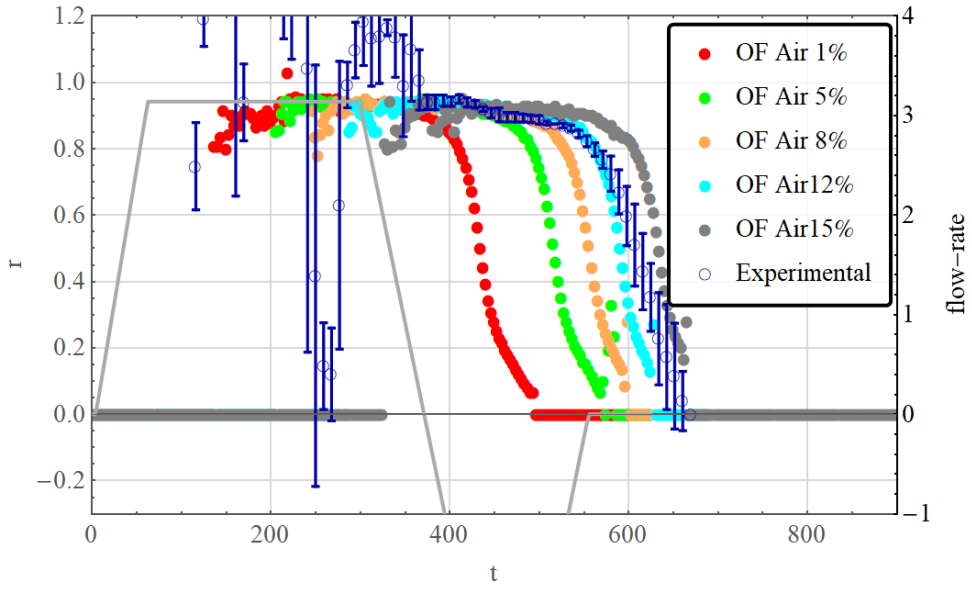

Figure 79: Results for mixture 4, Cam Profile 2. Solid, gray line represents the Cam Profile (referring to the flow-rate scale on the right); the dots represent the stream radius at a distance R from the nozzle: red dots for 1% disperse air in liquid, green for 5%, orange for 8%, light blue dots for 12% and gray dots for 15% of disperse air, blue dots with error bars represent the experimental results of a not aerated mixture containing air bags.

All the simulations presented so far have been run by assuming that the feeding tube is rigid. However, the system used in experiments and described in section 6.1, is composed of a 1.7 m semi-flexible pipe, whose effects are analyzed in this section. The literature about hydraulic transient in pipelines has been reviewed by Ghidaoui (2005), dealing with rigidly anchored pipe, and by Tjisseling (1996), primarily addressed on the effects of pipe motion and inertia. Korteweg (1878) extended the sound velocity to account for tube flexibility:

$$\frac{1}{c_f^2} = \frac{1}{c_0^2} + \frac{1}{c_1^2} \tag{6.10}$$

where c_f is the resulting sound velocity taking into account the contribution of compressible fluid, c_0, and of elastic tube, c_1. Regarding c_0, we use Eq. 2.9 shown in section 2.8, and c_1 is calculated according to classical waterhammer theory (Gibson, 1908):

$$c_1 = \sqrt{\frac{1}{\psi}\frac{E}{\rho_f}\frac{e}{D}} \tag{6.11}$$

where D is the pipe diameter, e the pipe wall thickness, E the Young's modulus for elasticity, ρ_f the fluid density and ψ a pipe support factor, that has been estimated as (Wylie, 1993):

$$\psi = \frac{2e}{D}(1+\nu) + \frac{D}{D+e}\left(1-\frac{\nu}{2}\right) \tag{6.12}$$

where ν is the Poisson's ratio of pipe material.

Rather than modeling a flexible pipe, its contribution on the dynamics of the system has been embedded in liquid phase, and the resulting c_f used in Eq. 12 (section 4.1). Its effects have been evaluated for the "extreme" liquids (equivalent to Mixture 1 and Mixture 4) and in case of low amount of dispersed air. In the calculations, we use $D = 6mm$, $e = 1\,mm$, $\nu = 0.4$ and $E = 2.5\,GPa$. Mixture 1 and Mixture 4 used in these simulations slightly differ from those presented in section 6.1, so we will refer to Mixture 1b ($Oh = 0.1$) and Mixture 4b ($Oh = 3.3$).

Figure 80 and Figure 81 represent the results of numerical simulations of the system described above, with the aim to compare the effect of a flexible pipe. In Figure 80 the stream radius of Mixture 1b with 1% w/w air dispersed is shown in time, and values obtained modelling the elasticity of the pipe (red dots) overlap those with the rigid pipe assumption (blue dots). In Figure 81, the corresponding values for Mixture 4b with 0.5% air dispersed are shown. In this case, a small deviation is visible, but negligible if compared with the effect that few traces of air can have on the final dynamics.

In our system, then, the approximation of rigid pipe is realistic as the effect of flexibility would be minor if one considers the uncertainty due to the presence of air under homogeneous hypothesis.

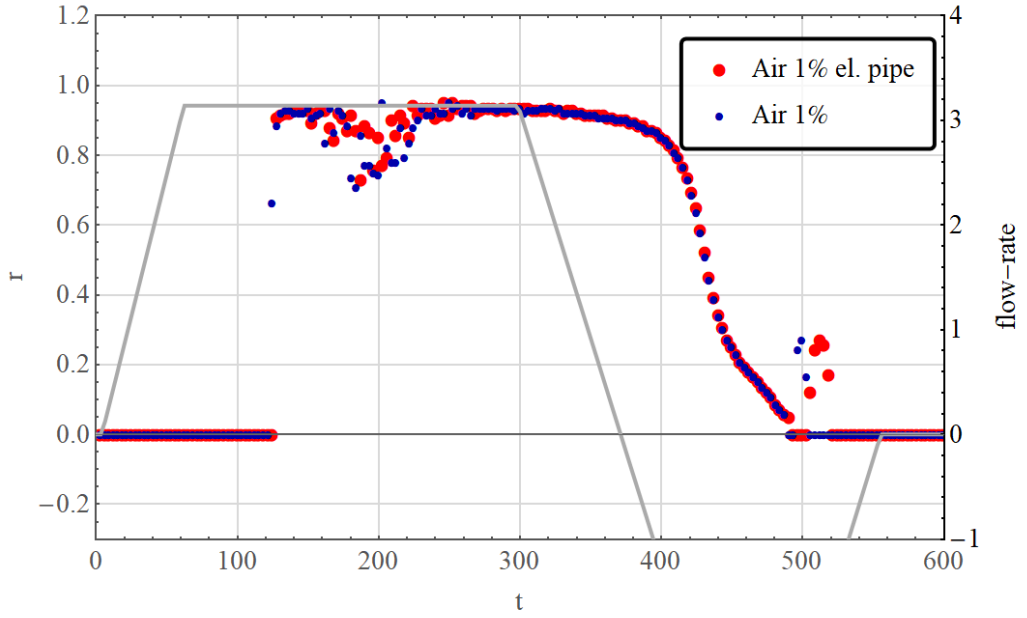

Figure 80: Results for mixture 1b, Cam Profile 1. Solid, gray line represents the Cam Profile (referring to the flow-rate scale on the right); the dots represent the stream radius obtained with numerical simulations at a distance R from the nozzle: red dots for a system with 1% disperse air in liquid and a flexible pipe, red dots for a system with 1% w/w disperse air in liquid and a rigid pipe.

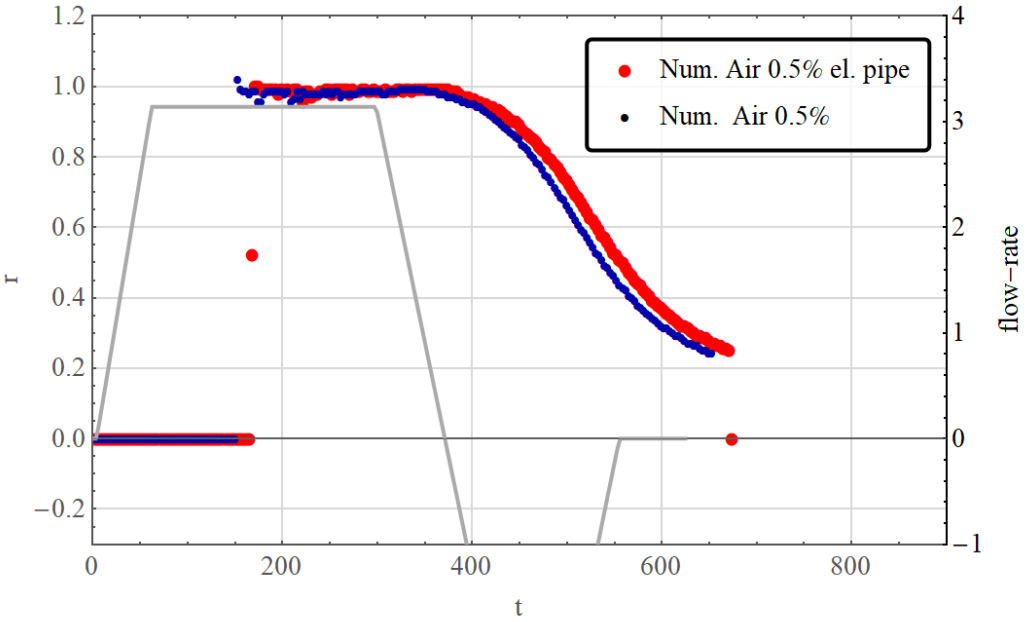

Figure 81: Results for mixture 4b, Cam Profile 1. Solid, gray line represents the Cam Profile (referring to the flow-rate scale on the right); the dots represent the stream radius obtained with numerical simulations at a distance R from the nozzle: red dots for a system with 1% w/w disperse air in liquid and a flexible pipe, red dots for a system with 1% disperse air in liquid and a rigid pipe.

6.7 Concluding remarks

In this Chapter, the behavior of a liquid stream processed in a real dosing equipment has been analyzed by experiments and numerical simulations. We tested the behavior of different liquids undergoing to time-varying inlet conditions, in order to find the conditions to properly perform the process (formation of a stable jet, effective breakup) and to minimize the dosing times.

The major role in such a process is played by compressibility induced by the coexistence of a gaseous (air) and a liquid phase. The effect of the air is to dampen the transmission of inlet condition throughout the pipeline that connects the pump to the nozzle, in particular delaying the sucking back phase. In modelling, air is accounted for by considering a homogenous phase. We have demonstrated, both with experiments and with numerical simulations, that the more is the air dissolved in the liquid, the longer is the dosing, and that the absorption/desorption/entrapment of air is a peculiar characteristic of the process, characterized by cycles of pushing (high pressures) and sucking-back phases (under ambient pressures). In fact, a pure liquid behavior has never been observed.

Once the right amount of disperse air in the liquid has been found, the numerical predictions are in excellent agreement with experimental results, both for the jet phase and for the thinning phase. Regarding high-*Oh* liquids, pre-breakup phase cannot be simulated because of the formation of a too thin filament, whose radial dimension is of the same order of magnitude of the mesh. Literature results on the time evolution of the thinning dynamics in the viscous regime are, instead, used.

A strong assumption used in simulated system is the axisymmetric geometry. We found that this hypothesis has no effect on the low-*Oh* liquids (thinning and breakup dynamics is well predicted), while the behavior of high-*Oh* liquids deviates from axisymmetric dynamics when a thin filament is formed, going to impact on a wall of the nozzle. This displacement promotes the stringing phenomenon that further delays the final breakup and is, then, undesired. Generally, dosing time increases as *Oh* increases. Although viscous forces are expected to prevent breakup, their effect should become relevant only in the last stage of thinning phases: the more is the viscosity, the faster the fluid reacts to the velocity variations experienced when the flow rate starts to decrease. This is confirmed by running simulations for pure liquid, where a smaller geometry composed of the only nozzle and external air is considered (not shown), that unexpectedly predict a slight slower dynamics for low-*Oh* liquids.

The higher dosing times found for high-*Oh* liquids, where the presence of air is of the same order of magnitude than low-*Oh* liquids, have an explanation in the model we used. The liquid phase has been

modeled by redefining its density that does not vary linearly with pressure. The higher is *Oh*, the higher are viscous forces, the higher are pressures required to set in motion the fluid at the desired flow rate. High-*Oh* liquids experience a wider range of pressures (both in pushing phase and in sucking back) and, consequently of densities, slowing down the final response of the liquid.

All these considerations seem to suggest to prefer liquids where viscous forces are as low as possible when compressibility effects are important. However, although low-*Oh* liquids exhibit faster dynamics in dosing cycles, they experience some unwanted phenomena, such as primary breakup before forming a stable jet and dripping (both right before the beginning of a cycle and right after the end of the cycle). As seen, very low-*Oh* liquids tend to take in air in form of millimetric bubbles near the nozzle during the breakup phase. When the liquid is pushed again in the following cycle, the air exits together with the liquid determining an instability of the jet. Moreover, being a low-*Oh* liquid more unstable, the secondary wave produced by breakup causes the formation of satellite drops, whose motion after pinching do not necessarily follow the linear trajectory of the jet and can cause fouling phenomena. As *Oh* increases, the dimension of satellite drops gets smaller. Undesired phenomena typical of low-*Oh* liquids in dosing processes are related to splashing (when the liquid exits the cavity it should fill due to the impact with its bottom) and to sloshing (when liquid comes out the cavity during the swap of the filled cavity with an empty one).

7. Conclusions

In this thesis, the behavior of a Newtonian fluid exiting a nozzle has been studied. The overview on the state-of-art has highlighted the availability of numerous works focused on free-surface flows limited, however, to continuous feeding flow conditions. In dosing operations, it is primarily important to induce a breakup of a liquid stream by employing time-varying feeding flow rates.

The work has been carried out both by means of numerical simulations, by employing the Volume of Fluid, and experiments. First, we study the fluid dynamics of a class of incompressible Newtonian liquids subjected to inlet conditions varying linearly in time and characterized by an inversion of the direction of the motion. In the investigated cases, we found that the imposed velocity profile has a strong influence on the initial thinning dynamics. However, the last stages before breakup are characterized by a local dynamics: the motion is not more dependent on the external parameters and is well-described by scaling-laws derived from steady-state conditions.

Then, we move on a real dosing system and we found that the main characteristic is the presence of entrapped air in the liquid phase that delays the onset of the thinning phase leading to breakup and slows down the thinning dynamics. As a consequence, the time required to perform a complete dosing cycle increases, proportionally both to the amount of entrapped air and to the viscous forces acting in the liquid system.

We propose a new method to deal with the compressible liquid phase modeled as a homogeneous material. The dynamics of liquids characterized by different properties has been studied in order to test and validate the numerical code in a large variety of real systems, and to investigate their suitability in dosing processes in terms of stability of the jet and effective breakup. We find that

dosing time is proportional to *Oh* number, and high-*Oh* liquids exhibit the formation of a thin, persistent filament before to enter the breakup phase. On the other hand, low-*Oh* liquids are affected by undesired low-frequencies instabilities both in the first stage of formation of the jet (unstable jet), and in the post breakup phase (satellite droplets).

Comparisons between numerical and experimental results are in excellent agreement, once the entrapped air in the system is known: the correlation between liquid physical properties and disperse air must be investigated for a totally predictive tool.

Simulations are affected by two strong limitations:

1. the finest achievable mesh for the volume considered cannot adequately describe the final stages of thinning in the case of high-*Oh* liquids;
2. axisymmetric assumption used in simulations is no longer valid in pre-breakup phase observed in experiments: the motion of the liquid stream, as soon as it impacts on a wall of the nozzle, becomes independent of sucking back velocity because of the no-slip condition. The consequence is a further slowdown of the dynamics in pre-breakup phase, since the liquid that enters the "local" regimes before than suggested by simulations. This effect is stronger for high-*Oh* liquids.

Fortunately, as the linear law derived for a viscous fluid perfectly predicts the final dynamics towards breakup found in the experiments, it can be used to extrapolate the missing data. This expedient can be employed for estimating the final dosing time without an excessive computational effort. Of course, three-dimensional simulations could provide more insights on this aspect, induced in real dosing processes by a 90° elbow connecting the feeding pipe with the nozzle. In such a case, the effect of the length of the nozzle on the final breakup should be explored.

Future work will also include the study of the dynamics of shear thinning fluids, that are mostly used in industrial applications.

Appendix A: myCompressibleSolver

In this Chapter, the code used to build the customized solver is presented. Notice that we refer to OpenFOAM 2.1.1, used in this work. The customized solver derives from an OpenFOAM standard solver, `compressibleInterFoam`, that deals with 2 compressible, immiscible fluids, whose densities are modeled as linearly dependent on pressure with the law:

$$\rho(p) = \rho_0 + \frac{1}{c^2}\, p \tag{A.1}$$

where c is the sound velocity and ρ_0 the density at a reference pressure. They must be defined for each phase: the pure liquid phase and the "external" air. However, we need to model the liquid phase as a homogenous biphasic fluid, where traces of air are dissolved in the liquid phase, for which we find a dependence of density on pressure far to be linear. It has been presented in section 6.2.1 and is here reported:

$$\rho_1(p) = \rho_{1,0} + a\, p + \frac{b}{p} \tag{A.2}$$

where a and b are constants obtained from the approximate solution of differential equation 6.3 with boundary condition 6.7 presented in section 6.2.1, and the subscript 1 means "liquid phase", here referring as homogeneous mixture.

As anticipated in the body of the thesis, a second issue has required a modification of the standard solver, related to the gravity field. As discussed in section 6.2.2, we choose to simulate the entire dosing system by neglecting the 90° round elbow that connects a quasi-horizontal long pipe with the vertical nozzle block, with the aim to reduce the computational effort by means of an axisymmetric geometry. In order to consider the gravity force acting only in that portion of the domain representing the nozzle and the "ambient air", we define a "like-gravity" volume field, not uniform in space. In particular, we define a critical quota z_c, so:

$g = -9.81\ m/s^2$ when $z < z_c$

$g =$ $0\ m/s^2$ when $z > z_c$.

A.1 Standard compressibleInterFoam

A.1.1 Balance Equations

In section 4.3 the model equations have been presented. In this section, we rearrange the equations in the form that will be solved by the numerical code.

The mass balance expressed for phase 1 is:

$$\frac{\partial}{\partial t}(\alpha\rho_1) + \boldsymbol{\nabla}\cdot\alpha\rho_1\boldsymbol{v} = 0 \qquad \text{(A.3)},$$

that expanded becomes:

$$\alpha(\dot{\rho_1} + \boldsymbol{v}\cdot\boldsymbol{\nabla}\rho) + \alpha\rho_1\boldsymbol{\nabla}\cdot\boldsymbol{v} + \rho_1(\dot{\alpha} + \boldsymbol{v}\cdot\boldsymbol{\nabla}\alpha) = 0 \qquad \text{(A.4)}.$$

where by applying the chain rule to the derivative of density, remembering that $\rho_1 = \rho_1(p)$ we can rearrange as:

$$(\dot{\alpha} + \boldsymbol{v}\cdot\boldsymbol{\nabla}\alpha) = -\frac{\alpha}{\rho_1}\frac{\partial\rho_1}{\partial p}(\dot{p} + \boldsymbol{v}\cdot\boldsymbol{\nabla}p) - \alpha\boldsymbol{\nabla}\cdot\boldsymbol{v} \qquad \text{(A.5)}.$$

Equation A.5, summed for both phases, becomes:

$$\left(\frac{\alpha}{\rho_1}\frac{\partial\rho_1}{\partial p} + \frac{(1-\alpha)}{\rho_2}\frac{\partial\rho_2}{\partial p}\right)(\dot{p} + \boldsymbol{v}\cdot\boldsymbol{\nabla}p) + \boldsymbol{\nabla}\cdot\boldsymbol{v} = 0 \qquad \text{(A.6)}.$$

The final form of our volume fraction equation A.5 is derived by using A.6 to replace the term on the right side:

$$\dot{\alpha} + \boldsymbol{\nabla}\cdot\alpha\boldsymbol{v} - \alpha\boldsymbol{\nabla}\cdot\boldsymbol{v} = \alpha(1-\alpha)\left(\frac{\rho_{1,p}\rho_2 - \rho_{2,p}\rho_1}{\alpha\rho_{1,p}\rho_2 + (1-\alpha)\rho_{2,p}\rho_1}\right)\boldsymbol{\nabla}\cdot\boldsymbol{v} \qquad \text{(A.7)}.$$

where $\rho_{k,p} = \partial\rho_k/\partial p$ with $k = \{1,2\}$.

Equations 4.3, 4.4 and A.7 are then discretized and used to obtain $\alpha, \boldsymbol{v}$ and p_d, while ρ_1 and ρ_2 are obtained by means of 4.7 and 4.8. Discretization schemes used in this work are reported in the file fvSchemes in Appendix B.

A.1.2 The solver case

The compressibleInterFoam directory is composed of:

1. compressibleInterFoam.C: is the main file and contains of a set of instructions. It can be compiled independently of the other code to create an executable. It recalls other *files*.H;
2. Make directory: it contains the instructions for the compilation, and specifies which libraries and applications are used in compressibleInterFoam.C;
3. *files*.H: are independent pieces of code.

With respect to the standard version of the solver, the modified files are:

- newCompressibleInterFoam.C: calculates and uploads each time-step the new equation of state;
- createFields.H: reads constants and initial conditions defined in the case folder (file `transportProperties`, reported in Appendix B) and creates the fields that will be used by other files;
- pEqn.H: solves the equation for pressure.

Their new version is reported in the following.

A.1.2.1 newCompressibleInterFoam.C

```
/*---------------------------------------------------------------------------*\
  =========                 |
  \\      /  F ield         | OpenFOAM: The Open Source CFD Toolbox
   \\    /   O peration     |
    \\  /    A nd           | Copyright (C) 2011 OpenFOAM Foundation
     \\/     M anipulation  |
-------------------------------------------------------------------------------
License
    This file is part of OpenFOAM.

    OpenFOAM is free software: you can redistribute it and/or modify it under the
terms of the GNU General Public License as published by the Free Software
Foundation, either version 3 of the License, or(at your option) any later version.

    OpenFOAM is distributed in the hope that it will be useful, but WITHOUT ANY
WARRANTY; without even the implied warranty of MERCHANTABILITY or FITNESS FOR A
PARTICULAR PURPOSE.  See the GNU General Public License for more details.

    You should have received a copy of the GNU General Public License
    along with OpenFOAM. If not, see <http://www.gnu.org/licenses/>.

Application
    myCompressibleInterFoam
```

```
Description
    Solver for 2 compressible, isothermal immiscible fluids using a VOF(volume of
fluid) phase-fraction based interface capturing approach.

    The momentum and other fluid properties are of the "mixture" and a single
momentum equation is solved.

    Turbulence modelling is generic, i.e.  laminar, RAS or LES may be selected.

\*---------------------------------------------------------------------------*/

#include "fvCFD.H"
#include "MULES.H"
#include "subCycle.H"
#include "interfaceProperties.H"
#include "twoPhaseMixture.H"
#include "turbulenceModel.H"
#include "pimpleControl.H"

// * * * * * * * * * * * * * * * * * * * * * * * * * * * * * * * * * * * * * //

int main(int argc, char *argv[])
{
    #include "setRootCase.H"
    #include "createTime.H"
    #include "createMesh.H"
    #include "readGravitationalAcceleration.H"
    pimpleControl pimple(mesh);

    #include "readControls.H"
    #include "initContinuityErrs.H"
    #include "createFields.H"
    #include "CourantNo.H"
    #include "setInitialDeltaT.H"

    // * * * * * * * * * * * * * * * * * * * * * * * * * * * * * * * * * * * * //

    Info<< "\nStarting time loop\n" << endl;

    while (runTime.run())
    {
        #include "readControls.H"
        #include "CourantNo.H"
        #include "setDeltaT.H"

        runTime++;

        Info<< "Time = " << runTime.timeName() << nl << endl;

        // --- Pressure-velocity PIMPLE corrector loop
        while (pimple.loop())
        {
            #include "alphaEqnsSubCycle.H"

            solve(fvm::ddt(rho) + fvc::div(rhoPhi));

            #include "UEqn.H"

            // --- Pressure corrector loop
            while (pimple.correct())
            {
                #include "pEqn.H"
```

```
            }

            if (pimple.turbCorr())
            {
                turbulence->correct();
            }
        }
        psi1 =  -b1/pow(p_rgh,2)+a1;

        rho = alpha1*rho1 + alpha2*rho2;

        runTime.write();

        Info<< "ExecutionTime = "
            << runTime.elapsedCpuTime()
            << " s\n\n" << endl;
    }

    Info<< "End\n" << endl;

    return 0;
}


// ************************************************************************* //
```

A.1.2.2 createFields.H

```
Info<< "Reading field p_rgh\n" << endl;
    volScalarField p_rgh
    (
        IOobject
        (
            "p_rgh",
            runTime.timeName(),
            mesh,
            IOobject::MUST_READ,
            IOobject::AUTO_WRITE
        ),
        mesh
    );

    Info<< "Reading field alpha1\n" << endl;
    volScalarField alpha1
    (
        IOobject
        (
            "alpha1",
            runTime.timeName(),
            mesh,
            IOobject::MUST_READ,
            IOobject::AUTO_WRITE
        ),
        mesh
    );

    Info<< "Calculating field alpha1\n" << endl;
    volScalarField alpha2("alpha2", scalar(1) - alpha1);

    Info<< "Reading field U\n" << endl;
    volVectorField U
    (
```

```
        IOobject
        (
            "U",
            runTime.timeName(),
            mesh,
            IOobject::MUST_READ,
            IOobject::AUTO_WRITE
        ),
        mesh
    );

    #include "createPhi.H"

    Info<< "Reading transportProperties\n" << endl;
  twoPhaseMixture twoPhaseProperties(U, phi);

    dimensionedScalar rho10
    (
        twoPhaseProperties.subDict
        (
            twoPhaseProperties.phase1Name()
        ).lookup("rho0")
    );

    dimensionedScalar rho20
    (
        twoPhaseProperties.subDict
        (
            twoPhaseProperties.phase2Name()
        ).lookup("rho0")
    );

    dimensionedScalar a1
    (
        twoPhaseProperties.subDict
        (
            twoPhaseProperties.phase1Name()
        ).lookup("a")
    );

    dimensionedScalar psi2
    (
        twoPhaseProperties.subDict
        (
            twoPhaseProperties.phase2Name()
        ).lookup("psi")
    );
    dimensionedScalar b1
    (
        twoPhaseProperties.subDict
        (
            twoPhaseProperties.phase1Name()
        ).lookup("b")
    );

    dimensionedScalar pMin(twoPhaseProperties.lookup("pMin"));
      volVectorField gfield
(
        IOobject
        (
            "gfield",
            runTime.timeName(),
            mesh,
```

```
        IOobject::MUST_READ,
        IOobject::NO_WRITE
    ),
 mesh
);

 volScalarField gh("gh", gfield & mesh.C());
 surfaceVectorField g1("g1",linearInterpolate(gfield));
 surfaceScalarField ghf("ghf", g1 & mesh.Cf());

  volScalarField psi1
(
     IOobject
    (
         "psi1",
        runTime.timeName(),
        mesh,
        IOobject::READ_IF_PRESENT,
        IOobject::AUTO_WRITE
    ),
  -b1/pow(p_rgh,2)+a1
);

volScalarField p
(
    IOobject
    (
        "p",
        runTime.timeName(),
        mesh,
        IOobject::NO_READ,
        IOobject::AUTO_WRITE
    ),
    max
    (
      (p_rgh + gh*(alpha1*rho10 + alpha2*rho20))
       /(1.0 - gh*(alpha1*psi1 + alpha2*psi2)),
        pMin
    )
);

volScalarField rho1(rho10 + b1/p +a1*p);
volScalarField rho2(rho20 + psi2*p);

volScalarField rho
(
    IOobject
    (
        "rho",
        runTime.timeName(),
        mesh,
        IOobject::READ_IF_PRESENT,
        IOobject::AUTO_WRITE
    ),
    alpha1*rho1 + alpha2*rho2
);
surfaceScalarField rhoPhi
(
    IOobject
    (
        "rho*phi",
        runTime.timeName(),
        mesh,
```

```
            IOobject::NO_READ,
            IOobject::NO_WRITE
        ),
        fvc::interpolate(rho)*phi
    );

    volScalarField dgdt
    (
        pos(alpha2)*fvc::div(phi)/max(alpha2, scalar(0.0001))
    );

    interfaceProperties interface(alpha1, U, twoPhaseProperties);
```

A.1.2.3 pEqn.H

```
{
    volScalarField rAU(1.0/UEqn.A());
    surfaceScalarField rAUf(fvc::interpolate(rAU));

    tmp<fvScalarMatrix> p_rghEqnComp;

    if (pimple.transonic())
    {
        p_rghEqnComp =
        (
            fvm::ddt(p_rgh)
          + fvm::div(phi, p_rgh)
          - fvm::Sp(fvc::div(phi), p_rgh)
        );
    }
    else
    {
        p_rghEqnComp =
        (
            fvm::ddt(p_rgh)
          + fvc::div(phi, p_rgh)
          - fvc::Sp(fvc::div(phi), p_rgh)
        );
    }


    U = rAU*UEqn.H();

    surfaceScalarField phiU
    (
        "phiU",
        (fvc::interpolate(U) & mesh.Sf())
      + fvc::ddtPhiCorr(rAU, rho, U, phi)
    );

    phi = phiU +
        (
            fvc::interpolate(interface.sigmaK())*fvc::snGrad(alpha1)
          - ghf*fvc::snGrad(rho)
        )*rAUf*mesh.magSf();

    while (pimple.correctNonOrthogonal())
    {
        fvScalarMatrix p_rghEqnIncomp
        (
            fvc::div(phi)
          - fvm::laplacian(rAUf, p_rgh)
```

```
    );
    solve
    (
        (
            max(alpha1, scalar(0))*(psi1/rho1)
          + max(alpha2, scalar(0))*(psi2/rho2)
        )
       *p_rghEqnComp()
      + p_rghEqnIncomp,
        mesh.solver(p_rgh.select(pimple.finalInnerIter()))
    );

    if (pimple.finalNonOrthogonalIter())
    {
        dgdt =
            (pos(alpha2)*(psi2/rho2) - pos(alpha1)*(psi1/rho1))
           *(p_rghEqnComp & p_rgh);
        phi += p_rghEqnIncomp.flux();
    }
}

U += rAU*fvc::reconstruct((phi - phiU)/rAUf);
U.correctBoundaryConditions();


p = max
(
    (p_rgh + gh*(alpha1*rho10 + alpha2*rho20))
   /(1.0 - gh*(alpha1*psi1 + alpha2*psi2)),
    pMin
);

rho1 = rho10 + b1/p + a1*p;
rho2 = rho20 + psi2*p;

Info<< "max(U) " << max(mag(U)).value() << endl;
Info<< "min(p_rgh) " << min(p_rgh).value() << endl;
```

Appendix B: case folder

The case folder is composed of `0`-, `constant`- and `system`- directories. The `constant`-directory consists of:

- a subdirectory `polymesh`, containing the dictionary for mesh generation `blockMeshDict`, that specifies the geometry and the mesh;
- files for specific properties, as `transportProperties`, where are specified the properties for each phase (i.e., density, viscosity, surface tension and other constants) and `g`, where the gravity field is defined.

The `system`-directory contains dictionaries for the simulation settings, that are:

- `controlDict`, which consists of settings for running the simulation;
- `fvSchemes` where discretization schemes for each term are defined;
- `fvSolution` consists of all settings concerning solving of matrices and pressure-velocity coupling;
- `setFieldsDict` contains information for assigning specific field properties to certain parts of the domain (i.e., volume fraction `alpha`).

The `0`-directory contains the files where initial and boundary conditions are specified for each field (velocity `U`, pressure `p_rgh` and volume fraction `alpha`. From `setFieldsDict` is possible to modify the values of internal fields at time zero.

As outlined in Appendix A, the implementations in the customized solver are:

1. the new equation of state for the biphasic liquid phase, that has required the update of `transportProperties` file in order to define the constant *a* and *b* of equation A.2;
2. a not uniform gravity field, that has required the definition of a new field, `gfield`, in the `0`-directory, opportunely initialized by `setFields` application. To this end, we set to 0 the "native" gravity field defined in `constant/g`.

In the following, we report the files `transportProperties`, `gfield`, `setFieldsDict`, `fvSchemes` and `fvSolutions`.

B.1 transportProperties

```
/*--------------------------------*- C++ -*----------------------------------*\
| =========                 |                                                 |
| \\      /  F ield         | OpenFOAM: The Open Source CFD Toolbox           |
|  \\    /   O peration     | Version:  2.1.1                                 |
|   \\  /    A nd           | Web:      www.OpenFOAM.org                      |
|    \\/     M anipulation  |                                                 |
\*---------------------------------------------------------------------------*/
FoamFile
{
    version     2.0;
    format      ascii;
    class       dictionary;
    location    "constant";
    object      transportProperties;
}
// * * * * * * * * * * * * * * * * * * * * * * * * * * * * * * * * * * * * //

phase1
{
    transportModel  Newtonian;
     nu              nu  [ 0 2  -1 0 0 0 0 ] 1.569e-5;
    rho             rho  [ 1 -3  0 0 0 0 0 ] 1142.16;
    rho0            rho0 [ 1 -3  0 0 0 0 0 ] 1150.33;
    a                psi [ 0 -2  2 0 0 0 0 ] 3.46e-7;
    b               bulk [ 2 -4 -2 0 0 0 0 ] -824065;
    CrossPowerLawCoeffs
    {
        nu0             nu0 [ 0 2 -1 0 0 0 0 ] 1e-06;
        nuInf           nuInf [ 0 2 -1 0 0 0 0 ] 1e-06;
        m               m [ 0 0 1 0 0 0 0 ] 1;
        n               n [ 0 0 0 0 0 0 0 ] 0;
    }

    BirdCarreauCoeffs
    {
        nu0             nu0 [ 0 2 -1 0 0 0 0 ] 0.0142515;
        nuInf           nuInf [ 0 2 -1 0 0 0 0 ] 1e-06;
        k               k [ 0 0 1 0 0 0 0 ] 99.6;
        n               n [ 0 0 0 0 0 0 0 ] 0.1003;
    }
}

phase2
{
    transportModel  Newtonian;
    nu              nu [ 0 2 -1 0 0 0 0 ] 1.48e-05;
    rho             rho [ 1 -3 0 0 0 0 0 ] 1;
    rho0            rho0 [ 1 -3 0 0 0 0 0 ] 0;
    psi             psi [ 0 -2 2 0 0 ] 1e-05;

    CrossPowerLawCoeffs
    {
        nu0             nu0 [ 0 2 -1 0 0 0 0 ] 1e-06;
        nuInf           nuInf [ 0 2 -1 0 0 0 0 ] 1e-06;
        m               m [ 0 0 1 0 0 0 0 ] 1;
```

```
        n               n [ 0 0 0 0 0 0 0 ] 0;
    }

    BirdCarreauCoeffs
    {
        nu0             nu0 [ 0 2 -1 0 0 0 0 ] 0.0142515;
        nuInf           nuInf [ 0 2 -1 0 0 0 0 ] 1e-06;
        k               k [ 0 0 1 0 0 0 0 ] 99.6;
        n               n [ 0 0 0 0 0 0 0 ] 0.1003;
    }
}

sigma           sigma [ 1 0 -2 0 0 0 0 ] 0.063;

pMin            pMin [ 1 -1 -2 0 0 0 0 ] 200;

// ************************************************************************* //
```

B.2 gfield

```
/*--------------------------------*- C++ -*----------------------------------*\
| =========                 |                                                 |
| \\      /  F ield         | OpenFOAM: The Open Source CFD Toolbox           |
|  \\    /   O peration     | Version:  2.1.1                                 |
|   \\  /    A nd           | Web:      www.OpenFOAM.org                      |
|    \\/     M anipulation  |                                                 |
\*---------------------------------------------------------------------------*/
FoamFile
{
    version     2.0;
    format      ascii;
    class       volVectorField;
    location    "0";
    object      gfield;
}
// * * * * * * * * * * * * * * * * * * * * * * * * * * * * * * * * * * * * * //

dimensions      [0 1 -2 0 0 0 0];

internalField   nonuniform List<vector>
128580
(
……
(-9.81 0 0)
……
(0 0 0)
)
;

boundaryField
{
    inlet
    {
        type            zeroGradient;
    }
    wall
    {
        type            zeroGradient;
    }
    axis
```

```
    {
        type            symmetryPlane;
    }
    top
    {
        type            zeroGradient;
    }
    right
    {
        type            zeroGradient;
    }
    bottom
    {
        type            zeroGradient;
    }
    fr
    {
        type            empty;
    }
    fr_pos
    {
        type            wedge;
    }
    fr_neg
    {
        type            wedge;
    }
}
```

B.3 setFieldsDict

```
/*--------------------------------*- C++ -*----------------------------------*\
| =========                 |                                                 |
| \\      /  F ield         | OpenFOAM: The Open Source CFD Toolbox           |
|  \\    /   O peration     | Version:  2.1.1                                 |
|   \\  /    A nd           | Web:      www.OpenFOAM.org                      |
|    \\/     M anipulation  |                                                 |
\*---------------------------------------------------------------------------*/
FoamFile
{
    version     2.0;
    format      ascii;
    class       dictionary;
    location    "system";
    object      setFieldsDict;
}
// * * * * * * * * * * * * * * * * * * * * * * * * * * * * * * * * * * * * * //

defaultFieldValues
(
    volScalarFieldValue alpha1 0
    volVectorFieldValue gfield (0 0 0)
);

regions
(
    boxToCell
    {
       box (0.105 0 -1) (3 0.00305 1);
```

```
        fieldValues
        (
            volScalarFieldValue alpha1 1
   );
    }
    boxToCell
  {
      box (0 0 -1) (0.08 0.05 1);
  fieldValues
        (
           volVectorFieldValue gfield (-9.81 0 0)
   );
    }
);
```

B.4 fvSchemes

```
/*--------------------------------*- C++ -*----------------------------------*\
| =========                 |                                                 |
| \\      /  F ield         | OpenFOAM: The Open Source CFD Toolbox           |
|  \\    /   O peration     | Version:  2.1.1                                 |
|   \\  /    A nd           | Web:      www.OpenFOAM.org                      |
|    \\/     M anipulation  |                                                 |
\*---------------------------------------------------------------------------*/
FoamFile
{
    version     2.0;
    format      ascii;
    class       dictionary;
    location    "system";
    object      fvSchemes;
}
// * * * * * * * * * * * * * * * * * * * * * * * * * * * * * * * * * * * * * //

ddtSchemes
{
    default         Euler;
}

gradSchemes
{
    default         Gauss linear;
}

divSchemes
{
    div(rho*phi,U)  Gauss upwind;
    div(phi,alpha)  Gauss vanLeer01;
    div(phirb,alpha) Gauss interfaceCompression 1;
    div(phi,p_rgh)  Gauss upwind;
    div(phi,k)      Gauss vanLeer;
    div((nuEff*dev(T(grad(U))))) Gauss linear;
}

laplacianSchemes
{
    default         Gauss linear uncorrected;
}
```

```
interpolationSchemes
{
    default         linear;
}

snGradSchemes
{
    default         uncorrected;//limited 0.5;
}

fluxRequired
{
    default         no;
    p_rgh;
    pcorr;
    gamma;
}


// ************************************************************************
```

B.4 fvSolutions

```
/*--------------------------------*- C++ -*----------------------------------*\
| =========                 |                                                 |
| \\      /  F ield         | OpenFOAM: The Open Source CFD Toolbox           |
|  \\    /   O peration     | Version:  2.1.1                                 |
|   \\  /    A nd           | Web:      www.OpenFOAM.org                      |
|    \\/     M anipulation  |                                                 |
\*---------------------------------------------------------------------------*/
FoamFile
{
    version     2.0;
    format      ascii;
    class       dictionary;
    location    "system";
    object      fvSolution;
}
// * * * * * * * * * * * * * * * * * * * * * * * * * * * * * * * * * * * * //

solvers
{
    pcorr
    {
        solver          PCG;
        preconditioner  DIC;
        tolerance       1e-08;
        relTol          0;
    }

    "(rho|rhoFinal)"
    {
        solver          diagonal;
    }

    p_rgh
    {
        solver          GAMG;
        tolerance       1e-12;
        relTol          0;
```

```
        minIter         3;
        maxIter         100;
        smoother        DICGaussSeidel;
        nPreSweeps      1;
        nPostSweeps     2;
        nFinestSweeps   2;
        scaleCorrection true;
        directSolveCoarsestLevel false;
        cacheAgglomeration on;
        nCellsInCoarsestLevel 500;
        agglomerator    faceAreaPair;
        mergeLevels     1;
    }

    p_rghFinal
    {
        $pcorr;
        tolerance       1e-8;
        relTol          0;
    }

    "(U|UFinal)"
    {
        solver          PBiCG;
        preconditioner  DILU;
        tolerance       1e-12;
        relTol          0;
    }
}

PIMPLE
{
    momentumPredictor         no;
    nCorrectors                5;
    nOuterCorrectors           1;
    nNonOrthogonalCorrectors   1;
    nAlphaCorr                 1;
    nAlphaSubCycles            2;
    cAlpha                     1;

    residualControl
    {
        p_rgh
        {
            tolerance 1e-8;
            relTol    0;
        }
        U
        {
            tolerance 1e-12;
            relTol    0;
        }
    }
}

// ************************************************************************
```

Bibliography

Amini, G., Ihme, M., & Dolatabadi, A. (2013). Effect of gravity on capillary instability of liquid jets. *Phys. Rew. E 87,* 053017.

Anna, S. L., & McKinley, G. H. (2001). Elasto-capillary number thinning and break-up of model elastic liquids. *J. Rheol. 45* , 115.

Basaran, O. (2002). Scaling, self-similarity, and intermediate asymptotics. *Cambridge University Press*.

Brennen, C. E. (2005). *Fundamentals of Multiphase Flows.* Cambridge University Press.

Castrejón-Pita, J. C.-P. (2015). Plethora of transition during breakup of liquid filaments. *Proc. Natl. Acad. Sci. USA 112*, 4582-4587.

Chandrasekhar, S. (1961). Hydrodinamic and hydromagnetic stability. Courier Corporation.

Chang, H.-C., Demekhin, E. A., & Kalaidin, E. (1999). Iterated stretching of viscoelastic jets. *Phys Fluids 11*, 1717.

Chen, A. N. (2002). Computational and experimental analysis of pinch-off and scaling. *Phys. Rev. Lett, 88*, 174501.

Chiegier, N., & Reitz, R. D. (1996). Regimes of jet breakup and breakup mechanisms (physical aspects). In *Recent Advances in Spray Combustion: Spray Atomization, vol. I* (pp. 109-136). K. K. Kuo.

Christanti, Y., & Walker, L. M. (2001). Surface tension driven jet break up fo strain-hardening polymer solutions. *J. Non-Newt. Fluid. Mech. 100*, 9.

Christanti, Y., & Walker, L. M. (2002). Effect of fluid relaxation time of dilute polymer solution on jet break up due to a forced disturbance. *J. Rheol. 46*, 733.

Clarke, N. S. (1968). Two-dimensional flow under gravity in a jet of viscous liquid. *J. Fluid Mech. 31*, 481.

Clasen, C., Philips, P. M., Palangetic, L., & Vermant, J. (2011). Dispensing of Rheologically Complex Fluids: The Map of Misery. *AlChE Journal*, 3242-3245.

Cooper-White, J. J., Fagan, J. E., Tirtamaatmadja, V., Lester, D. R., & Boger, D. V. (2002). Drop formation dynamics of constant low-viscosity, elastic fluids. *J. Non-Newt. Fluid Mech.*, 29-59.

Da Vinci, L. (1504-1508). Codex Leicester.

Danus, J. (2017). *Experimental design of a new nozzle.* Master Thesis.

Day, R. F. (1998). Self-similar capillary pinch-off in an inviscid fluid. *Phys. Rev. Lett., 80,* 704-707.

Deshpande, S. S., Anumolu, L., & Trujillo, M. F. (2012). Evaluating the performance of the two-phase flow solver interFoam. *Computational Science & Discovery 5*, 014016.

Dumouchel, C. (2008). On the experimental investigation on primary atomization. *Exp Fluids*.

Eggers, J. (1993). Universal pinching of 3D axisymmetric free-surface flows. *Phys. Rew. Lett 71*, 3458.

Eggers, J. (1997). Nonlinear dynamics and breakup of free-surface flows. *Reviews of Modern Physics, Vol 69*, 865.

Eggers, J. (2005). Drop formation, an overview. *Angew. Math. Mech 85*, 400-410.

Eggers, J., & Dupont, T. F. (1994). Drop formation in a one-dimensional approximation of the Navier-Stokes equation. *J. Fluid Mech 262*, 205.

Eggers, J., & Villermaux, E. (2008). Physics of liquid jets. *Rep. Porg. Phys. 71*, 036601.

Entov, V. M., & Hinch, E. J. (1997). Effect of a spectrum of relaxation times on the capillary thinning of a filament of elastic liquid. *J. Non-Newt. Fluid Mech. 72*, 31.

Ghidaoui, M. Z. (2005). A Review of Water Hammer. Theory and Practice. *Applied Mechanics Reviews, 58*, 49-76.

Gibson, A. (1908). Water Hammer in Hydraulic Pipe Lines. *London: Archibald Constable*.

Gouse, S. a. (1964). A survey of the velocity of sound in two-phase mixtures. *ASME Paper 64-WA/FE-35*.

Grant, R. P., & Middleman, S. (1966). Newtonian Jet Stability. *AlChE Journal*.

Hirt, C. N. (1981). Volume of fluid (vof) method for the dynamics of free boundaries. *Journal of computational physics, 39*, 1, 191-205.

Karplus, H. (1958). *The velocity of sound in a liquid containing gas bubbles.* Illinois Inst. Tech. Rep. COO-248.

Keller, J. B., Rubinow, S. I., & Tu, Y. O. (1973). Spatial instability of a jet. *Phys. Fluids 16*, 2052.

Korteweg, D. (1878). Uber die fortpflanzungsgeschwindigkeit des schalles in elastischen rohren. *Ann. Phys. 241*, 525-542.

Kowalewski, T. A. (1996). On the separation of drops from a liquid jet. *Fluid Dyn. Res 17*, 121-145.

Kroesser, F. W., & Middleman, S. (1969). Viscoelastic jet stability. *AlChE J. 15*, 383-386.

Li, Y., & Sprittles, J. (2016). Capillary breakup of liquid bridge: identifying regimes and transitions. *J. Fluid Mech. 797*, 29-59.

Lin, S., & Reitz, R. (1998). Drop and spray formation from a liquid jet. *Annu. Rev. Fluid Mech. 30*, 85-105.

Lister, J., & Stone, H. (1998). Capillary breakup of a viscous thread surrounded by another viscous fluid. *Phys. Fluids 10*, 2758.

Mandhane, J. G. (1974). A flow pattern map for gas-liquid flow in horizontal pipes. *Int. J. Multiphase Flow, 1*, 537-553.

Mariotte, E. (1718). Traité du mouvement des eaux et des autre corps fluides. Paris: E. Michallet.

Middleman, S. (1995). Modelling axisymmetric flows. *San Diego: Academic Pres*.

Middleman, S., & Gavis, J. (1961). Expansion and contraction of capillary jets of Newtonian liquids. *Phys. Fluids*, 335-359.

Montanero, J. M., Herrada, M. A., Ferrera, C., Vega, E. J., & Gañán-Calvo, A. M. (2011). On the validity of a universal solution for viscous capillary jets. *Phys. Fluids 23*, 122103.

Notz, P. C. (2001). Satellite drops: unexpected dynamics and change of scaling during pinch-off. *Phys. Fluids 13*, 549-552.

Omodei, B. J. (1980). On the die-swell of an axisymmetric Newtonian jet. *Comput. Fluids 8*, 275-289.

Papageorgiou. (1995). On the breakup of viscous liquid threads. *Physics of Fluids*.

Plateau, J. A. (1849). Statique experimentale et theorique des liquides soumis aux seules forces moleculaires. *Acad. Sci. Brux. Mem. 25*, 5.

Ranz, W. (1959). On sprays and spraying. *College of Engineering and Architecture*.

Rodd, L. S.-W. (2005). Capillary breakup rheometry of low-viscovisty elastic fluids. *Appl. Rheol.*, 12-27.

Rutland, D. F., & Jameson, G. J. (1971). A non-linear effect in the capillary instability of liquid jets. *J. Fluid Mech. 46*, 267.

Savart, F. (1833). Mémoire sur la constitution des veines liquides lancées par des orifices circulaires en mince paroi. *Ann. Chim. 53*, 337-98.

Sterling A.M., S. C. (1975). The instability of capillary jets. *Journal of Fluid Mechanics*, 477-495.

Stokes, G. G. (1880). A supplement to a paper on the theory of oscillatory waves. *Mathematical and Physical Papers 1*, 314-326.

TA INSTRUMENTS. (2017, 13 June). *Ares-G2 Rheometer*. Retrieved from http://www.tainstruments.com/ares-g2.

Takahashi, T., & Kitamura, Y. (1972). Stability of a Contracting Liquid Jet. *Memoirs School for Eng. Okayam Univ. 7*, 61-84.

Tjisseling, A. (1996). Fluid-structure interaction in liquid-filled pipe systems. *Journal of Fluids and Structures 10*, 109-146.

Tomotika, S. (1935). On the instability of a cylindrical thread of a viscous liquid surrounded by another viscous fluid. *Proc. R. Soc. Lond. A 150*, 322-37.

Umemura, A. (2011). Self-destabilizing mechanism of a laminar inviscid jet issuing from a circular nozzle. *Physical Rewiev E*, 83, 046307.

Umemura, A., Kawanabe, S., Suzuki, S., & Osaka, J. (2011). Two-valued breakup length of a water jet issuing from a finite-length nozzle under normal gravity. *Physical Rewiev E*, 84, 036309.

Weber, C. Z. (1931). Zum Zerfall eines Flussigkeitsstrahles. *ZAMM-Journal of Applied Mathematics and Mechanics/Zeitschrift für Angewandte Mathematik und Mechanik, Wiley Online 11*, 136-154.

Weisman, J. (1983). Two-phase flow patterns. *Handbook of Fluids in Motion*, 409-425.

Weller, H. T. (1998). A tensorial approach to computational continuum mechanics using object-oriented techniques. *Computer in Physics, 12*, 6-620.

Wu, P., & Faeth, G. (1995). Aeradynamic effects in primary breakup of turbulent liquid jets. *Atom. Sprays 3*, 265.

Wylie, E. S. (1993). Fluid transient in systems. *Prentice-Hall, Englewood Cliffs, New Jersey, 0-13-322173-3*.

Xu, Q., & Basaran, O. A. (2007). Computational analysis of drop-on-demand drop formation. *Physics of Fluids 19*, 102111.